# DNA PROGRAMMABLE SOFT MATTER DEVICES

by
Angelo J. Cangialosi

Department of Chemical and Biomolecular Engineering
Johns Hopkins University

A dissertation submitted to Johns Hopkins University in conformity with the requirements for the degree of Doctor of Philosophy

Baltimore, Maryland

May 2018

© 2018 Angelo Cangialosi
All Rights Reserved

# Abstract

The ability to program soft materials to undergo observable shape transformations in response to environmental stimuli is critical to the development soft programmable matter. In recent years, chemomechanical shape-changing hydrogels have garnered interest because they do not require wires or batteries and can operate untethered at smaller size scales. Devices comprised of these materials can respond to only a limited set of spatially non-specific stimuli such as temperature or pH – and are therefore restricted to a small set of final states. On the other hand, due to the large sequence space and programmable interactions of DNA molecules, devices comprised of DNA-conjugated hydrogel domains can potentially access a much larger set of final configurations through sequence-specific, addressable actuation of individual domains.

To investigate the shape-changing properties of single domain DNA-conjugated hydrogels, we first determine the swelling extent of DNA-crosslinked acrylamide networks in response to sequence-specific DNA stimuli. By coupling the DNA crosslinks to a DNA hybridization chain reaction that enables further incorporation of DNA to the crosslink sites, we demonstrate that specific DNA molecules can induce up to 100-fold volumetric hydrogel expansion. This large degree of swelling is then used to actuate approximately centimeter-sized gels containing multiple DNA-sensitive gel domains that each change shape in response to different DNA sequences. From swelling experiments and finite-element simulations we develop a simple design rule for the DNA-controlled shape change of a hydrogel bilayer.

The next generation of soft programmable matter and robotics will require materials that not only respond to distinct chemical species, but mechanical forces as well. Prior work in developing mechanochemically responsive polymers makes use of mechanophores – molecules that change configuration and initiate chemical reactions in response to mechanical forces – to instill bulk materials with force sensing properties. In this work, we use established thermodynamic models to design two DNA mechanophore complexes capable of responding to two distinct ranges of applied force. We micromold PEGDA copolymer hydrogels containing DNA mechanophore complexes and examine the force-sensing properties of the bulk material through the use of a multifunctional force microscope and a DNA-based fluorescence reporting scheme.

Because DNA molecules can be coupled to molecular sensors, amplifiers, and logic circuits, the incorporation of DNA complexes into hydrogel networks – whether as mechanophores or chemical crosslinkers –introduces the possibility of building soft matter devices that respond to numerous, distinct inputs and autonomously implement chemical control programs. These soft matter constructs have the potential to exhibit the multistage, goal-directed behaviors that are currently impossible to achieve in other soft robotic devices.

**Thesis Advisor**
**Dr. Rebecca Schulman**

**Thesis Committee Members**
**Dr. Michael A. Bevan**
**Dr. Joelle Frechette**
**Dr. Thao (Vicky) Nguyen**
**Dr. Sung Hoon Kang**

*If we knew what it was we were doing, it would not be called research, would it?*

Albert Einstein

# Acknowledgements

Even under the best of circumstances, graduate school can be a real whirlwind. Whether it's experiments that don't work, code that doesn't run, or lab chores you've been putting off, it can be exceedingly easy to forget why you chose to embark on this journey in the first place – something that I was guilty of on more than one occasion during my time in graduate school. Fortunately for me, I could count on the guidance and support of colleagues, advisors, and family to lift my spirits and help me remember the larger purpose behind this winding journey. One person without whom I couldn't have made it through graduate school is my advisor, Dr. Rebecca B. Schulman. This body of work is as much a testament to her extraordinary ingenuity as it is to the many hours spent in the lab conducting experiments. But more important than her constant stream of ideas was her support as an unwavering and caring mentor. She always took the time to check-in, see how I was doing and, most importantly, figure out how she could help. Unbeknown to those outside the Schulman lab, her towering intellect and unbridled passion for technology are exceeded by her mentorship for her students as they tackle ambitious and daunting projects. I will always be thankful for the opportunity to work in her lab. I can honestly say I learned from one of the very best.

Alongside my advisor, I would also like to thank my lab mates. To a person they were always selfless with their advice and expertise. Their enthusiasm for science and generosity of spirit were contagious. In short, they made graduate school much more fun than it otherwise would have been. A special thank you to Josh Fern, Sam Schaffter, Dominic Scalise, Philip Dorsey, and Deepak Agrawal for all of your help over the years.

According to an Italian proverb: "He who finds a friend, finds a treasure." If this is true, then in John Zenk, Abdul Mohammed, and Tanvi Shroff I probably hit the jackpot. During their time in the Schulman lab they made working in the lab about as fun it can possibly be. Their humor and kindness are at the heart of some of my fondest memories from graduate school. I will never forget, and will always be thankful for, their support through my graduate school journey as well as life's rougher moments.

Finally, I would like to thank my family. Without their love, support, and patience I definitely couldn't have embarked on, and sustained, this journey. To my siblings Allison, Nicholas, Ellen, and Jennifer – you are the best friends a person could ask for. Whether you realized it or not, from the very (very) beginning you have always inspired me to keep going, work harder, and try to enjoy life all the while. To my parents, if there was anyone in my life who deserves accolades for hard work and perseverance, it would be you two. I am where I am today through the power of your example. Any success I can claim from this journey is because of your unconditional love and support.

# Table of Contents

## List of Figures

## List of Tables

## List of Movies

# CHAPTER 1 INTRODUCTION

Ever since Toffoli and Margolus[1] first coined the term "programmable matter," the scientific community has constantly strived to develop new materials capable of dynamically interacting with their environment. Today, the term describes any material that can respond to environmental cues – whether derived from user input or autonomous sensing – by changing its shape or properties according to a predetermined set of instructions.[2] With an eye towards how nature achieves this behavior in biological organisms, one prominent strategy has been to embed collections of sensors, actuators, and controllers within a base material. The role of each of these components is most clearly illustrated in hard robotic devices where, for example, a sensor attached to a hard-material framework would detect external stimuli such as light, heat, or mechanical force and then transmit this signal via electric wiring to a controller or computational unit. The controller would then process this input according to a given set of instructions, i.e., a program, and execute the appropriate response via an actuator. For hard robotic devices, actuation can take the form of material deformation (e.g., moving stiff appendages via hinges and joints), textural changes, or color alterations, etc.[3] Integration of sensing, computational, and actuation components has produced devices that can sense touch and classify different textures,[4] detect incoming sound waves and then alert the user as to their direction,[5] or recognize a user's physical gestures and respond with changes in color and opacity.[6]

While an impressive array of hard robotic devices has been constructed based on the aforementioned engineering paradigm of sensors, controllers, and actuators, challenges remain in building devices with increasingly complex behavior. For instance, the hard skeletal framework inherent in these devices restricts the number of spatial configurations they can occupy, making it difficult for them to change shape, handle delicate objects, or traverse rough terrain.[7] Along with their physical configurations, there are inherent limitations to both the range of stimuli and number of actuation mechanisms they are able to accommodate.[3] Overcoming these limitations through the installation of more sensors and actuators increases the overall weight, cost, and fabrication difficulty of the device, and thus limits its applicability. Furthermore, the use of additional sensors and actuators increases the challenge of systems-level integration of these components. More bandwidth is required to transmit sensor and actuation signals to and from the controller, and more memory is required to process incoming and outgoing signals.

To surmount some of these challenges, engineers have turned to soft-bodied robotic devices. In 2008 Trivedi *et al.* defined these devices – aptly termed "soft robots" – as "continuum robots made of soft materials that undergo continuous elastic deformation and produce motion through the generation of a smooth backbone curve."[8] The continuous, rather than discrete, deformation possible with base materials such as elastomers, hydrogels, and electroactive polymers enables soft robotic devices to access a larger physical deformation space and, as a result, achieve more complex motions.[7,9,10] For example, in 2011 the Whitesides laboratory constructed soft, McKibbon-type actuating devices comprised of channels of pneumatic networks (PneuNets).[11] The devices were synthesized using two readily available, highly elastic components – polydimethylsiloxane and Ecoflex® – and were deformed by supplying pressurized air via plastic tubing. While these PneuNet devices were shown to handle delicate objects and traverse challenging terrain, they required user input in the form of pressurized air to achieve actuation. This shortcoming was later corrected with the development of the "octobot" – a soft robot comprised of the same base materials as the PneuNet, but which was autonomously powered by monopropellant fuel and controlled by a microfluidic logic component.[12] Here, the monopropellant fuel produced the gaseous fluid that strained the pneumatic chambers, while the microfluidic logic component controlled the flow of gas to the chambers and was used to achieve oscillatory actuation of the octobot arms. The autonomous operation of the octobot represented a major leap forward in the field of soft robotics as, quite literally, cutting the wires and tethers that connected soft robotic devices to external electric or pneumatic power sources had been a longstanding goal of soft roboticists. Yet for all its advancements, the octobot still lacked the stimuli-sensing capabilities necessary for a fully autonomous, programmable soft matter device.

A class of soft materials that engineers have had great success with in demonstrating autonomous sensing and stimuli-responsive behaviors are hydrogels, which are broadly defined as physically or chemically crosslinked networks of hydrophilic polymers swollen to varying degrees in aqueous environments.[13] While they behave as an elastic solid, hydrogels are primarily composed of aqueous solvent and, as a result, have several major advantages over other soft materials. Perhaps chief among these is their compatibility with biological systems such as tissues and cells.[14] Their high water content and porosity, along with the wide range of developed chemistries one can use to functionalize the hydrophilic polymer networks with bioactive molecules (e.g., "click" chemistry), make hydrogels particularly well-suited to host – and interface with – biomolecular-based reaction networks.[15] This quality has led hydrogels to find medicinal applications in areas such as drug delivery, tissue engineering, and implants.[14,16,17]

More importantly, various hydrogel compositions have been shown to exhibit autonomous, stimuli-responsive behavior to a wide variety of well-defined environmental cues such as light, pH, heat, and magnetism.[18,19] For example, Yoon *et al.*[20] fabricated hydrogel sheets that, through actuating hydrogel hinges, fold into cube and pyramidal shapes in response to either temperature or pH changes. Similarly, Hauser *et al.*[21] fabricated hydrogel-nanoparticle composite sheets that locally buckle when selected regions are illuminated with white light. The pronounced deformations experienced by these and other hydrogel-based devices are primarily due to the tight coupling of sensing and actuation via the dynamics of the polymer network: external stimuli change the total free energy of the network, which then causes an uptake or expulsion of water molecules from the gel. Whether it's from a homogenous hydrogel exposed to a spatially heterogeneous stimulus (exemplified by Hauser *et al.*) or a heterogeneous hydrogel exposed to a spatially homogenous stimulus (exemplified by Yoon *et al.*), both of these devices demonstrate that even a single stimulus can cause hydrogel devices to undergo complex shape transformations.

While hydrogels have been demonstrated to undergo two or three shape transformations in response to distinct stimuli,[22] they are ultimately limited in the number of conventional signals they are able to sense. But what if an engineer wanted to build a hydrogel-based soft robotic device capable of extraordinarily complex shape transformations – behavior that would require a device to recognize hundreds of different stimuli and respond with hundreds of different actuation responses? Not only would this device need to be comprised of many more distinct domains than what has been previously fabricated, it would have to possess sophisticated computational abilities to process the multitude of input signals. To begin our journey answering this question, we restricted our engineering efforts to chemoresponsive hydrogels due to the large compositional space of molecules and their interactions. For the chemical signals that would interface with our chemoresponsive hydrogels, we turned to DNA due to its demonstrated ability to store information, form molecular circuits, and perform computations.[23,24]

Biological organisms interact with their environment through complex and tightly regulated molecular networks that sense chemical stimuli, perform computations, and release chemical signals.[25] Much of these interactions are rooted in the capacity of deoxyribonucleic acid (DNA) to encode genetic information and interact with other biomolecules. DNA's role as information-carrying molecule was first suggested upon the discovery of its three-dimensional structure by James Watson, Francis Crick, and Rosalind Franklin in 1953.[26] In their landmark *Nature* article, Watson and Crick posited what is now known as Watson-Crick complementarity: adenine (A) bonds to thymine (T), while guanine (G) bonds to cytosine (C), which they believe suggested "a possible copying mechanism for the genetic material," and enabled it to store information. The central role of DNA in biology led the scientific community to immediately undergo an enormous effort studying its chemical and physical properties. Techniques such as calorimetry[27] and spectroscopy[28] were used to determine the standard enthalpies and entropies of oligonucleotide duplex formation. The accumulation of thermodynamic data eventually led to the formation of nearest-neighbor (NN) models which predict the free energy of formation of DNA complexes based solely on the sequences of the individual strands.[29] Together with certain computational techniques, these NN models are at the heart of tools such as NUPACK[30] and Mfold[31] that can predict the equilibrium concentrations and secondary structure of oligonucleotide complexes at given set of temperature and salt conditions.

As thermodynamic properties and basepairing models began to emerge, starting in the 1980s scientists began to view DNA as a potential, if not ideal, engineering material. As first demonstrated by Nadrian Seeman,[32] the Watson-Crick base pairing rules, thermodynamic properties, and measurement of the physical dimensions of DNA molecules enabled the rational design of complex DNA nanostructures. Furthermore, beginning with the landmark 1994 study of Leonard Adleman in which he used DNA as a substrate to compute the solution to a seven-city Hamiltonian path problem,[33] the potential of DNA to perform computations and control molecular systems began to be realized. In the following years Boolean logic gates,[34] circuits,[23] and even neural networks,[24] would be constructed entirely out of DNA. Central to these molecular devices is the DNA-based strand displacement reaction: a process by which a single-stranded DNA species is displaced from its original complex by the hybridization of another DNA strand.[35] These reactions are often mediated by the binding of single-stranded domains called "toeholds"[36] and proceed as follows: (1) the single-stranded toehold domains in the initial DNA complex and single-stranded DNA species hybridize, (2) a branch migration process follows where domains in the incoming and originally bound strand compete for the same complementary regions, and (3) the originally bound strand is fully displaced from the DNA complex. These reactions are thermodynamically driven by the decrease in free-energy that accompanies DNA hybridization and have been show to possess kinetic tunability[36] via modification of the toehold length and composition.

The large sequence space of DNA, along with its well-studied thermodynamic properties, eventually led the engineering community to employ DNA-based molecular systems to modulate the behavior of macroscale materials – including hydrogels. Nagahara and Matsuda initiated this body of work with their 1996 study demonstrating hydrogel formation via the hybridization of polyA and polyT oligonucleotide complexes covalently bound to separate poly(N,N-dimethylacrylamide) macromers.[37] Furthermore, thermal denaturation of the DNA crosslinker complex conferred thermoresponsive behavior onto the bulk gel material. Next, Murakami *et al.* took advantage of the sequence specificity of DNA-based reactions and demonstrated a roughly 20% increase in volume of DNA-acrylamide copolymer hydrogels in response to sequences that paired with the stem and loop regions of the ssDNA hairpin crosslinkers.[38] In their study DNA-acrylamide copolymer gels treated with non-complementary ssDNA showed little to no volume change. In another set of studies, Lin et al. employed a three-strand DNA crosslinker complex to tune mechanical properties in DNA-acrylamide copolymer gels through the addition of sequence-specific oligonucleotides. Toehold-mediated DNA strand displacement reactions between the DNA crosslinker and added ssDNA were used to either modify the stiffness[39] or decrease the crosslink density[40] of the bulk gel. The crosslinker designs used by Lin *et al.* are the main inspiration for the work presented in *Chapter 4* of this thesis.

The aforementioned DNA-responsive hydrogels – while advancements in their own right – did not possess the mechanical properties required for a multidomain, DNA-programmable soft robotic device. Specifically, these materials did not possess the high degree of swelling necessary to drive mechanical deformation of would-be neighboring hydrogel domains. To fill this gap, we set out to develop a novel DNA copolymer hydrogel material capable of large-degree swelling in response to DNA stimuli. But first, in Chapter 2, we demonstrate the programmability of DNA-based molecular interactions through the construction of a DNA timer circuit. Using simple mass action kinetic principles and DNA strand displacement reactions, we program the release of target DNA sequences at a constant rate and with a tunable delay period. In *Chapter 3*, the heart of this thesis, we employ a previously developed DNA hybridization cascade reaction to swell DNA-crosslinked polyacrylamide gels up to 100 volumetric-fold. Standard photolithographic techniques were used pattern multidomain gel structures that undergo different shape transitions in response to different sequences. A simple design rule for the actuation of hydrogel bilayers was formulated and verified using a previously-developed constituitive model for hydrogel swelling and deformation. Next, *Chapter 4* of this thesis details the DNA crosslinking schemes that were investigated prior to the one discussed in *Chapter 3*. These schemes, largely based on the work of Lin *et al.*,[39,40] were never shown to achieve uniaxial swelling greater than roughly twenty percent, far lower than what we predicted was necessary to swell a multidomain hydrogel architecture. Lastly, in *Chapter 5* we detail the construction of DNA-based force sensor complexes and the initial efforts undertaken to synthesize and characterize a force sensing DNA copolymer hydrogel. This thesis concludes in *Chapter 6* with a discussion of potential applications of, and improvements to, the research described in *Chapters 3* through *5*.

## 1.1 CONTRIBUTIONS

**Chapter 2**
A version of Chapter 2 was published:

Fern, J.; Scalise, D.; Cangialosi, A.; Howie, D.; Potters, L.; Schulman, R. DNA Strand-Displacement Timer Circuits. *ACS Synth. Biol.* **2017**, *6* (2), 190–193.

Josh Fern carried out the experiments and analyzed the data; Josh Fern, Dominic Scalise, and Rebecca Schulman planned the experiments and wrote the paper. Experiments for a previously submitted version of the paper were carried out by Angelo Cangialosi.

**Chapter 3**
A version of Chapter 3 was published:

Cangialosi, A.; Yoon, C.; Liu, J.; Huang, Q.; Guo, J.; Nguyen, T. D.; Gracias, D. H. DNA Sequence – Directed Shape Change of Photopatterned Hydrogels via High-Degree Swelling. *Science.* **2017**, *357* (6356), 1126–1130.

Angelo Cangialosi, Chang Kyu Yoon, and Qi Huang carried out the experiments; Angelo Cangialosi analyzed the data. Experiments were designed by Angelo Cangialosi, Chang Kyu Yoon, Rebecca Schulman, David Gracias, and Thao (Vicky) D. Nguyen; Simulations were designed and performed by Jingkai Guo, Jiayu Liu, and Vicky Nguyen. The paper was written by Rebecca Schulman, Angelo Cangialosi, David Gracias, Vicky Nguyen, and Jiayu Liu.

**Chapter 4**
Angelo Cangialosi and Chang Kyu Yoon performed the experiments; Angelo Cangialosi analyzed the data. Experiments were designed by Angelo Cangialosi, Chang Kyu Yoon, Rebecca Schulman, David Gracias, and Thao (Vicky) D. Nguyen.

**Chapter 5**
Experimentation with respect to the contents of Chapter 5 is still ongoing. Experiments shown in Chapter 5 were planned by Angelo Cangialosi, Rebecca Schulman, Jiayu Liu, Vicky Nguyen, Joelle Frachette, and Paul Roberts. Experiments were performed by Angelo Cangialosi, Jiayu Liu, Paul Roberts, and Lei Zhang. The Arruda-Boyce model was developed by Vicky Nguyen, Jiayu Liu, and Zheng Jia; subsequent calculations and modeling of the polymer network mechanical properties were performed by Jiayu Liu in consultation with Rebecca Schulman and Vicky Nguyen.

# CHAPTER 2 DNA STRAND-DISPLACEMENT TIMER CIRCUITS

## SUMMARY

Chemical circuits can coordinate elaborate sequences of events in cells and tissues, from the self-assembly of biological complexes to the sequence of embryonic development. However, autonomously directing the timing of events in synthetic systems using chemical signals remains challenging. Here we demonstrate that a simple synthetic DNA strand-displacement circuit can release target sequences of DNA into solution at a constant rate after a tunable delay that can range from hours to days. The rates of DNA release can be tuned to the order of 1-100 nM per day. Multiple timer circuits can release different DNA strands at different rates and times in the same solution. This circuit can thus facilitate precise coordination of chemical events *in vitro* without external stimulation.

## 2.1 INTRODUCTION

While gene networks in cells can orchestrate intricate processes by modulating gene expression to release a series of target molecules at specified times,[41,42] synthetic *in vitro* biochemical protocols commonly involve manual steps performed by an experimenter, in which reagents are added, filtered, heated or otherwise altered. Artificial mechanisms to automate the temporal release of trigger molecules would make it possible to direct sequential events without the need for external stimulation. Further, the timed release of molecules using such a process could act as a trigger to control acellular self-assembly processes,[43–45] multistep reaction cascades,[46] or to time the release of signaling molecules or other reagents in cell culture.[47–49]

In this chapter, we build a chemical timer circuit that releases a target sequence of DNA at a constant rate from DNA complexes after a tunable delay period. In contrast to previously designed synthetic in vitro transcriptional timer circuits,[50] our timer is controlled solely by DNA strand-displacement processes, which have previously been used to perform diverse information processing tasks including Boolean logic,[23,34,51–53] signal amplification,[54–57] neural network computation[24] and oscillatory signal generation.[58] The timer circuit is designed such that the strand that is released can be coupled to many of these systems in their present form, suggesting that timer circuits will make it possible to activate elaborate information processing tasks at specified times. Further, a design based on strand displacement reactions alone should allow the circuit to operate in a variety of buffers and at a variety of temperatures without redesign.[55] The timer circuit works by suppressing the release of a single-stranded DNA molecule for a delay period, after which the molecule is allowed to increase in concentration at a constant rate. We show how to design a timer circuit within an abstract chemical reaction network, and then describe an implementation of the abstract network using a simple set of DNA molecules that interact through strand-displacement reactions. Next, we investigate the range of delay periods and release rates that are possible using our circuit, and finally demonstrate that multiple timer circuits can operate within the same solution. Throughout this chapter, all supplemental figures and tables are listed in § 2.5 and are denoted by a "S" before the figure/table number (e.g. Figure S2.5.1 is the first supplemental figure).

## 2.2 RESULTS & DISCUSSION*

The timer circuit consists of two simultaneous abstract chemical processes: *production* (Eqn. 2.1) and *delay* (Eqn. 2.2):

$$\emptyset_{Source} \xrightarrow{k_{prod}} \mathrm{O} \tag{2.1}$$

$$\mathrm{O} + \mathrm{D} \xrightarrow{k_{delay}} \emptyset_{Waste} \tag{2.2}$$

In the production process, the output **O** is released by a zero-order reaction at a constant rate $k_{prod}$. In the delay reaction, **O** is rapidly converted into inert waste when it reacts with a delay species **D**. If $k_{delay}[\mathbf{O}][\mathbf{D}] \gg k_{prod}$, **O** cannot accumulate until all of **D** has been depleted (Figure 2.1).

We call the time during which **O** cannot accumulate the delay time, $t_{delay}$, which is the time needed to produce enough **O** to consume all of the **D** that is initially present:

$$t_{delay} = \frac{[\mathbf{D}]_0}{k_{prod}} \tag{2.3}$$

This time can be easily tuned by changing the initial concentration of **D**.

During the delay period, [**O**] remains very small because any molecules of **O** that are produced are rapidly removed. After **D** is depleted, however, [**O**] increases linearly with time. The approximate concentration of free **O** is therefore:

---

* Throughout this chapter, all supporting figures and tables are listed in § 2.5 and are denoted with a "S" before the figure/table number (e.g. Figure S2.1 is the first supporting figure of the supporting information section).

$$[O] \approx \begin{cases} k_{prod}/\left(k_{delay}[\mathbf{D}]\right) \approx 0, & \text{if } t < t_{delay} \\ k_{prod}\left(t - t_{delay}\right), & \text{otherwise} \end{cases} \tag{2.4}$$

where [**O**] and [**D**] are functions of time.

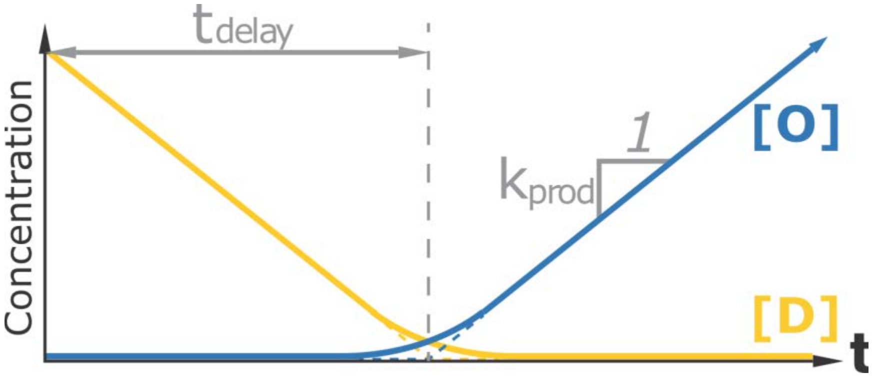

**Figure 2.1 Schematic for the operation of a timer circuit.** The output species (blue) is constantly produced at rate $k_{prod}$, but is rapidly consumed by the delay species (yellow). This rapid consumption prevents the accumulation of output until time $t_{delay}$, when the delay species is depleted.

To construct a timer circuit that controls the release of a DNA strand, we built a set of DNA strand-displacement reactions that emulate the abstract reactions in Eqns. 2.1 and 2.2 (Figure 2.2).[59,60] The domain level structure of our complexes follows a DNA architecture previously used for Boolean logic circuit evaluation.[53] Within this implementation, strand **O** is initially partially bound within a complex. The production process frees **O** from this complex, making **O** available in its full single-stranded form (Figure 2.2a). The delay process likewise sequesters **O** in a waste complex in which the toehold domain of **O** is covered (Figure 2.2b). Because an exposed toehold domain is generally required to initiate downstream strand-displacement reactions, the delay circuit will control when **O** is available in a functional form.

**Production.** The production reaction releases an output molecule **O** when a source complex **S** and an initiator strand **I** react (Figure 2.2a). This strand-displacement process is facilitated by the spontaneous pairing and unpairing of the bases on the ends of the source complex, i.e., fraying. During the short time periods when these bases are frayed, **I** can bind and compete with **O** until one or the other is displaced.

Reactions initiated by fraying alone have an exceptionally small reaction rate constant, on the order of 0.5 $M^{-1}$ $s^{-1}$, which we denote by $k_{0bp}$.[36,61] On the order of days, very little **S** and **I** react, allowing us to assume [**S**] and [**I**] remain effectively constant when considering shorter time scales. To release an appreciable concentration of **O**, we use a large amount of **S** and **I** in a reaction. The rate at which **O** is released into solution can therefore be approximated as a constant we term $k_{prod}$:

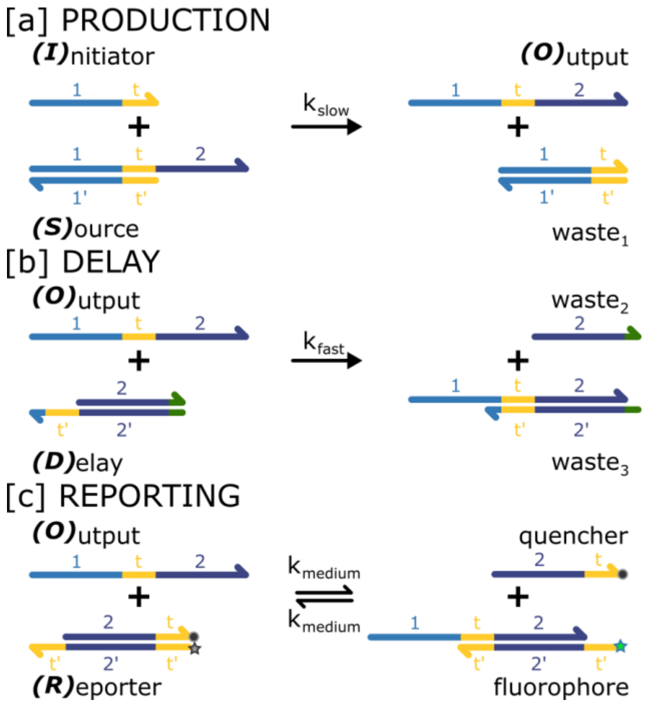

**Figure 2.2 Strand-displacement reactions for a timer circuit.** (a) PRODUCTION: Output is slowly released from source in the presence of initiator. (b) DELAY: Output is rapidly consumed by the delay complex. (c) REPORTING: Free output binds reversibly to a reporter complex, separating quencher and fluorophore modifiers. FAM and TexasRed paired with appropriate quenchers were used to report on two different output sequences (see Section 2.4, Materials and Methods).

$$\frac{d[\mathbf{O}]}{dt} = k_{0bp}[\mathbf{S}][\mathbf{I}] \approx k_{prod} \tag{2.5}$$

Eq 2.5 shows that $k_{prod}$ can be easily tuned by changing the initial concentrations of **S** and **I**. For simplicity, and to maximize the time during which the approximation of constant concentrations is reasonable, we keep their initial concentrations equal, i.e., $[\mathbf{S}]_0 = [\mathbf{I}]_0$. At longer time scales, the approximation of a constant $k_{prod}$ is violated and [**O**] increases according to second order reaction kinetics.

**Delay**. To keep [**O**] low while the delay species is present, the delay reaction must sequester O at a rate much faster than $k_{prod}$. The delay complex **D** (Figure 2.2b), which has a 7 base pair (7 bp) single-stranded toehold domain that binds to O and colocalizes it with **D**, acts as a concentration thresholding device.[23] Reactions mediated by 7 bp toeholds proceed at approximately 6 orders of magnitude faster than reactions without a mediating toehold.[36,61] A 2 bp clamp (green in Figure 2.2b) inhibits some undesired interactions between **S** and **D** while ensuring that the reaction between **O** and **D** remains strongly forward-biased. Clamps with only 1 bp may not reliably prevent interactions at that end and clamps with greater numbers of bases (e.g., 5 bp) are expected to strongly decrease the sequestering ability of the thresholding device due to reaction reversibility.[34,55]

To monitor the reaction's progress, we also include a reporter complex modified with a fluorophore and an associated quencher to track the concentration of free **O** over time. This complex reacts reversibly with the output strand on a time scale much faster than the production reaction, but slower than the delay process, and produces fluorescence as a function of [**O**] at a given time (Figure 2.2c). The concentration of **O** is related to the fluorescence levels using a calibration curve (Fig. S2.1).[62,63] To build a timer circuit, the source complex **S** and the delay complex **D** are initially combined and the timer is triggered upon the addition of the initiator strand **I**. To demonstrate that the individual reactions performed as desired and determine how the production rate varied with initial concentrations of **S** and **I**, we tested each reaction in isolation at 25 °C (Figure 2.3a,b, § 2.5.2). To test the production reaction, we varied $[\mathbf{S}]_0 = [\mathbf{I}]_0$ from 0.25 μM to 2 μM (Figure 2.3a) and determined the average $k_{0bp}$ to be $0.49 \pm 0.13\ \mathrm{M}^{-1}\ \mathrm{s}^{-1}$ (Table S2.1) which is in good agreement with previous estimates.[36,61] We calculated, using $[\mathbf{S}]_0$ and $[\mathbf{I}]_0$, that $k_{prod}$ varied from 0.15 to 4 nM/hour over the range of concentrations tested (Table S2.1). When the delay reaction was tested in isolation, the delay complex sequestered free **O**, resulting in a sudden decrease in output detected by the reporter (Figure S2.7). The decrease in [**O**] matched the concentration of **D** added to the reaction solution (Figure 2.3b).

To characterize the delay time before **S** begins accumulating as a function of $[\mathbf{D}]_0$ (Eqns 2.3 and 2.4), we varied $[\mathbf{D}]_0$ while keeping the production rate (determined by $[\mathbf{S}]_0$ and $[\mathbf{I}]_0$) constant. **O** remained low for a delay period that increased with $[\mathbf{D}]_0$ (Figure 2.3c). For each trial, we used linear least-squares fitting to identify the portion of the production regime with the steepest slope (§ 2.5.3) and used the slope and y-intercept of this fit to calculate the delay time. This method allowed us to measure the delay time without being affected by the ramp up in release that occurs because small amounts of **D** are still present when release noticeably begins. We observed that the delay time varied linearly with respect to the initial concentration of **D** (Figure 2.3d). We also tested two other timer circuits with lower initial concentrations of **S**, **I** and **D**, and obtained systems with similar delay times but slower rates of output release (§ 2.5.3).

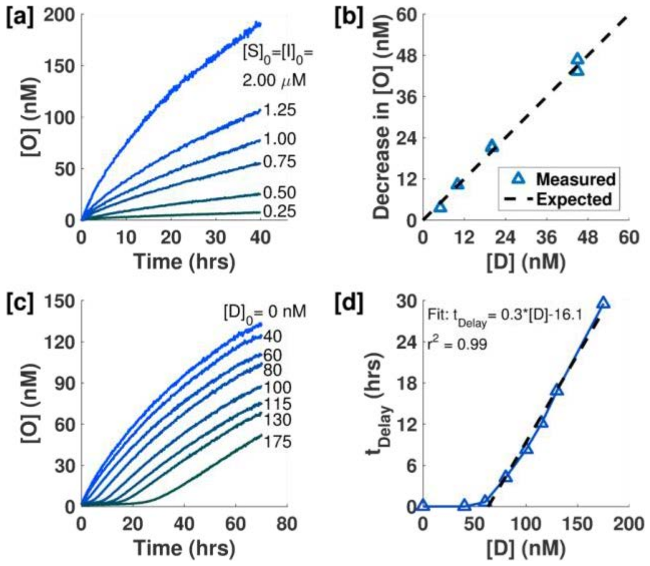

**Figure 2.3 Production, Delay and Timer circuit reactions.**(a) Production kinetics in the absence of **D**. Release rate is dependent upon initial [**S**] and [**I**]. (b) [**O**] decreases proportionally to added [**D**]. (c) Delay time was tuned by changing the initial concentration of the delay species **D**. $[\mathbf{S}]_0=[\mathbf{I}]_0=1$ μM. (d) Plot of delay time vs. initial concentration of **D**, showing an approximately linear relationship after an initial offset.

Because the delay circuit is based on DNA strand-displacement events involving a particular DNA sequence, it is possible to create multiple circuits that use different sequences and can trigger the delayed release of two different DNA strands (Figure 2.4). To characterize the operation of two timer circuits in a single solution, we prepared a second timer circuit and reporter complex with different sequences and fluorophore/quencher than our original system. The second system had the same qualitative behavior, and it was possible to programmatically tune both delay times and release rates. Differences in rates and delay times were observed between the two systems, possibly due to differences in toehold sequence that affect reaction rates (§ 2.5.4−2.5.5). The two systems were able to operate together in the same solution with virtually identical kinetics to those observed when the systems were operated apart (Figure 2.4).

The timer circuit developed here successfully releases target strands of DNA into solution at a constant rate after a delay period. The sequence, delay time and production rate were easily tuned without needing to redesign the release system. We demonstrated delay times on the order of hours to days and production rates from a few nM/day to a hundred nM/day, which for volumes of 100 μL are approximately 0.1−10 nmol/ day.

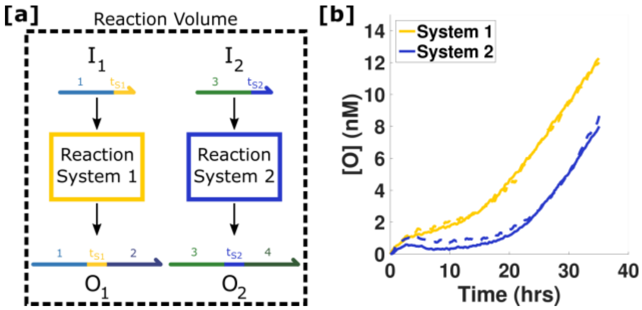

**Figure 2.4 Multiplexed timers.** (a) Schematic of multiple timer circuits operating within the same solution, releasing independent output strands at different times. (b) Two timers release output with the same rate but at different times (9 and 17 hrs). Here, $[\mathbf{S}]_0=[\mathbf{I}]_0=0.5$ µM and $\{[\mathbf{D}]_{\mathrm{Sys1}}, [\mathbf{D}]_{\mathrm{Sys2}}\}=\{46$ nM, $63$ nM$\}$. Dashed lines indicate the same reactions except with each system in isolation.

While the release of **O** observed (Figure 2.3, Figs. S2.8−S2.10) qualitatively followed our simple model described in eqs 2.1−2.5, there were differences between experiments and reaction curves predicted by the model. Notably we found that the release rate of **O** decreased faster and to a greater degree than the predicted reaction curves, suggesting the existence of uncharacterized reactions (i.e., leak reactions) between **S** and **D** or the reporter. On the basis of the experiments, we hypothesize that DNA synthesis errors (e.g., base-mismatches, truncations, additions or deletions) in the bottom strand of the **S** complex led to leak reactions and pathways that explained most of the deviation from the simple model. By accounting for these and other more minor leak reactions, a model was developed that provided a close fit with the experimental observations (§ 2.5.6), indicating that models can be used to program the rate and timing of output release.

## 2.3 CONCLUSION

By designing a circuit in which the output DNA sequence is an aptamer,[43,64] i.e., sequences of DNA that bind specifically to non-DNA species such as proteins[65] and other small molecules,[66] the circuit described here could also be used to control the dynamics of a wide range of other chemical systems beyond DNA strand-displacement.

Timer devices that can be programmed to release a particular species with a pre-specified delay could be important for designing cascades for therapeutics or for self-assembly[45,67] in which different species are activated at different times. The constant low-rate of production we have shown could be used to design therapeutic hydrogels with novel, linear release profiles or within a reliable pulsed delivery system by combining it with a threshold amplifier system such as those used for signal restoration in molecular logic circuits.[23,68]

## 2.4 MATERIALS & METHODS

The timer circuit was designed following the principles outlined in reference 14. Sequences for each domain were drawn from Table S1 of the Supporting Online Material for reference 14 and are listed here in Table 1. Domains *S6* and *S5* listed below correspond to Domains *1* and *2* depicted in Figure 2.2 of the Main Text and Figure 2.5. The toehold (*t*) domain of System 2 was designed to have minimal non-specific interactions with the sequences of both systems using NUPACK.[30] Domain names and sequences are listed 5' to 3'. Additional schematics of the DNA complexes and the reactions are shown in § 2.5.2.

**Table 2.1 Sequence Data**

| **Strand Names** | **Domain Names** | **Sequences** |
|---|---|---|
| Source 1 Top | *S6 t S5* | CA TAACACAATCA CA TCT CA CCACCAAACTT CA |
| Source 1 Bottom | *t' S6'* | TG AGA TG TGATTGTGTTA TG |
| Initiator 1 | *S6 t* | CA TAACACAATCA CA TCT CA |
| Delay 1 Top | *S5* | CA CCACCAAACTT CA CT |
| Delay 1 Bottom | *S5' t' S6' (2nt)* | AG TG AAGTTTGGTGG TG AGA TG TG |
| Reporter 1 Top | *S5 t Quencher* | CA CCACCAAACTT CA TCT CA/3IABkFQ/ |
| Reporter 1 Bottom | *FAM t' S5' t'* | /56-FAM/TG AGA TG AAGTTTGGTGG TG AGA TG |
| Reporter 1 Full Complement | *t S5 t* | CA TCT CA CCACCAAACTT CA TCT CA |
| | | |
| Source 2 Top | *S27 t S28* | AC AACACTCTATT AC AAT AC TCTACAATTCA AC |
| Source 2 Bottom | *t' S27'* | GT ATT GT AATAGAGTGTT GT |
| Initiator 2 | *S27 t* | AC AACACTCTATT AC AAT AC |
| Delay 2 Top | *S28* | AC TCTACAATTCA AC CA |
| Delay 2 Bottom | *S28' t' S27' (2nt)* | TG GT TGAATTGTAGA GT ATT GT AA |
| Reporter 2 Top | *S28 t Quencher* | AC TCTACAATTCA AC AAT AC/3IABRQSp/ |
| Reporter 2 Bottom | *TexasRed t' S28' t'* | /5TexRd-XN/GT ATT GT TGAATTGTAGA GT ATT GT |
| Reporter 2 Full Complement | *t S28 t* | AC AAT AC TCTACAATTCA AC AAT AC |

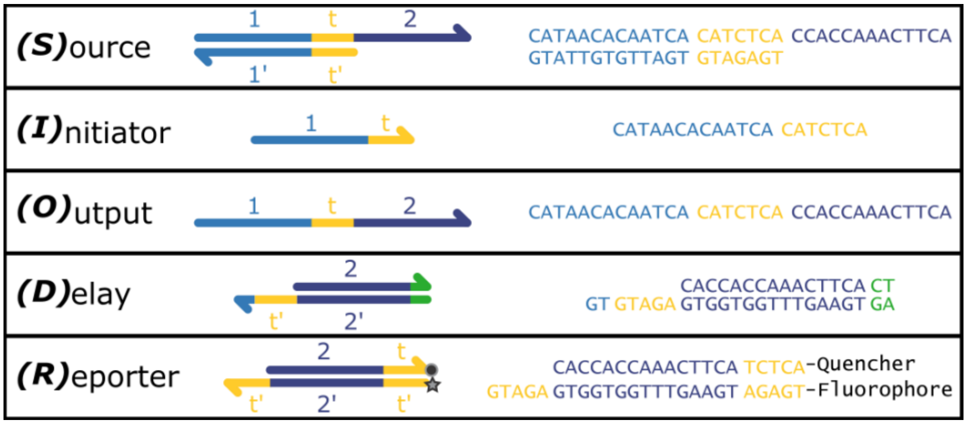

**Figure 2.5 Schematic of reaction species with their sequences as listed in Table 1.** Reactions between species for the timer circuit are shown in Figures S2.3 and S2.6.

Sequences were ordered as lyophilized powder from Integrated DNA Technologies (IDT). The **Reporter Top** and **Reporter Bottom** strands were ordered purified by high-performance liquid chromatography (HPLC) and all other strands were ordered impure with standard desalting. Strands were suspended in Millipore purified water to a concentration of ~1 mM and stored at -20°C. Empirical oligonucleotide stock concentrations were determined by assaying the absorbance (OD260) of 1000x diluted samples of each stock solution at 260 nm. The extinction coefficient provided by IDT was used to calculate stock concentrations using the Beer-Lambert law.

**Source**, **Delay** and **Reporter** complexes were prepared at a concentration of 100 µM in Tris-acetate-EDTA buffer with 12.5 mM $Mg^{++}$ (1x TAE/$Mg^{++}$). Each complex was annealed in an Eppendorf Mastercycler PCR by holding the solutions at 90°C for 5 minutes followed by cooling at -1°C per minute down to 20°C. After annealing, the **Source** complexes were incubated with 100 µM of their complementary **Initiator** strand overnight at room temperature to react with any poorly formed **Source** complexes. The **Source** complex was not incubated with any other strands or complexes due to the increased complexity of gel purification.

After annealing each complex and incubating the **Source** complexes overnight, all complexes were purified by polyacrylamide gel electrophoreses (PAGE). Ten percent polyacrylamide gels were cast by mixing 3.25 mL of 19:1 40% acrylamide/bis solution (Bio-Rad) with 1.3 mL 10x TAE/$Mg^{++}$ and 8.45 mL Millipore-purified $H_2O$. This solution was polymerized by the addition of 78 µL 10% ammonium persulfate (APS) and 5.4 µL tetramethylenediamine (TEMED) in a gel cassette with a large single well comb at the top of each gel. Fifteen percent polyacrylamide gels were prepared in a similar fashion except with a corresponding higher fractional volume of 40% acrylamide/bis stock solution. Two hundred microliters of annealed DNA complexes were mixed with 6x loading dye (New England Biolabs, product #B7021S) and loaded into the wells of the gels in a Scie Plas TV100K cooled vertical electrophoresis chamber. The gels were run at 150V and 4°C for 1.5 or 3 hours for 10% and 15% polyacrylamide gels. **Reporter** and **Delay** complexes were purified using 10% gels and the **Source** complex was purified using 15% gels. After running for the appropriate time, the bands were cut out using UV-shadowing at 254 nm for visualization. Bands were diced into ~1 $mm^3$ pieces, mixed with 500 μL of 1x TAE/$Mg^{++}$ buffer and were shaken on a vortexer overnight at room temperature. The DNA solutions were then transferred by pipet to a fresh tube leaving behind the gel pieces. The solutions were centrifuged for 5 minutes at 3000x*g* to precipitate any remaining gel pieces. The DNA solutions were transferred to a new tube and stored at 4°C until use. The concentrations of these purified complexes were then measured with an Eppendorf Biophotometer with a dilution factor of 30x using the approximate extinction coefficient ($\varepsilon$):

$$\varepsilon_{\text{Final}} = \varepsilon_{Top-strand} + \varepsilon_{Bottom-strand} - 3200N_{AT} - 2000N_{GC}$$

where $N$ indicates the number of hybridized A-T or G-C pairs in each complex.[69]

Reaction kinetics were measured on quantitative PCR (qPCR) machines (Agilent Stratagene Mx3000 and Mx3005 series) at 25°C. Reactions were prepared in 96-well plates using 150 μL/well volumes. Each well contained 1x TAE/$Mg^{++}$ and 2 μM Poly$T_{20}$ strands to help displace reactant species from the pipet tips used to add species and potentially from the well walls. In a typical experiment, Millipore-purified $H_2O$, TAE/$Mg^{++}$ and Poly$T_{20}$ strands were first mixed together. **Reporter** complexes were then added at 100 nM for System 1 or 200 nM for System 2. Baseline fluorescent measurements of the **Reporter** complex alone was conducted for each experiment for 0.5 to 1 hour with measurements every 1 to 10 minutes. This baseline was taken to be where the [**Output**] is equal to zero as detected by the **Reporter** and was subtracted from all subsequent data. After measuring this baseline, DNA strands or complexes were added to each well, depending on the experiment (see § 2.5.1-2.5.4). Fluorescence measurements were taken every 1-5 minutes for Delay characterization or every 5-10 minutes for Production characterization and Timer experiments.

## 2.5 SUPPORTING INFORMATION (SI)

### 2.5.1 Reporter Calibration

The **Reporter** complex (Figure 2.2c) was used to indirectly measure the concentration of the single-stranded **Output** strands in solution as a function of time. A **Reporter** that reacts reversibly with the **Output** species was used as an irreversible reporter could compete with the **Delay** species. The reporter follows the reaction:

$$\textbf{Reporter} + \textbf{Output} \underset{k_r}{\overset{k_f}{\rightleftharpoons}} \text{Fluorophore} + \text{Quencher} \tag{S2.1}$$

where the quencher-modified top strand of the **Reporter** complex is displaced by an invading strand causing in increase of fluorescence. The forward reaction rate constant, $k_f$, is expected to be around $5 \times 10^4$ $M^{-1}s^{-1}$.[36] Two calibrations were conducted to translate measured fluorescence intensities to levels of free **Output** concentration for each experiment. It was assumed that the measured fluorescence was proportional to the concentration of unquenched fluorophore, [**Fluoro.**] (*e.g.* Fluorophore in Eqn. S2.1), through a proportionality constant α. To determine α, we measured the fluorescence of the **Reporter** complex with known concentrations of the full complement (**FC**) to the bottom strand of the **Reporter** (see Table 2.1) and measured the change in fluorescence before and after addition of the complementary strand (Figure S2.1). In general, we used the equation

$$[\mathbf{FC}] = \alpha * \Delta\text{Fluorescence} + \beta \tag{S2.2}$$

for [**FC**] equal to 0, 25, 50, 75 and 100 nM. In the ideal case, $\beta$ is equal to zero. Alpha was determined by calculating the slope after fitting a line to [**FC**] vs. ΔFluorescence (Figure S2.1). This calibration enables the normalization of all fluorescence data into [**Fluoro.**]. Additionally, Figure S2.1 shows that photobleaching of the fluorophores are not a significant factor in measuring fluorescence as seen by the stable, non-decreasing intensity values.

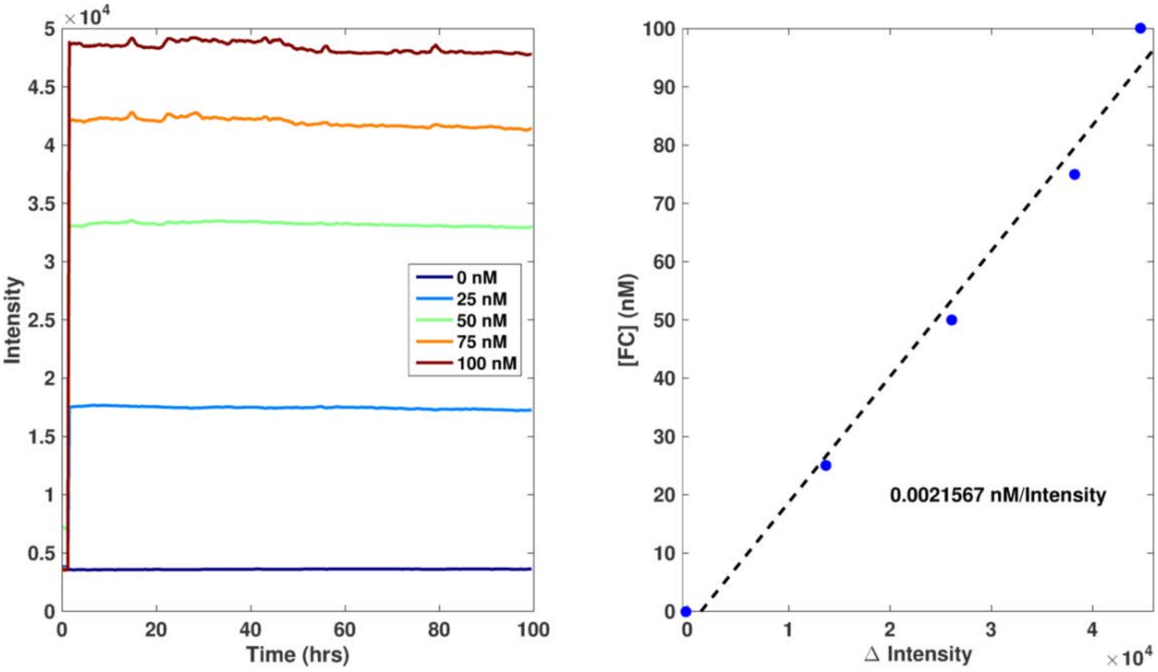

**Figure S2.1 Example calibration plots for the Reporter complex.** Example calibration plots for the **Reporter** complex with its full complement to convert raw intensity values into [**Fluoro.**]. **FC** was added to 100 nM **Reporter** at concentrations ranging from 0 – 100 nM as noted in the legend.

To convert the [**Fluoro.**] into [**Output**], the $K_{eq}$ for the reporter reaction shown in Eqn. 2.1 was calculated by mixing the **Reporter** complex with known concentrations of **Output** strand and using the equation:

$$K_{eq} = \frac{[\text{Fluoro.}]^2}{([\text{O}]_0 - [\text{Fluoro.}])([\text{R}]_0 - [\text{Fluoro.}])} \tag{S2.3}$$

where [**O**]$_0$ is the concentration of **Output** (*e.g.* 25, 50, 75 or 100 nM) added to the **Reporter** solution and [**R**]$_0$ is the initial **Reporter** complex concentration (*e.g.* 100 nM). In general, we found that the intensities measured with this calibration method decreased over the duration of the experiment (Fig. S2.2a), possibly due to **Reporter** complexes becoming stuck in the "off" state. Due to this decrease, the $K_{eq}$ was calculated as a function of time. The data was segmented into 75 bins (~1.3 hours each), with each bin having a $K_{eq}$ calculated as the average $K_{eq}$ over the [**Output**] tested (Fig. S2.2b,c).

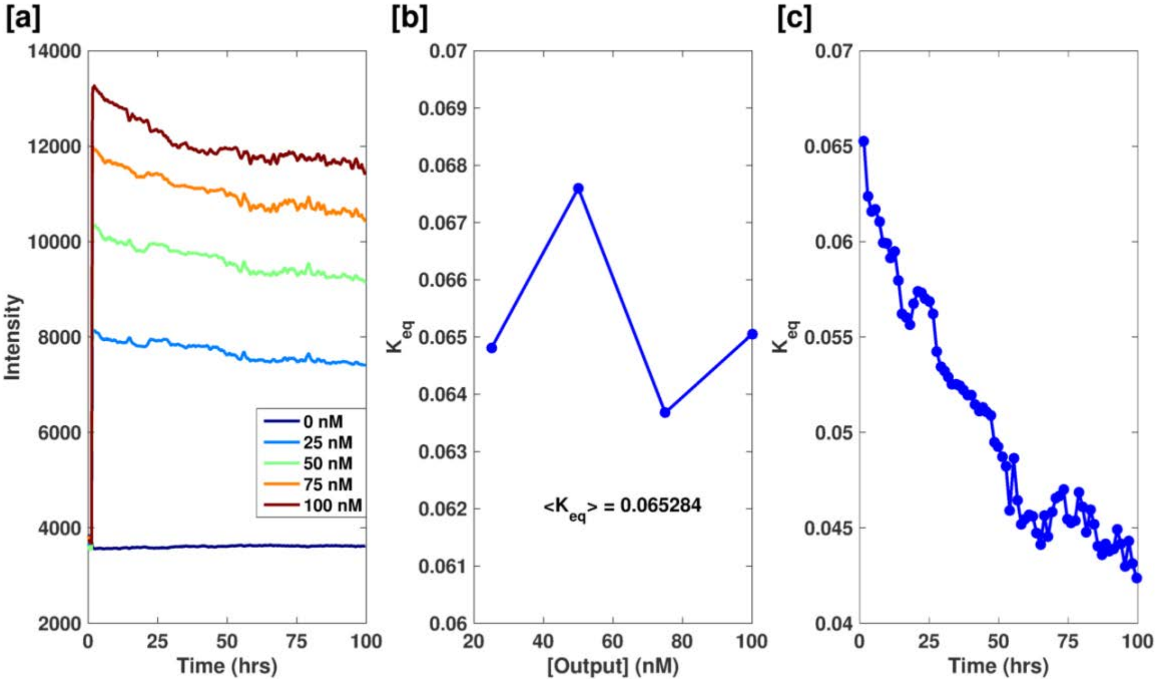

**Figure S2.2 Example calibration plots for the Reporter complex with the Output to convert [Fluoro.] values into [Output].** (a) **Output** was added to 100 nM **Reporter** at concentrations ranging from 0 – 100 nM as noted in the legend. (b) For each time segment, the $K_{eq}$ was calculated as the average value over the [**Output**]'s tested. Little variance was seen between the $K_{eq}$'s calculated at each [**O**] within a given time segment. The initial segment is shown (t = 1 hr). (c) The $K_{eq}$ decreases as a function of time. Each segment usually contained 1.3-1.5 hours of data.

The concentration of **Fluoro.** was then converted into [**Output**] through the equation

$$[\mathbf{O}] = \frac{[\mathbf{Fluoro.}]^2}{K_{eq}([\mathbf{R}]_0 - [\mathbf{Fluoro.}])} + [\mathbf{Fluoro.}] \tag{S2.4}$$

where [**Fluoro.**], [**O**] and $K_{eq}$ are functions of time. This equation reports the total concentration of **Output** as the sum of free **O** in solution and **O** that is transiently bound to the **Reporter** complex.

### 2.5.2 Production and Delay Reaction Characterization

To understand the timer system, we initially characterized the production reaction (between the **Source** and **Initiator** molecules) without a concurrent delay reaction. Multiple production reactions using various concentrations of **Initiator** and **Source** were conducted to calculate the forward and reverse reaction rate constants for the set of reactions shown in Figure S2.3. Two sets of reactions were conducted: [**S**]=[**I**] and [**S**]x[**I**]=1. In the first case, the production rate ($k_{prod}$) varies because the product of the initial concentrations of **Initiator** and **Source** is changing. In the second case, the production rate is theoretically constant between experiments on "short" time scales.

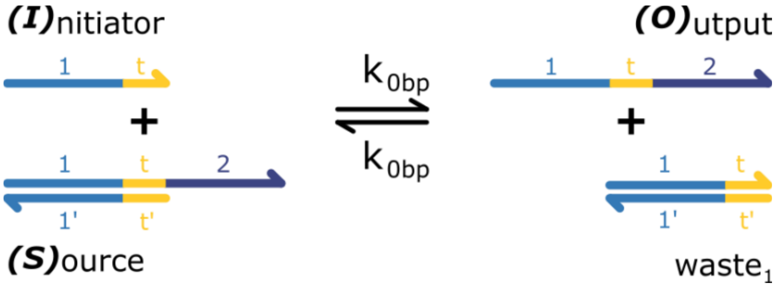

**Figure S2.3 Schematic for Production circuit.**The **Initiator** reacts with the **Source** complex through a fraying mechanism at the ends of the double-stranded regions to produce **Output** and **waste**$_1$. The forward and reverse reaction rate constant depend on DNA sequence and the point of strand-displacement initialization and thus could be different values, but for simplicity a single rate constant, $k_{0bp}$, was chosen.

The **Source** and **Reporter** were incubated for about 6 hours until the measured intensity reached a steady state prior to the addition of **I**. This steady state intensity is thought to be a small population of free **Output** left over from the purification process, although interactions between the **Source** and **Reporter** complexes may exist. The concentration of detected **Output** by the **Reporter** corresponded to 0.01-0.02x[**Source**] used in each experiment (Figure S2.4).

The post-initiation reaction curves were fit using MATLAB to initially calculate $k_{0bp}$ for this set of reactions using the second-order reaction kinetics equation:

$$\frac{d[\boldsymbol{O}]}{dt} = k_{0bp}[\boldsymbol{I}][\boldsymbol{S}] - k_{0bp}[\boldsymbol{O}][\boldsymbol{waste_1}] \qquad \text{(S2.5)}$$

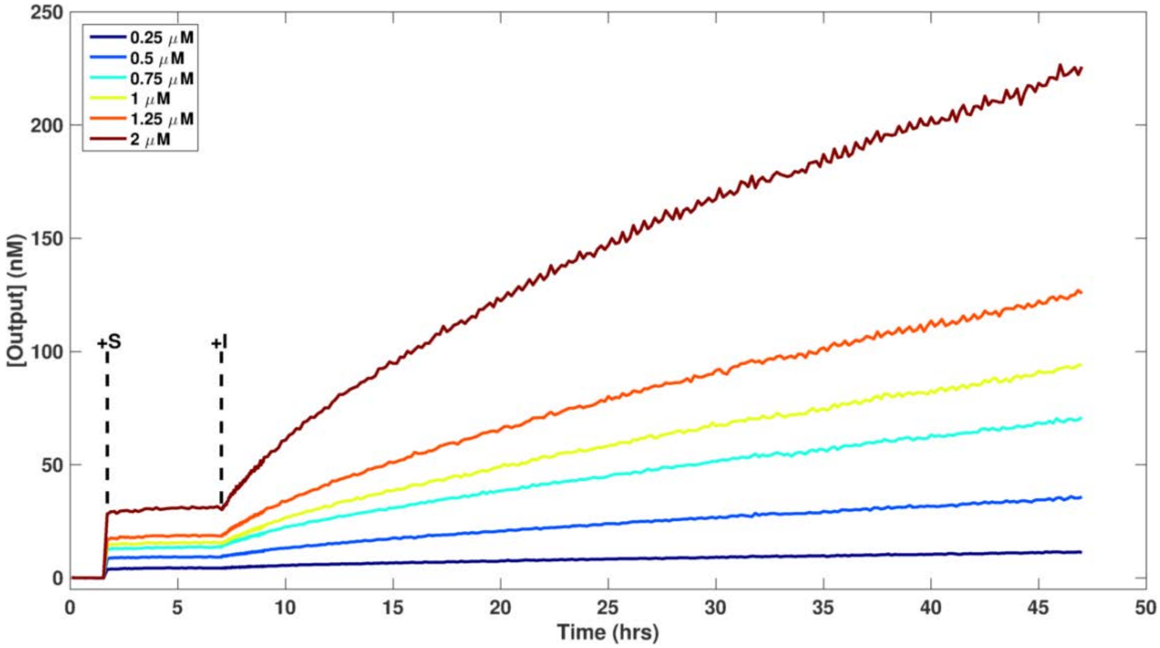

**Figure S2.4 Characterization of the effect of [Source] and [Initiator] on the observed release of Output.** The **Source** is mixed with the **Reporter** after 1.5 hours and incubated for about 6 hours, when the **Initiator** is added (denoted by black dashed lines). For the curves shown, [**S**] is equal to [**I**] and is shown in the legend. The concentration of initial **Output** detected prior to initiation scales with the amount of [**S**] added. Data is identical to that shown in Fig. S2.5a and Fig 2.3a.

The **Reporter** reaction was not included in the fitting procedure because its equilibration kinetics were assumed to be much faster (~$10^5$x faster reaction rate constant) than that of the Production reaction. However, the reaction rate constants calculated from this model did not capture the dynamics seen in Fig S2.5a,b - *i.e.* a quick release of **O** followed by a slower, more linear region. We hypothesized that this was due to a small concentration of **Source** that reacted quickly and irreversibly with the **Initiator** present in the reaction volumes, perhaps because of errors in sequence produced during solid state DNA synthesis. We call this small population [**S**]$_{\text{Leak}}$ which reacts with reaction rate constant $k_{Leak}$. To account for this possibility, we used the following equation to generate a better fit to the experimental data:

$$\frac{d[\boldsymbol{O}]}{dt} = k_{0bp}[\boldsymbol{I}][\boldsymbol{S}] - k_{0bp}[\boldsymbol{O}][\boldsymbol{waste_1}] + k_{Leak}[\boldsymbol{S}]_{Leak}[\boldsymbol{I}] \tag{S2.6}$$

and to calculate the model parameters $k_{0bp}$, $k_{Leak}$ and [**S**]$_{\text{Leak}}$. Additional information regarding $\mathbf{S}_{\mathbf{Leak}}$ can be found in § 2.5.6. An example of such a fit is shown in Figure S2.5c and the fit parameters are compiled in Table S2.1. The average $k_{0bp}$ was 0.49±0.13 $M^{-1}sec^{-1}$ which is in good agreement with the reported value of 0.5 $M^{-1}sec^{-1}$.[36] [**S**]$_{\text{Leak,0}}$ varied from 0.5 to 4.7% of [**S**]$_0$.

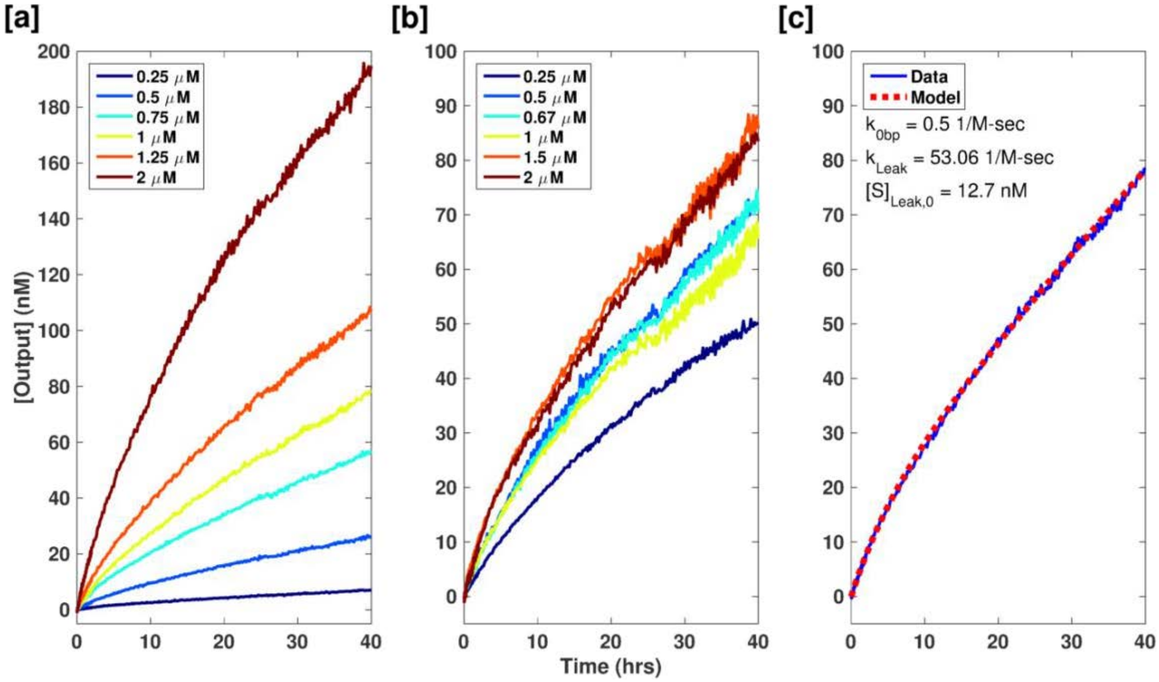

**Figure S2.5 Characterization of Production reactions.** Production reactions were measured for [**Source**] = [**Initiator**] in the range of 0.25-2 µM (a) and for [**S**] x [**I**] = 1 (b). The legend in (b) shows the concentration of **Source** in the reaction mixture. (c) Example comparison between experimental measurements and the model resulting from the fit of reaction rate constants for [**S**]=[**I**]=1 µM. Reaction curves were fit using a bimolecular reaction kinetics model to calculate a second-order reaction rate constant. Reaction rate constants for each curve are listed below in Table S2.1.

As shown in Figure S2.5a, the production rate varied with the concentrations of **Source** and **Initiator**. From Equation 2.5, the production rate is expected to follow a power law ($k_{Prod} \sim [\boldsymbol{S}]_0^2$) when initial concentrations of **S** and **I** are equal. The experimentally determined production rate increased to the exponential of 1.6 with increasing **S** and **I** instead of 2. There was also a small variation in the production rate for the case [**S**]x[**I**]=1, where the initial $k_{prod}$ was expected to be constant among the reaction conditions tested (see Table S2.1). The deviation from the expected result in both cases could be due to other undesired reactions present in between reaction species.

The Delay circuit module was characterized by the degree to which the **Delay** complex was able to sequester free **Output**. The kinetics of the reaction between **Delay** and **Output** was too fast to capture using the concentration ranges tested in order to fit reaction rate constants for the set of reactions show in Figure S2.6. The Delay reaction is slightly reversible due to 2 extra bases on the **Delay** complex that are not complementary to the **Output** (shown in green). These bases are important for decreasing undesired reactions between the **Source** and **Delay** complexes, whose reaction rate constant is on the same order as the

Production circuit (initialized *via* fraying). However, this reaction set is expected to be very forward reaction dominated since $k_{forward}$ ~2x$10^6$ 1/M-sec and $k_{reverse}$ ~$10^2$ 1/M-sec.[4]

**Table S2.1 Reaction rate constants for the Production reactions shown in Fig. S2.5.** The production rate constant ($k_{prod}$) was calculated using Equation 2.5 with the initial concentrations of **Source** and **Initiator**. Values listed are result of fit with 95% confidence interval bounds. Overall values are the average and standard deviation of all rows ($k_{0bp}$) or rows in the [**S**]x[**I**]=1 set of experiments ($k_{prod}$).

| Experiment Type | [S] (μM) | [I] (μM) | $k_{0bp}$ (1/M-sec) | $k_{prod}$ (nM/hr) | $k_{Leak}$ (1/M-sec) | [S]$_{Leak}$ (nM) |
|---|---|---|---|---|---|---|
| [S]=[**I**] | 0.25 | 0.25 | 0.676±0.008 | 0.152±0.002 | 336±20 | 1.3±0.1 |
| | 0.5 | 0.5 | 0.645±0.006 | 0.58±0.005 | 129±7 | 4.6±0.2 |
| | 0.75 | 0.75 | 0.647±0.004 | 1.311±0.009 | 91±4 | 8.8±0.2 |
| | 1 | 1 | 0.501±0.004 | 1.803±0.014 | 53±2 | 12.7±0.4 |
| | 1.25 | 1.25 | 0.439±0.004 | 2.47±0.021 | 43±2 | 19.0±0.6 |
| | 2 | 2 | 0.279±0.005 | 4.016±0.066 | 20±1 | 53.8±2.0 |
| [S]x[**I**]=1 | 0.25 | 4 | 0.32±0.01 | 1.14±0.02 | 8±1 | 11.7±0.8 |
| | 0.5 | 2 | 0.46±0.01 | 1.67±0.02 | 27±2 | 13.2±0.6 |
| | 0.67 | 1.5 | 0.46±0.01 | 1.65±0.02 | 35±3 | 12.6±0.6 |
| | 1 | 1 | 0.39±0.01 | 1.41±0.03 | 52±4 | 14.1±0.7 |
| | 1.5 | 0.67 | 0.53±0.01 | 1.91±0.03 | 96±6 | 18.2±0.8 |
| | 2 | 0.5 | 0.55±0.01 | 1.97±0.02 | 129±7 | 15.9±0.6 |
| **Overall** | | | 0.5±0.1 | 1.6±0.3 | | |

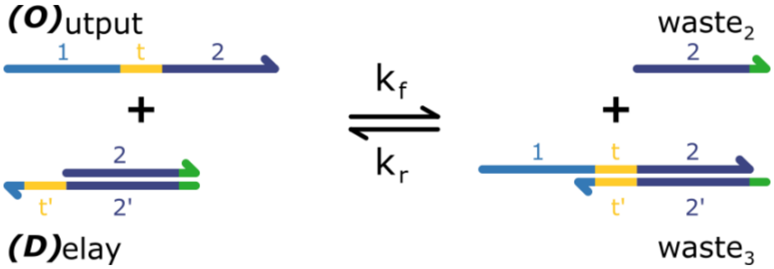

**Figure S2.6 Schematic for the Delay circuit.** The **Output** reacts with the **Delay** complex through a 7 base-pair toehold to produce two waste species. Two extra bases on the **Delay** complex (shown in green) inhibit a leak reaction between **Source** and **Delay** complexes.

Two sets of experiments were run to investigate whether the **Delay** complex efficiently sequestered **Output** in a reaction solution. The first set was run by adding **D** at various concentrations to the **Reporter** followed by the addition of **O**. As shown in Fig. S2.7a, the concentration of **O** detected closely matched the expected result: [**O**] = [**O**]$_0$-[**D**]. The second set of experiments was run by first adding **O** to the **Reporter** followed by the addition of **D**, leading to a sudden decrease in fluorescence intensity and detected free **O** (Fig. S2.7b). Again, the remaining [**O**] matched the expected concentrations determined by the amount of **D** added. The concentration of **O** remaining when the **D** exceeded the initial concentration of **O** added did not fully decrease to zero due to the reversibility of the Delay reaction (Fig. S2.6).

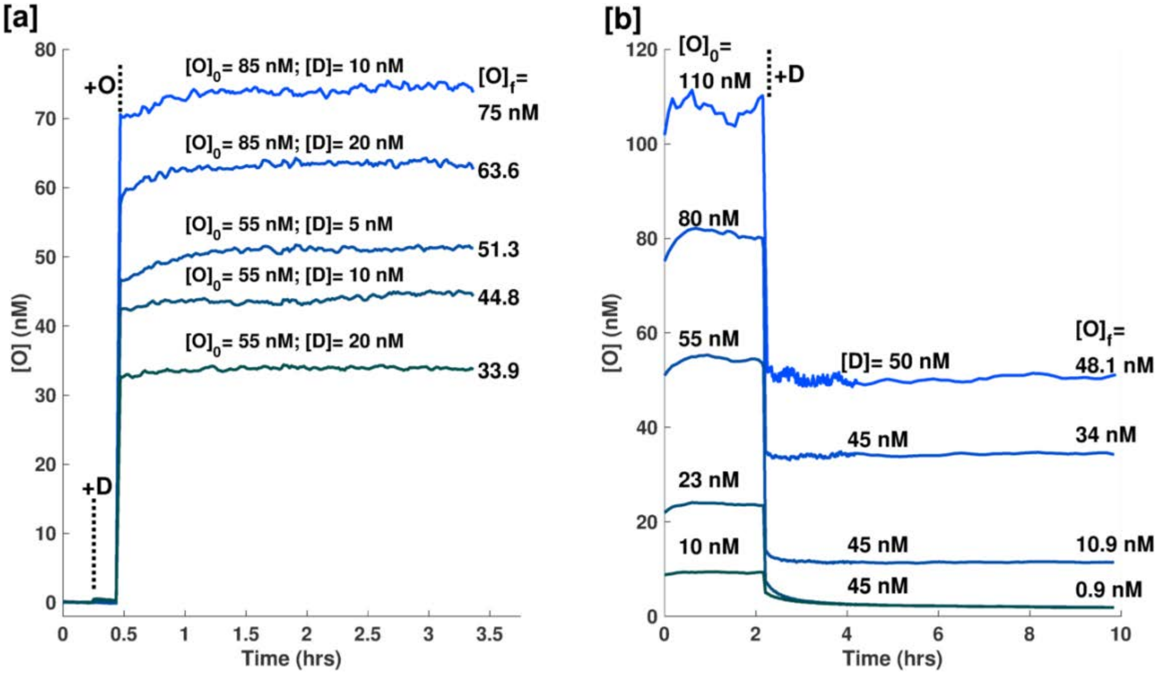

**Figure S2.7 Characterization of the Delay circuit.** (a) **O** is added to **R** and **D** leading to a rise in detected **O** by the **Reporter**. Black dashed lines indicate the times **D** or **O** is added to the **Reporter** solution. The concentration of **O** and **D** added to each reaction mixture is annotated above each trace. $[\mathbf{O}]_f$ is the average [**O**] over the last 30 data points. (b) **D** is added to **Reporter** and **O** leading to a decrease in fluorescence as **O** is being sequestered by **D**. The data in Fig. 2.3b is calculated from the data shown here in (a) and (b).

### 2.5.3 Timer Experiments with System 1

Timer experiments were conducted similar to Production experiments, except both **Source** and **Delay** were mixed with the **Reporter** after the initial baseline was measured (~1 hour). **Initiator** was mixed into the wells after the intensity reached a steady-state, at about 22-24 hours. Both **S** and **I** were kept equal in these experiments. From Table S2.1, [**S**]=[**I**]=1 µM produces **Output** at ~1.8 nM/hr, [**S**]=[**I**]=0.5 µM at ~0.6 nM/hr and [**S**]=[**I**]=0.25 µM at ~0.15 nM/hr (Fig. 2.3c,d and Figs. S2.8-S2.10).

The delay time ($t_{\text{Delay}}$) was determined by calculating a moving linear fit of each curve post-**Initiator** addition. The span of each fit included 100 or 60 data points, depending on the reaction conditions. The step size was ½ of the span in each case (50 and 30 points). The x-intercept from the fit with the largest slope was chosen as the delay time. Other algorithms (*e.g.* the time [**O**] or d[**O**]/dt surpasses a specified value) gave similar time delays, but were more sensitive to noise/bias.

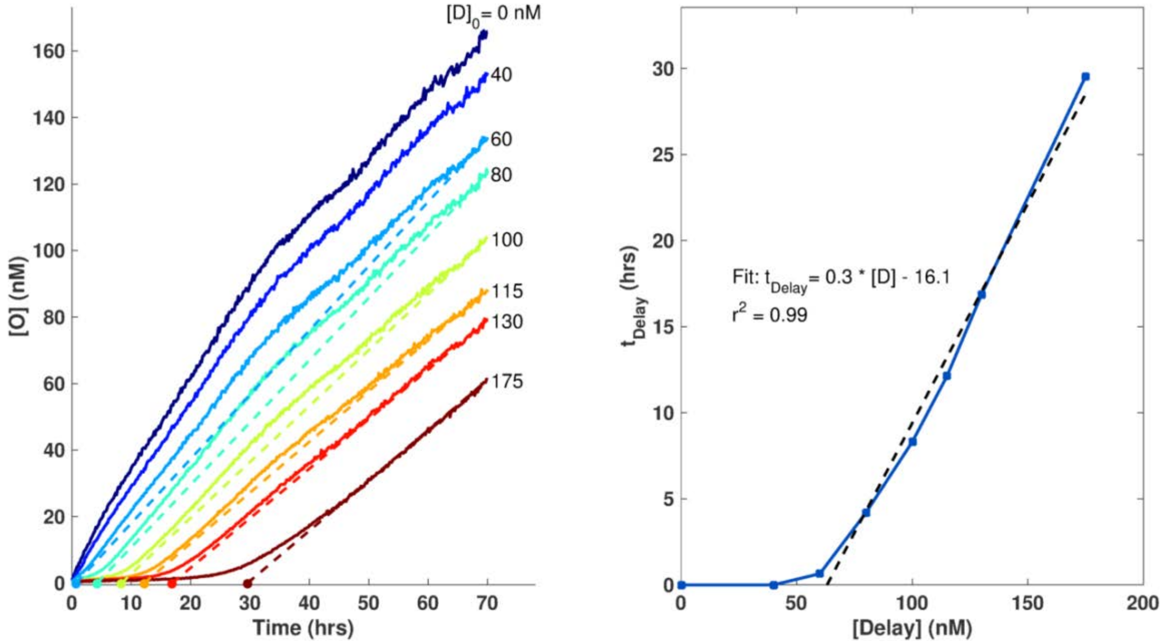

**Figure S2.8 [Output] vs. time and $t_{Delay}$ vs. [Delay] for reactions using [S]=[I]=1 μM production conditions for System 1.** Dashed lines in the left plot are guides showing the calculated time delay. Dashed line in the right plot shows a linear fit for points with $t_{Delay}$ greater than zero. Data is the same as in Figure 2.3c,d.

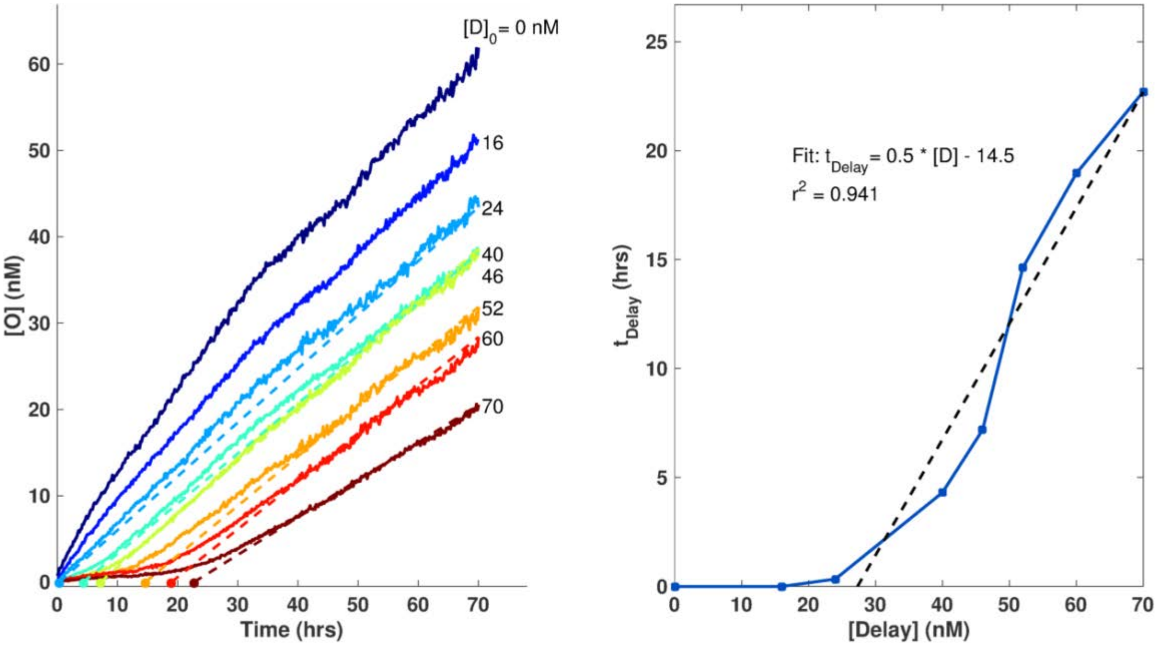

**Figure S2.9 [Output] vs. time and $t_{Delay}$ vs. [Delay] for reactions using [S]=[I]=0.5 μM production conditions for System 1.** Dashed lines in the left plot are guides showing the calculated time delay. Dashed line in the right plot shows a linear fit for points with $t_{Delay}$ greater than zero.

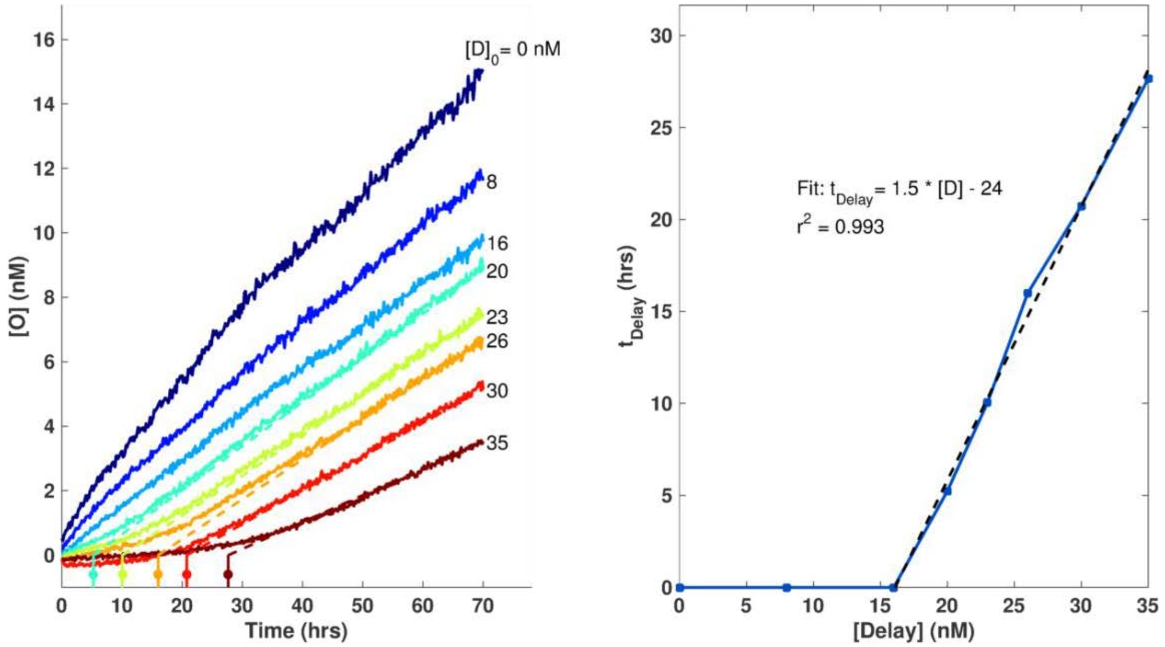

**Figure S2.10 [Output] vs. time and $t_{Delay}$ vs. [Delay] for reactions using [S]=[I]=0.25 µM production conditions for System 1.** Dashed lines in the left plot are guides showing the calculated time delay. Dashed line in the right plot shows a linear fit for points with $t_{Delay}$ greater than zero.

The rate of production (d[**O**]/dt) was calculated for each reaction condition. The slope of each curve was calculated as the average over the last 90 data points (15 hours). We found that the production rate at that time point decreased slightly as a function of [**Delay**], possibly due to the uncharacterized reactions mentioned elsewhere. Despite the **Delay** dependent effects observed, an appropriate [**Delay**] can be chosen from a desired production rate and time delay using Table S2.1 and Figure S2.11.

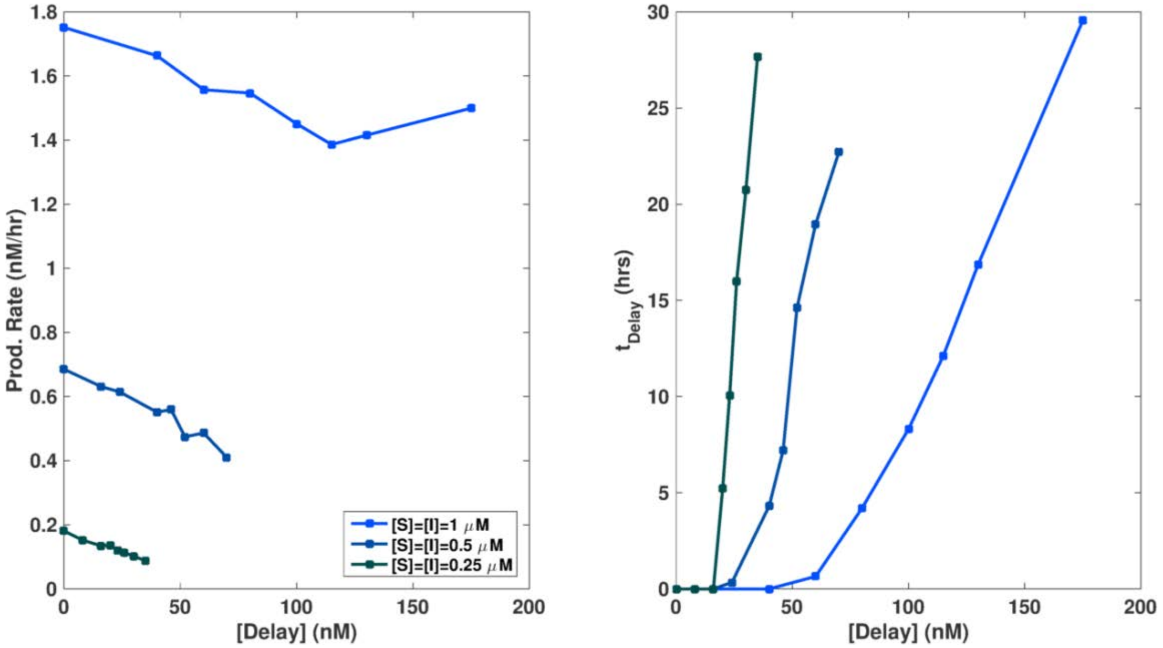

**Figure S2.11 Production rate vs. [Delay] and $t_{Delay}$ vs. [Delay] for System 1.** Production rate was calculated as the average over the last 90 data points (15 hours). Production rate decreases with [**Delay**] due to possible undesired reactions between circuit components.

### 2.5.4 Timer Experiments with System 2

Experiments for System 2 were conducted the same as with System 1 except with a [**Reporter**] of 200 nM. **Output** production from System 2 was found to be slower than with System 1 (Figs. S2.12-S2.14). This could be due to DNA sequence differences between the systems; notably the toehold domain of System 2 is expected to have weaker binding than that of System 1 because it has less G-C base content. The 7bp toehold of the **Delay** complex is weaker as well. Additionally, if there are significant interactions between the **Source** or **Delay** and the **Reporter** complex, the increased **Reporter** concentration could be an attributing factor. Finally, while System 1 had a decrease in production rate with increasing [**Delay**], System 2 showed an increase in production rate (Fig. S2.15).

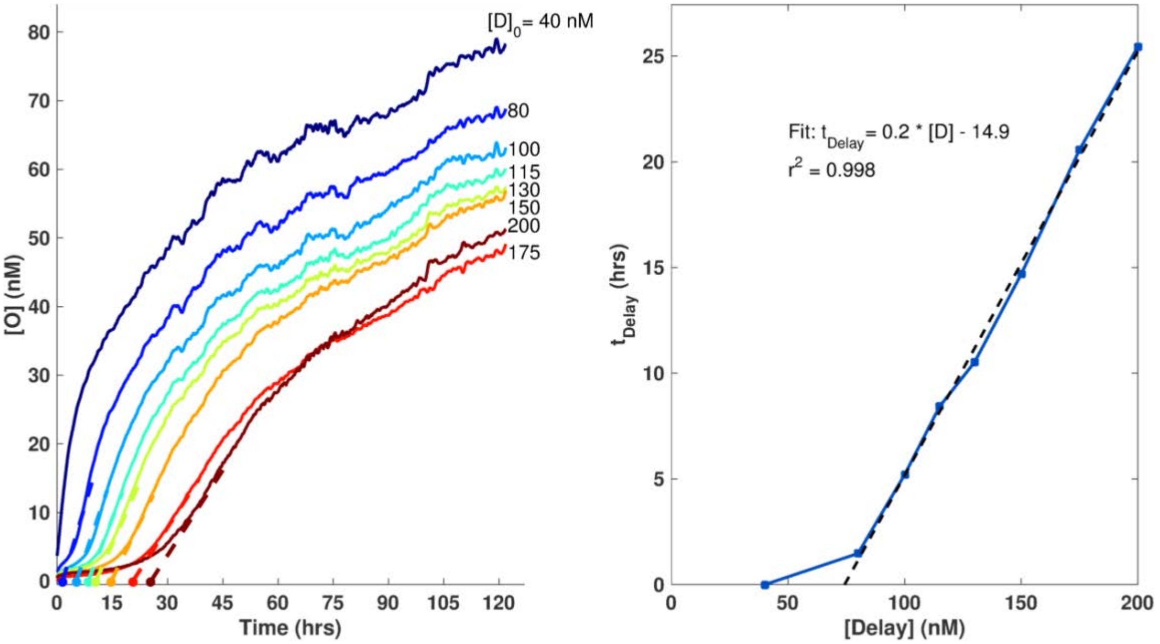

**Figure S2.12 [Output] vs. time and $t_{Delay}$ vs. [Delay] for reactions using [S]=[I]=1 μM production conditions for System 2.** Dashed lines in the left plot are guides showing the calculated time delay. Dashed line in the right plot shows a linear fit for points with $t_{Delay}$ greater than zero.

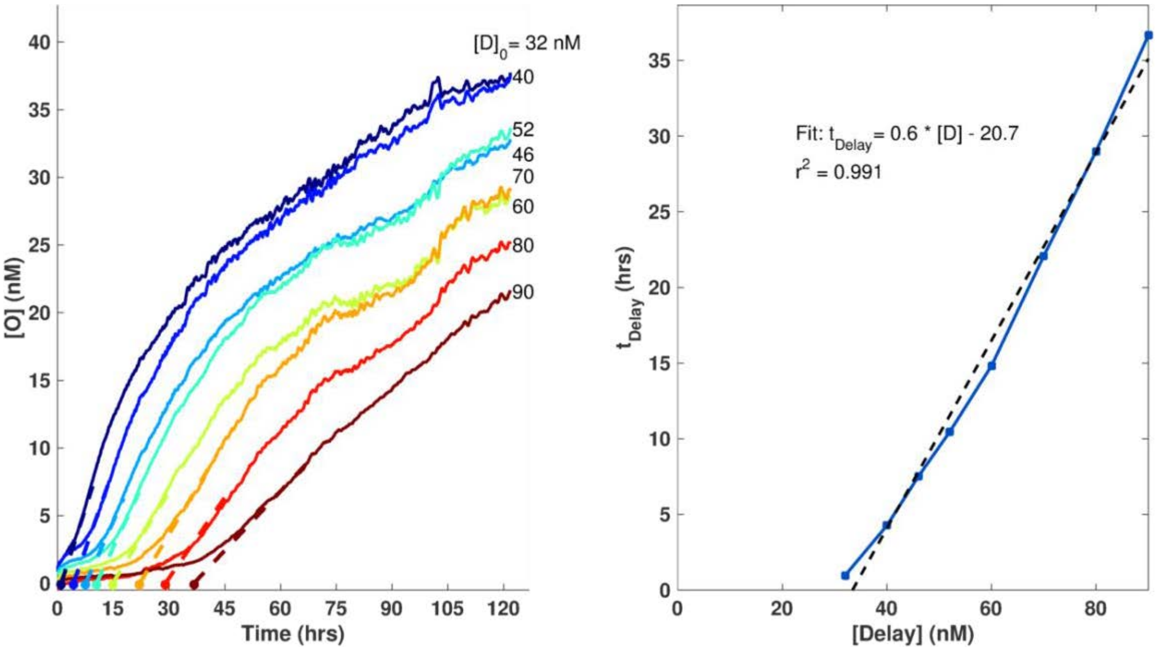

**Figure S2.13 [Output] vs. time and $t_{Delay}$ vs. [Delay] for reactions using [S]=[I]=0.5 μM production conditions for System 2.** Dashed lines in the left plot are guides showing the calculated time delay. Dashed line in the right plot shows a linear fit for points with $t_{Delay}$ greater than zero.

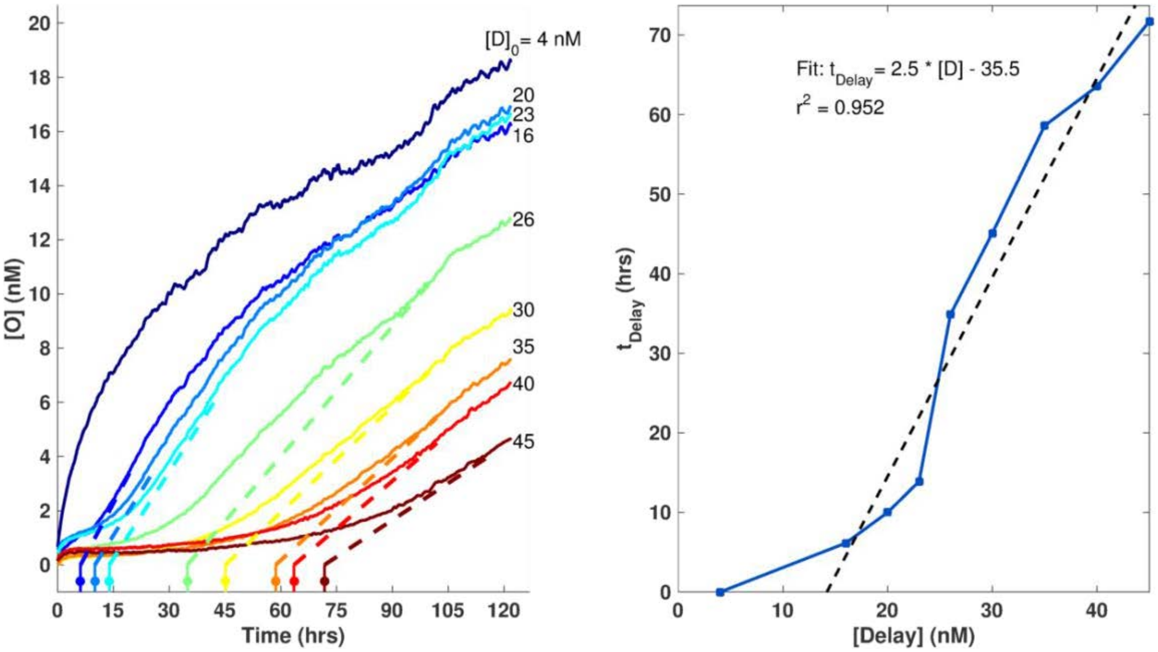

**Figure S2.14 [Output] vs. time and $t_{Delay}$ vs. [Delay] for reactions using [S]=[I]=0.25 µM production conditions for System 2.** Dashed lines in the left plot are guides showing the calculated time delay. Dashed line in the right plot shows a linear fit for points with $t_{Delay}$ greater than zero.

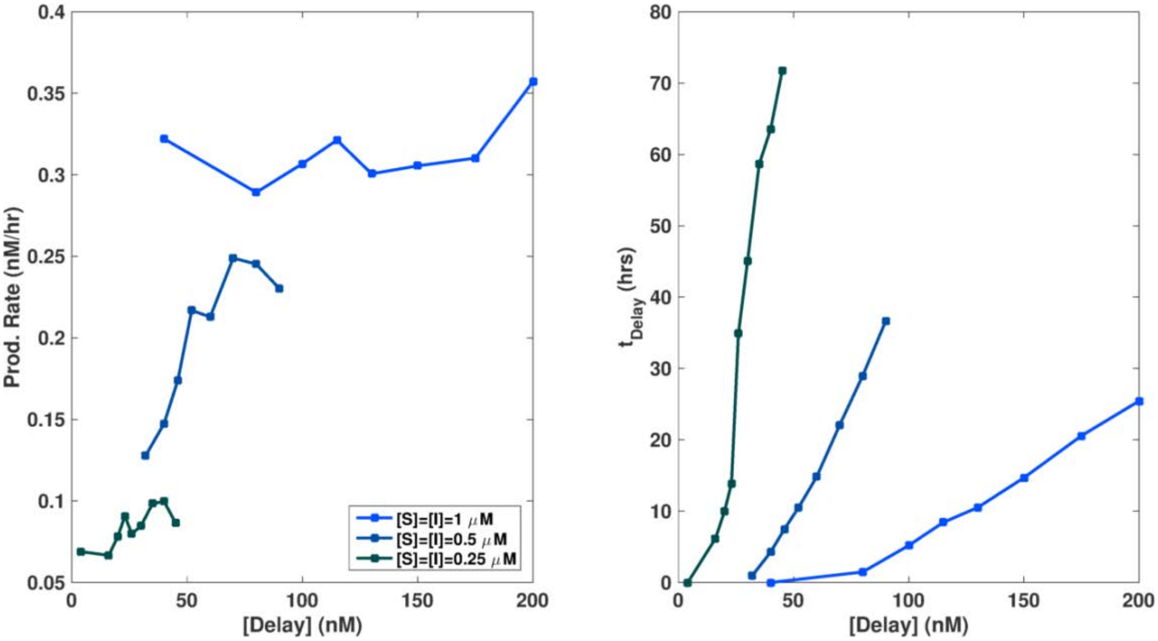

**Figure S2.15 Production rate vs. [Delay] and $t_{Delay}$ vs. [Delay] for System 2.** Production rate was calculated as the average over the last 250 or 100 data points (about 40 or 16 hours). Production rate increases with [**Delay**] due to possible undesired reactions between circuit components.

### 2.5.5 Multiplex Timer Experiments (Systems 1 and 2)

Multiplexing experiments were conducted the same as the experiments described in SI 2.5.3-2.5.4. Briefly, the **Reporters** of each system were mixed and a baseline was taken followed by the addition of **Delay** and **Source** complexes. **Initiator** was added after 22-24 hours. For experiments comparing data of each system in isolation *vs*. together, the reaction solution contained **Reporters** from both systems, but only the **D**, **S** and **I** from the system being studied (dashed lines in Fig. S2.16). System 1 was tracked using FAM and System 2 with TexasRed fluorophores using two different filters on the qPCR. Fluorescence from one fluorophore was not observed when measuring the fluorescence of the other fluorophore.

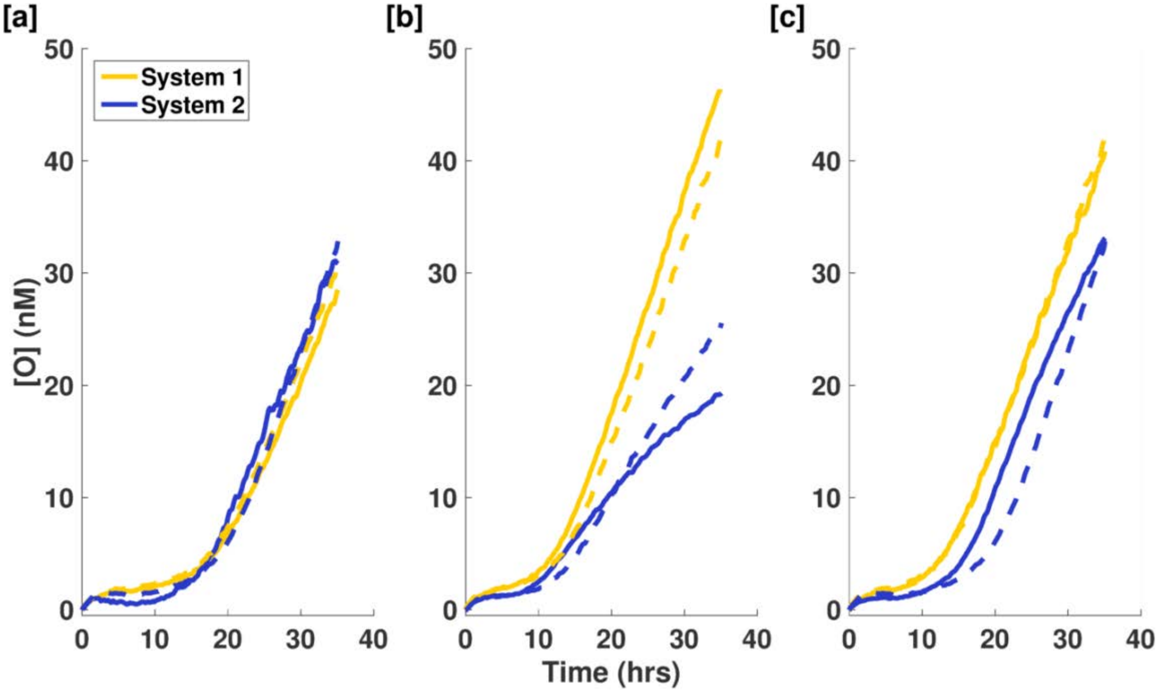

**Figure S2.16 Additional examples of multiplexing two timer circuits.** In each case, dashed lines indicate a reaction with the system in isolation. (a) Reaction mixture conditions were chosen such that both systems would release their respective O at the same time (19 hours) and rate. [**S**]$_0$=[**I**]$_0$=1 µM; {[**D**]$_{Sys1}$, [**D**]$_{Sys2}$}={130 nM, 165 nM}. (b) The release rate of each system can be independently controlled while keeping the delay time constant (9 hours). [**S**]$_0$=[**I**]$_0$=1 µM for Sys1 and 0.5 µM for Sys2; {[**D**]$_{Sys1}$, [**D**]$_{Sys2}$}={100 nM, 50 nM}. (c) The time of release (9 and 19 hours) of each system can be independently controlled while keeping the release rate constant. [**S**]$_0$=[**I**]$_0$=1 µM; {[**D**]$_{Sys1}$, [**D**]$_{Sys2}$}={100 nM, 165 nM}.

### 2.5.6 Timer Circuit Simulations and Characterization of Leak Reactions

Since the DNA strand-displacement circuit can be represented by a series of mathematical equations (Equations S2.1 and S2.5 and Figure S2.6), a model that matches the experimental behavior of the system could be built to further tune the circuit for future applications. However, we found that a simple model derived from those equations failed to quantitatively capture the delay times observed in experiments (Fig S2.17). Based on that mismatch and the observation of an increase in fluorescence (or detected **O**) by the **Reporter** when **S** is added in the absence of **I** or **D** (Figure S2.4), we postulated that a series of interactions might exist between **S**, **D**, **I** and **Reporter** beyond what is predicted by the simple model.

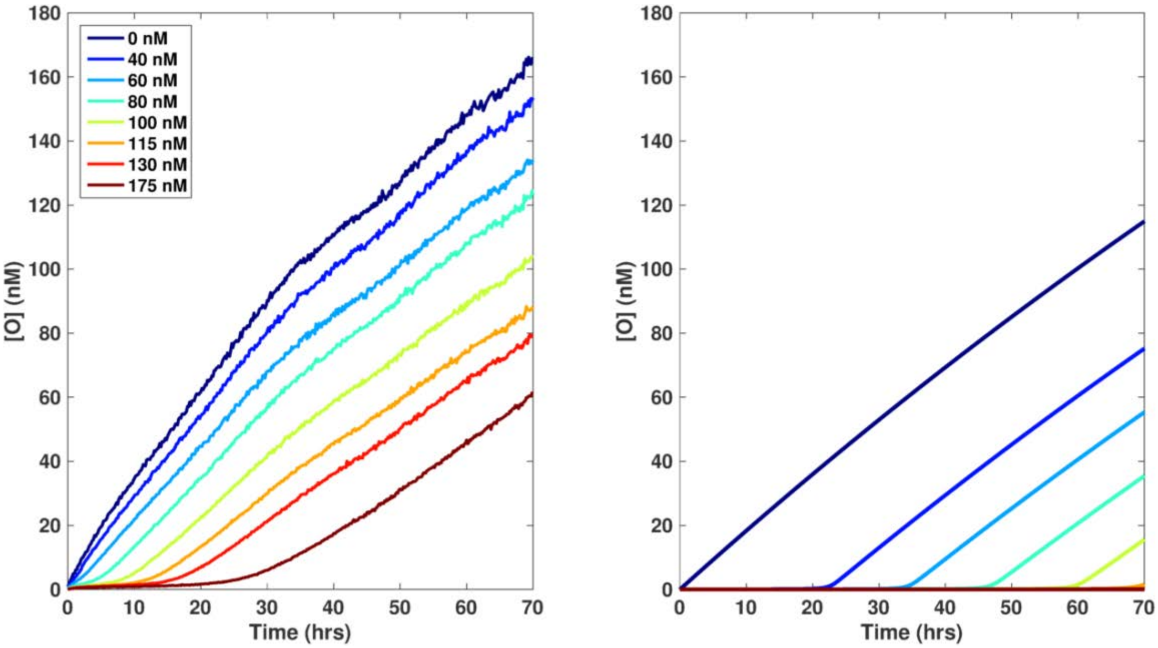

**Figure S2.17 Comparison of data and model considering only abstract reactions.** Comparison of data (left) and a model considering only abstract reactions described in Eqn. S2.5 and Fig. S2.6 (right) for System 1 using 1 µM **S** and **I**. **Delay** concentrations for both plots are shown in the legend. Parameters for the model were as described in SI 2.5.2 (Figs. S2.3,S2.6) and in Zhang and Winfree.[36] Note the decrease in overall production and increase in time delay of the model prediction compared to experimental results.

In control experiments, we found that mixing the **Reporter** and **Source** quickly produced an observable fluorescence signal in the absence of **Initiator** (Fig. S2.4), suggesting that the **Source** complex and the **Reporter** interacted in an undesired or “leak” reaction (Fig. S2.18a). While by design these species could interact through a 4-way 0bp pair branch migration interaction, such a pathway would not explain the fast rate of reaction we observed. We therefore postulated that this reaction could be due to truncations or base mismatches within the toehold region of the bottom strand of some **S** complexes. We designated **S** complexes with these variations as the subspecies $\mathbf{S_{Leak}}$. These complexes would not have been separated from pure **S** complex during the purification process because their electrophoretic mobility is very similar to that of **S**.

We also observed that some leftover **O** remained after the gel purification process due to the proximity of the bands in the gel. Purifying **S** using a 15% polyacrylamide gel instead of a 10% gel significantly reduced the level of pre-initiation **O** detected, but some may still remain in the purified **S** complex solution. The leftover **O** and $\mathbf{S_{Leak}}$ complex are also expected to interact with the **Delay** complex for timer circuit reactions. We also considered a leak reaction between the **Initiator** and the **Delay** complex since there are 7 complementary nucleotides for a transient hybridization. The schematic shown in Figures S2.18-S2.20 shows the possible leak reactions considered here. Unless specified in the figure captions, reaction rate constants for these reactions were taken from Zhang and Winfree,[36] or fit using the bimolecular rate equation shown in SI 2.5.2 and Figure S2.5. This approach of choosing reaction rate constants supports a physical representation of the postulated reactions and provides consistency with studies of other DNA strand-displacement reactions.

While the reactions described above may account for the unintended reactions that occurred within the timer system, including these reactions in a model still predicted significantly different time delay values than what were observed experimentally. To account for the decreased time delay observed in experiments, we added a small leak reaction between pure **Source** complexes and **Delay** complexes. While such a reaction would be expected to occur with a rate constant smaller than $k_{0bp}$, a reaction rate constant of $k_{1bp}$ was needed to account for the large decrease in delay time. As noted in § 2.5.2, we found that a reaction between $\mathbf{S_{Leak}}$ and **I** produced a better fit to the production dynamics. However, we would not expect this reaction to occur since **S** and **I** are incubated prior to PAGE purification of the **S** complex, any **S** species that would quickly react with **I** would be removed. Figure S2.19 shows an example comparison between experimental data (System 1, [**S**]=[**I**]=1 μM) and the resulting model prediction. While these reactions are only a possible description of the interactions between the DNA species, they show that an understanding of the reaction behavior is possible through the incorporation of leak pathways. We found that incorporation of each of these leak pathways into our model, using previously published rates and the fitted parameters of [$\mathbf{S_{Leak}}$], $k_{S,Leak}$ and $k_{0bp}$ as described in § 2.5.2 (no additional fitting parameters were required) produced quantitative agreement between our model and the experimental results that we observed (Fig. S2.21). Thus, we expect that this model can be used to tune the system's performance, including release rates and delay times.

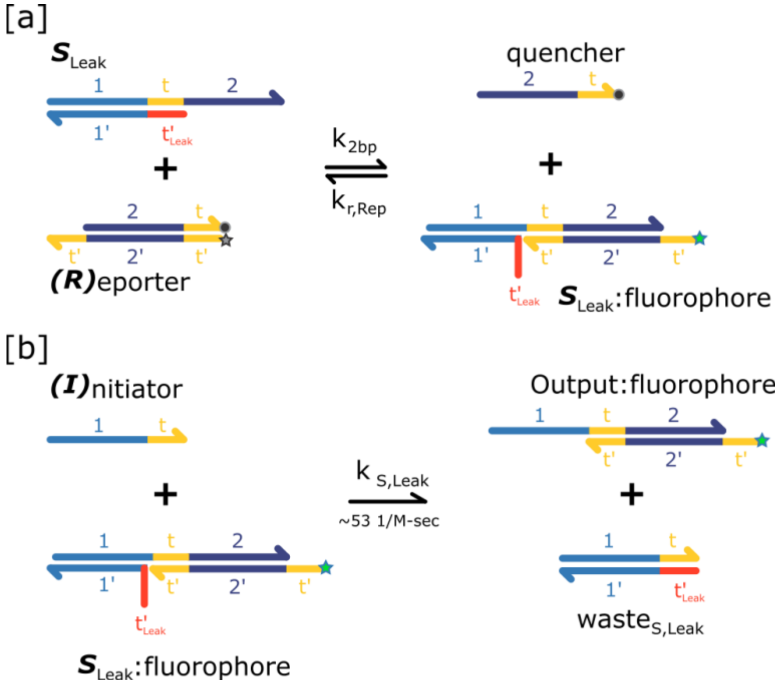

**Figure S2.18 Reactions between a Source complex with mismatches or base truncations in the toehold region and the Reporter complex lead to the detection of a fluorescent signal prior to the addition of the Initiator.** (a) **$\mathbf{S}_{\mathbf{Leak}}$** complex interacts reversibly with the **Reporter** to produce a fluorescent complex that reacts irreversibly with the **Initiator** (b). $k_{r,rep}$ was calculated from $k_{5bp}$ (see Zhang and Winfree[36]) and the experimentally measured $K_{eq}$ of the **Reporter-Output** reaction (Fig. S2.2).

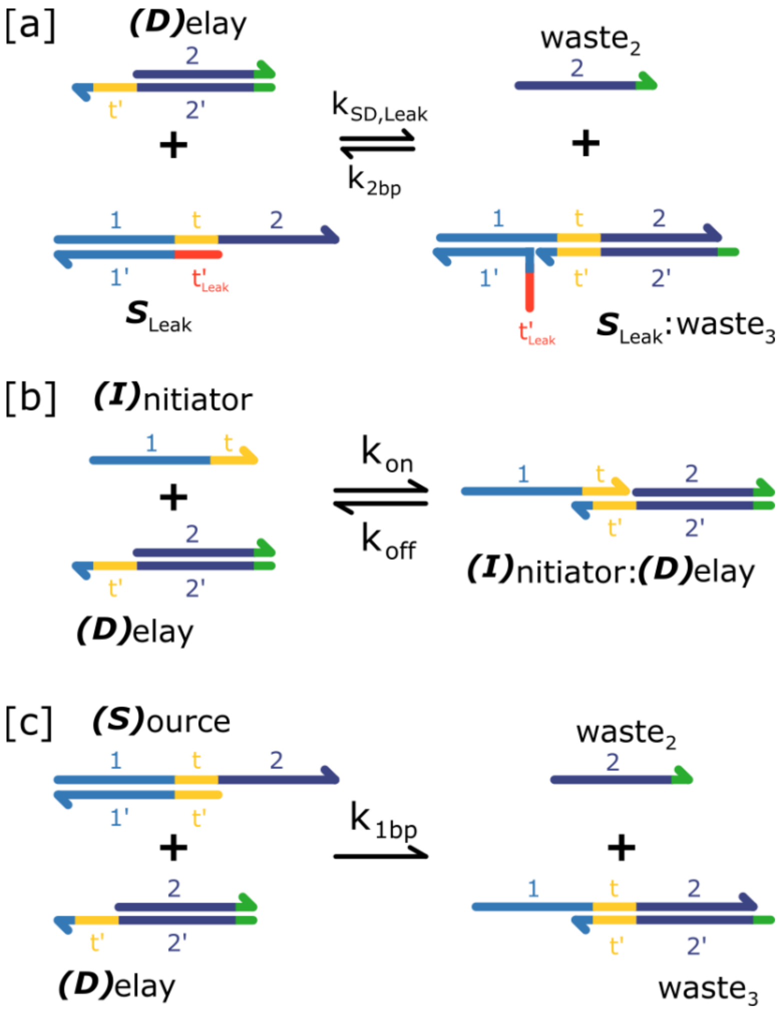

**Figure S2.19 Reactions between the Delay complex and other reaction species.** (a) **Delay** and $\mathbf{S_{Leak}}$ react reversibly with a forward rate constant estimated to be $k_{SD,Leak}$ ~250 1/M-sec. (b) **Initiator** hybridizes and de-hybridizes with the toehold of the **Delay** complex. From Zhang and Winfree,[36] $k_{on}$ ~ 3.5E6 1/M-sec and $k_{off}$ ~ 0.08 1/sec. (c) Leak reaction between pure **Source** complex and the **Delay** complex.

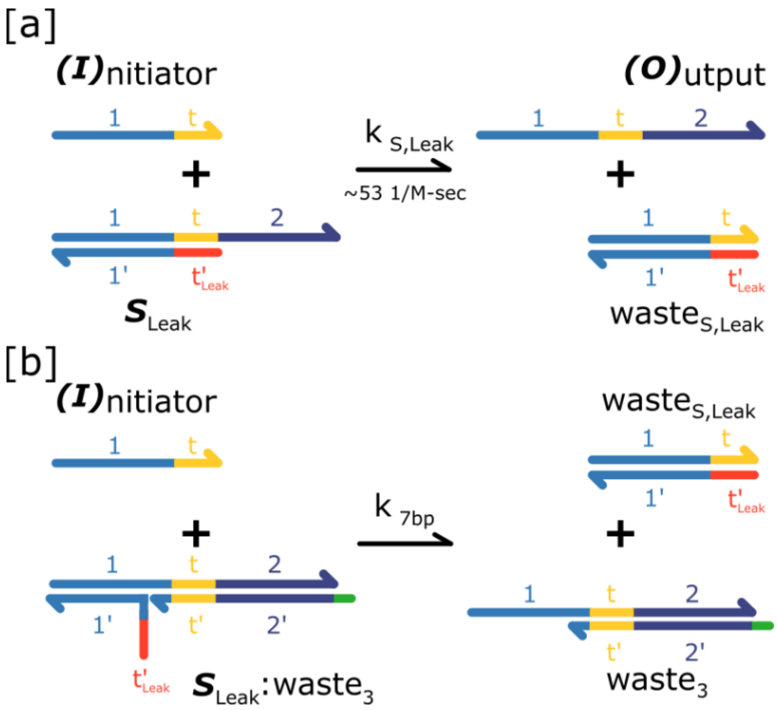

**Figure S2.20 Reactions between the Delay complex and other reaction species.** Leak reactions with **Initiator**. (a) Reaction between **I** and **S$_{Leak}$**. (b) Reaction between **I** and the complex produced from **S$_{Leak}$**+**D**.

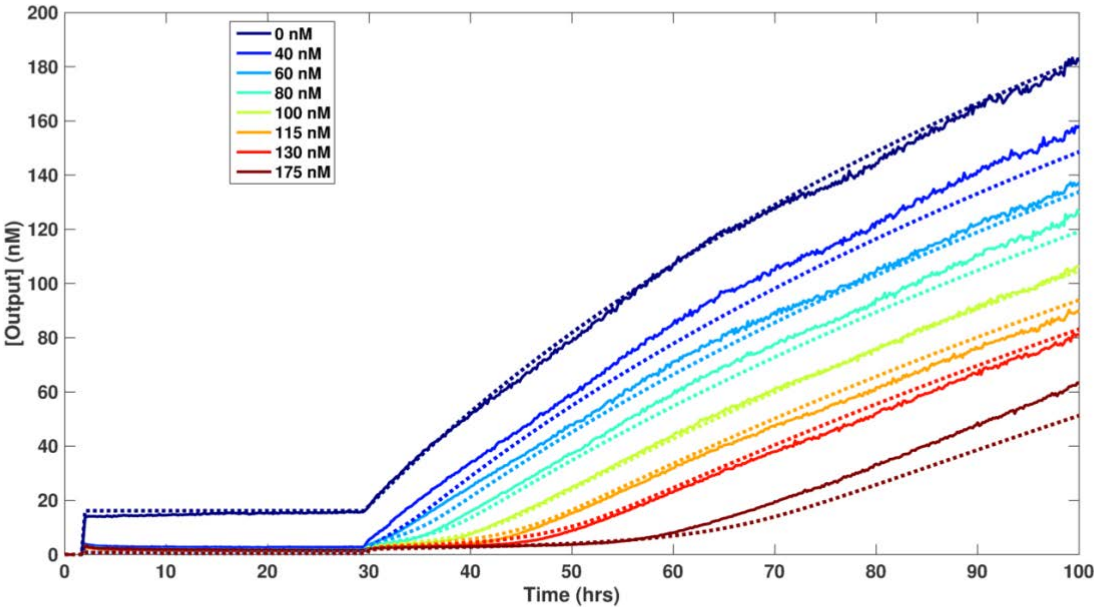

**Figure S2.21 Comparison of data and the model prediction for System 1 using 1 µM S and I. Delay** concentrations are listed in the legend. Reporter-only baseline was initially measured followed by **Source** and **Delay** complex addition at 1 hour. **Initiator** was added after 30 hours. Parameters and reactions included in the model were as described above in Figs. S2.18-S2.20 and in Zhang and Winfree.[36]

## 2.6 ACKNOWLEDGEMENTS

The authors would like to thank Elisa Franco, Deepak Agrawal, Abdul Mohammed and John Zenk for insightful conversations. This work was supported by NSF-CCF-1161941, NSF-SHF-1527377, award SC0010595 from the Department of Energy for some materials and supply costs, and a grant to the Turing Centenary Project by the John Templeton Foundation.

# CHAPTER 3 DNA SEQUENCE-DIRECTED SHAPE CHANGE OF PHOTOPATTERNED HYDROGELS VIA HIGH-DEGREE SWELLING

## SUMMARY

Shape-changing hydrogels that can bend, twist, or actuate in response to external stimuli are critical to soft robots, programmable matter, and smart medicine. Shape change in hydrogels has been induced by global cues, including temperature, light, or pH. Here we demonstrate that specific DNA molecules can induce 100-fold volumetric hydrogel expansion by successive extension of crosslinks. We photopattern up to centimeter-sized gels containing multiple domains that undergo different shape changes in response to different DNA sequences. Experiments and simulations suggest a simple design rule for controlled shape change. Because DNA molecules can be coupled to molecular sensors, amplifiers, and logic circuits, this strategy introduces the possibility of building soft devices that respond to diverse biochemical inputs and autonomously implement chemical control programs.

## 3.1 INTRODUCTION

If one region of a material shrinks or swells in response to a chemical or physical stimulus, the material can change shape to minimize its overall free energy.[18,70–72] The ability to addressably deform different material regions can thus allow a material to take on many shapes. This principle has been used to create metamorphic materials[9] or soft robots[11] in which embedded wires direct local mechanical deformations.[2,9,11] However, wires add bulk and require batteries or tethering. In contrast, chemomechanically responsive materials swell or shrink in response to chemical rather than electrical or pneumatic signals. Chemicals can diffuse over large distances and into small or tortuous spaces, and the huge number of chemicals that can be synthesized offers unprecedented tunability and specificity. Chemomechanical devices require no batteries and can easily be miniaturized and integrated with other devices.

Stimuli such as temperature, light, electromagnetic stimuli, or pH have commonly been used to direct shape change.[18,70–72] These nonspecific stimuli can induce chemical or conformational changes throughout a material, leading to substantial swelling or shrinking. However, this lack of specificity also means that these stimuli cannot produce addressable control comparable to that in wired systems. We sought to determine whether we could build a combinatorial library of biomolecules, such as DNA sequences, where each species would direct the swelling of a specific material domain.

## 3.2 RESULTS & DISCUSSION[*]

We focused on hydrogels, crosslinked networks of polymers in water, where structural changes can cause extensive expansion or contraction of the material as a whole. To study biomolecular actuation, we considered DNA–crosslinked polyacrylamide hydrogels (Figures 3.1A and S3.1).[37] DNA hybridization exchange processes can direct the release of particles[73] or melt, form, or stiffen these gels.[39,74,75] Hybridization exchange can also induce size or shape changes of DNA-linked nanostructures,[76] thin films,[77] and colloidal crystals.[78–80] However, although the exchange of a DNA strand can cause DNA–crosslinked gels to swell by 10 to 15%, this amount is typically insufficient to change the shape of macroscale gel architectures (Figure S3.2).[38,81]

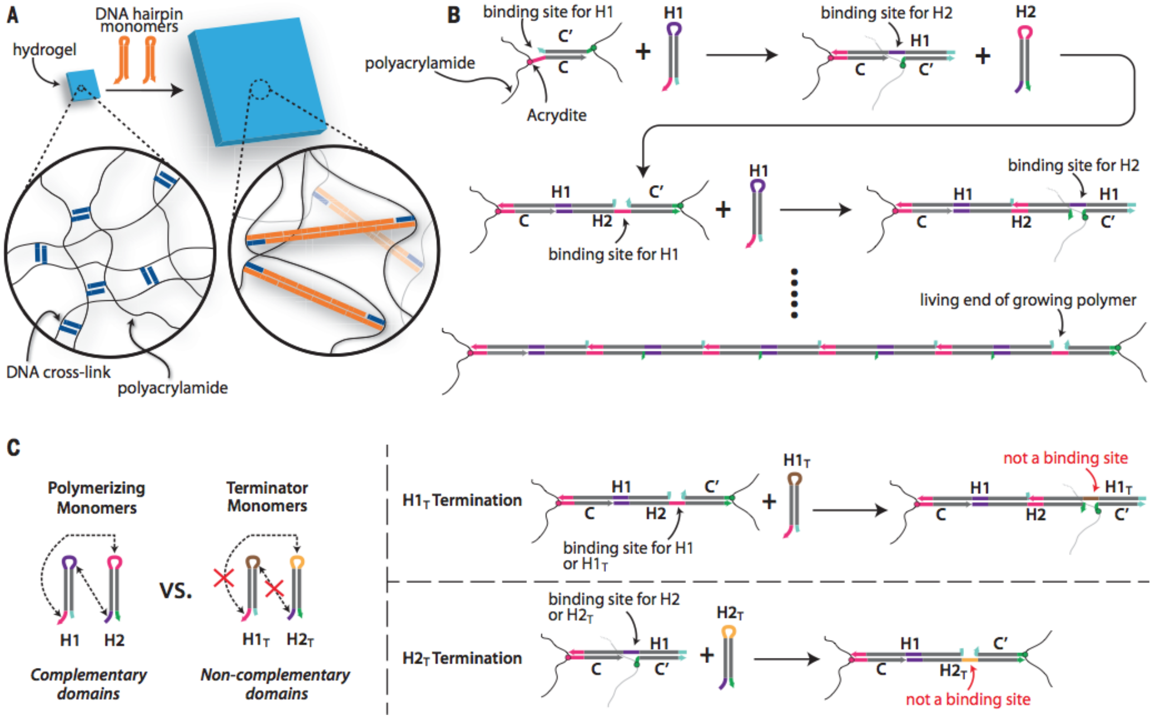

**Figure 3.1 DNA-directed expansion of DNA-crosslinked polyacrylamide gels.** (**A**) DNA–cross-linked polyacrylamide hydrogels (see ref. 42). Hairpins can insert into cross-links, inducing hydrogel expansion. (**B**) Schematic of cross-link C–C′ extension by hairpins H1 and H2. Colors indicate domain type and its complement. Thin black lines indicate polyacrylamide. (**C**) Polymerizing hairpins allow the insertion of additional monomers, whereas terminator hairpin monomers (denoted by "T") leave a site with which no monomers can interact.

---

[*] Throughout this chapter, all supporting figures, tables, and movies are listed in § 3.6 and are denoted with a "S" before the figure/table number (e.g. Figure S3.1 is the first supporting figure of the supporting information section).

Hence, a critical challenge in making DNA-triggered shape-changing hydrogels was to substantially increase the degree of swelling. We postulated that swelling would increase if we lengthened crosslinks successively using a DNA hybridization cascade in which multiple DNA molecules are inserted into a duplex[82,83] (Figure 2.1A and B). To test this theory, we designed DNA sequences (hereafter referred to as "system 1") consisting of hydrogel crosslinks and corresponding hairpins (H1 and H2) for the cascade.

Another challenge to enable addressable control was to reproducibly fabricate well-defined, multimaterial DNA hydrogel shapes capable of arbitrary shape change in three dimensions. We thus developed a photolithography process to pattern DNA hydrogels into precisely defined architectures. Although numerous photolithographic processes for silicon-based devices exist, protocols for photopatterning DNA hydrogels are largely absent, and the patterning process presents distinctive challenges. The moduli of DNA–crosslinked hydrogels are orders of magnitude lower than those of silicon or even many polymers (Figure S3.3); additionally, these hydrogels tend to adhere strongly to untreated glass and photomasks. Further, the ultraviolet light typically used for photopolymerization can damage DNA. We developed a process in which an optimized amount of light exposure drives fabrication to reduce DNA damage. Further, we created a process where structure thickness is controlled by solid spacers sandwiched between glass slides and a CAD-designed chrome mask with coatings and sacrificial layers that enable liftoff (Fig. 3.2A) (see § 3.4 Materials & Methods). Structures with lengths and widths on the millimeter to centimeter scales and thicknesses from 15 to hundreds of micrometers with multiple domains could be patterned serially using mask alignment with registry to underlying layers (see § 3.4). Multiple structures could be fabricated in parallel, and after fabrication, structures were stable in buffer at 4°C for at least 4 months (Fig. S3.4).

We fabricated hydrogel squares (dimensions: 0.06 mm by 1 mm by 1 mm) that contained system 1 cross-links (see § 3.4). In the presence of system 1 hairpins, the hydrogels expanded substantially, whereas the gels in buffer containing an alternate DNA sequence did not expand (Fig. 3.2C and D). Scanning electron micrographs of fixed samples showed that multiscale pores formed during expansion (Fig. 3.2E). Expansion occured unabated at a roughly linear rate (Fig. S3.5 and Movie S3.1).

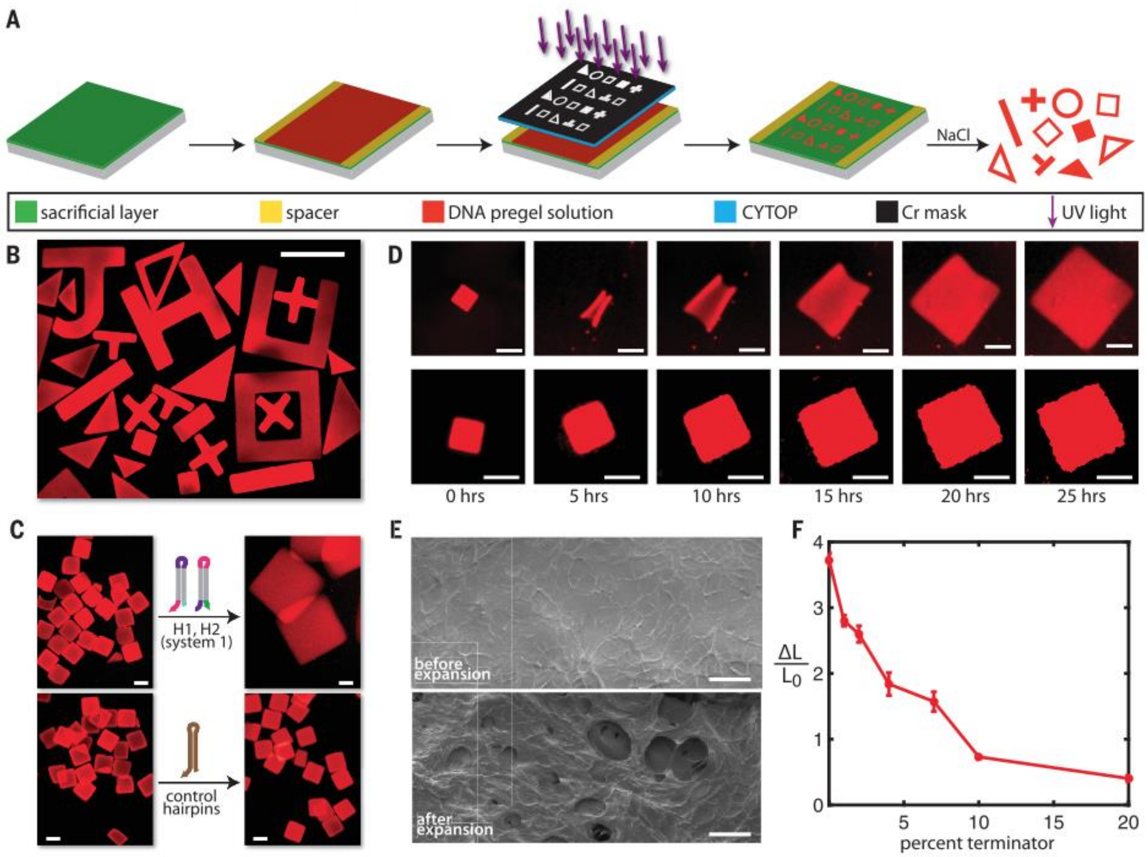

**Figure 3.2 Photopatterning and hydrogel expansion.** (**A**) Photopatterning process flow. (**B**) Fluorescence micrograph of hydrogels poststained with SYBR Green I (see § 3.4). Scale bar, 5 mm. (**C**) Hydrogels expand substantially in 20 mM polymerizing hairpin solution but not in 20 mM control hairpin solution. Scale bars, 1 mm. (**D**) Time-lapse fluorescence micrographs of a hydrogel in polymerizing hairpins (top) and 98% polymerizing, 2% terminating hairpins (bottom). Scale bars, 2 mm. (**E**) Scanning electron micrographs of hydrogels before and after DNA hybridization–driven expansion. Scale bars, 300 mm. (**F**) Linear expansion of hydrogels with different terminator hairpin percentages (N = 4 samples for each data point). Error bars represent 1 SD. $L_0$, initial length; ΔL, change in length.

We thus asked whether hydrogels could reliably expand to a desired final size. We modified the sequences of the polymerizing hairpins to create "terminator hairpins" (Fig. 3.1C). By tuning the relative concentrations of polymerizing and terminator hairpins, we could induce swelling of gels to a well-defined final size (Fig. 3.2F and Fig. S3.5). Inclusion of 2% terminator hairpins produced high-degree but well-controlled swelling and was used in the remainder of our studies (Movie S3.2).

We also found that we could tune the swelling rate. Thinner films swelled slightly faster, but swelling rates do not appear to be limited by the diffusion of DNA hairpins (Fig. S3.6). Increasing the length of one of the toeholds that initiated the hairpin insertion process from three to four or six basepairs sped up expansion more markedly (Fig. S3.7), as did increasing the hairpin concentration (Fig. S3.8). By designing DNA sequences for three more systems of cross-links and hairpins, we could addressably swell multiple

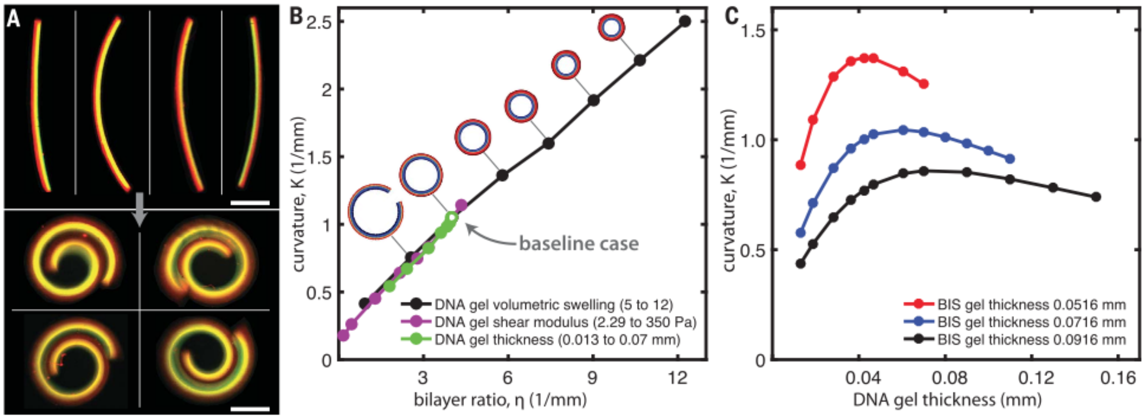

**Figure 3.3 Shape-change mechanics.** (**A**) Fluorescence micrographs of photopatterned hydrogel beams (side views) with a 60-mm-thick BIS–crosslinked polyacrylamide layer (green) and a 60-mm-thick DNA–crosslinked hydrogel (red), before (top) and after (bottom) sequence-driven curving. Scale bars, 1 mm. (**B**) Computational finite element parameter study of bilayer curvature. The baseline case (white circle) corresponds to the experimentally measured bilayer curvature and swelling ratios. The bilayer ratio $\eta$ (Eq. 3.1) captures the effects of the shear moduli, thickness, and volumetric swelling ratios of the gel layers. Illustrated bilayers show the predicted final shapes for different volumetric swelling ratios. (**C**) Analytical predictions of curvature change using the design rule $K = C\eta + K_0$, where $C$ and $K_0$ were fit to the simulation results in (**B**).

domains (Table S3.1). Hydrogels with each cross-link type swelled extensively in response to their corresponding hairpins but not to others (Figs. S3.9 and S3.10). Hairpins also accumulated only in gels with their corresponding crosslink sequences (Fig. S3.11).

To investigate how to design the shape change of composite multidomain architectures, we characterized DNA sequence-driven curling of model bilayer beams (Fig. 3.3A and Fig. S3.12). Although the beams curled only slightly in DNA-free buffer because of different rates of solvent uptake by N,N′-methylenebis(acrylamide) (BIS)–crosslinked and DNA–crosslinked gels (Fig. 3.3A and Fig. S3.13), they curled much more tightly when subsequently exposed to their corresponding hairpins (Fig. 3.3A and Fig. S3.14).

We applied finite element analysis to study bilayer curving caused by DNA-induced swelling (see § 3.5, Finite Element Model of BIS/DNA Bilayer Actuation). The stress response of the gel was assumed to be the sum of an elastic component for the entropic response of the polymer network and the solvent pressure acting on the network derived from the Flory-Huggins theory.[84] We determined the final shape of a structure after DNA-driven swelling by changing the Flory- Huggins parameter in the DNA- and BIS–crosslinked gel layers to achieve the experimentally measured volumetric swelling ratios within the different layers (see § 3.4 Materials & Methods) (Fig. 3.3A) and then solving for the displacement field in the bilayer.

To set the remaining model parameters, we conducted an unconfined compression test and thus measured the Young's modulus of a BIS– crosslinked gel as 2.2 kPa (Fig. S3.15) (see § 3.4 Materials & Methods), which corresponds to a shear modulus of 733 Pa, assuming mechanical incompressibility (see § 3.5). We then used the finite element model to fit the shear modulus (229 Pa) of the DNA gel to obtain the curvature of the bilayer measured in experiments. We found that the effects of varying DNA gel thickness, modulus, and the degree of swelling (Fig. 3.3B) can be described by a simple design rule for the curvature $K = C\eta + K_0$ of the bilayer, where $\eta$ is the bilayer ratio[85] calculated by (see § 3.5.3 Parameter Study)

$$\eta = \frac{AB(1+B)\Delta\theta}{t_{BIS}(1+4AB+6AB^2+4AB^3+A^2B^4)} \tag{3.1}$$

where $A = E_{DNA}/E_{BIS}$ is the ratio of the Young's modulus (in pascals) of the DNA and BIS gels, $B = t_{DNA}/t_{BIS}$ is the ratio of the thickness (in millimeters) of the DNA and BIS gels, and $\Delta\theta$ is the difference in the volumetric swelling ratio between the DNA and BIS gels. The initial curvature $K_0 = 0.2$ mm$^{-1}$ and proportionality constant $C = 0.21$ were obtained from a linear regression of our simulation results (Fig. 3.3B).

This design rule indicates that the curvature is more sensitive to the DNA gel swelling ratio ($\Delta\theta$), with which the curvature varied linearly, than to the shear modulus or thickness of the DNA gel layer. The high degree of swelling was thus essential for extensive shape change. Further, there is an optimum thickness of the DNA gel for which curvature is maximized (Fig. 3.3C). A DNA gel layer that is too thin cannot exert enough force to bend the bilayer, whereas a DNA gel layer that is too thick is negligibly affected by the BIS gel layer and undergoes uniform swelling rather than folding.

The parameter study predicts that the high degree of swelling of the DNA gel could cause millimeter- to centimeter-thick structures to bend. For example, an initially flat 10-mm-long–by–7.23-mm-thick bilayer with optimum DNA gel thickness and a maximum swelling ratio of 3.72 ± 0.11 should fold into a complete circle after sequence-specific DNA- triggered actuation.

We next explored how structures with multiple different DNA sequence–responsive hydrogels could change into different shapes in response to different hairpin inputs. We fabricated flowers in which two groups of petals responded to two different sequences (Fig. S3.16 and Fig.3.4A). In the presence of both sets of sequences, all of the petals folded (Fig. 3.4B). Each set alone caused its corresponding petals to fold, and petals could be folded in sequence through stepwise exposure (Fig. 3.4 C and D). We attribute the twisting of the petals to misalignment errors during photopatterning of the gel layers. We further fabricated hydrogel "crab" devices, in which the antennae, claws, and legs each curled in response to their respective sequences, either all at once or sequentially (Fig. 3.4 E to G, and Fig. S3.17). The structures remained in their actuated states for at least 60 days (Fig. S3.18).

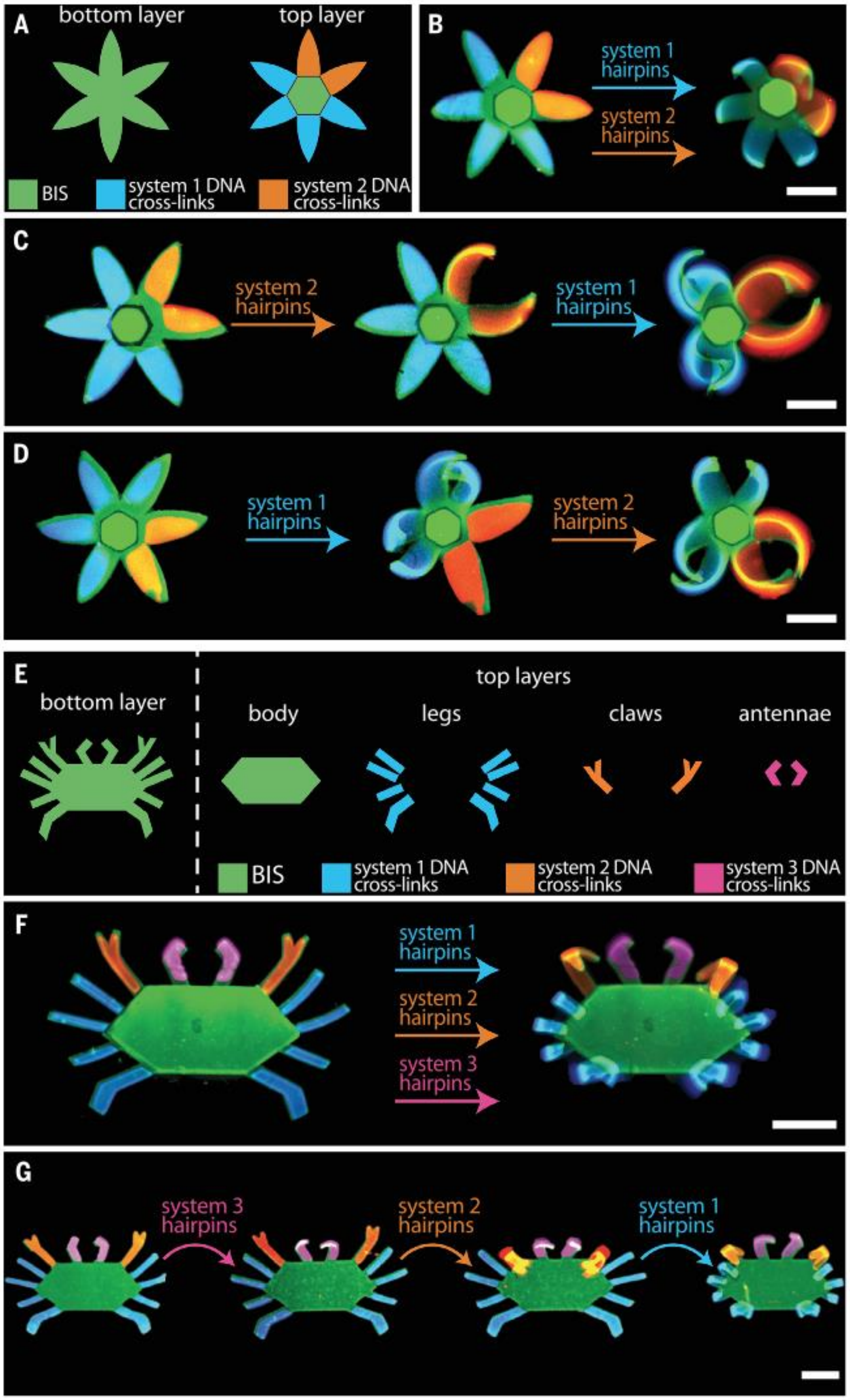

**Figure 3.4 DNA sequence–programmed shape change of macroscopic hydrogel shapes.**(**A**) Schematic of a six-petal flower (§ 3.4). (**B**) All petals curl in response to both system 1 and 2 hairpins. (**C** and **D**) Specific petals actuate in response to system 1 or system 2 hairpins alone. Petals can be actuated in series. (**E**) Hydrogel crab schematic. (**F**) Legs, claws, and antennae all actuate in response to system 1, 2, and 3 hairpins. (**G**) Serial actuation. Solutions contained 20 mM of each hairpin, 98% polymerizing hairpins, and 2% terminating hairpins. DNA–crosslinked hydrogel domains are differentially colored for clarity. Scale bars, 1 mm [(**B**) to (**D**)]; 2 mm [(**F**) and (**G**)].

## 3.3 CONCLUSION

Biological tissues demonstrate the versatility and functionality of shape change driven by biomolecules, where different cues and their concentrations determine which responses occur.[25] We have demonstrated how specific biomolecular signals can also determine which domains of a synthetic material should change in shape and by how much. The DNA oligonucleotide signals used could be the outputs or inputs to molecular sensors[86] and circuits.[23,35] Coupling these circuits to hydrogels could allow materials to exhibit multistage, goal-directed behaviors that are currently impossible to achieve.[72,87,88] Because hairpin insertion and removal can occur while the crosslink remains connected,[82] altering the extension reaction's bias could allow crosslink contraction and, potentially, reversible actuation. Finally, our wafer-scale patterning approach offers the potential for scale-up and integration with existing optical, logic, and memory devices.

## 3.4 MATERIALS & METHODS

### 3.4.1 DNA sequences and sequence design

All oligonucleotide sequences are listed in Table S3.1. The sequences for system 1 crosslinks and polymerizing hairpins, H1 and H2, are based on those used by Venkataraman *et al.*[82] Oligonucleotides were supplied by Integrated DNA Technologies (IDT) in their lyophilized form. Sequences for all terminating hairpins and the sequences for the crosslinks and hairpins in systems 2-4 were designed using the DNAdesign package, available at: www.dna.caltech.edu/DNAdesign/. This program produces sequences with the necessary complementarity to form the desired secondary structures, while minimizing other potential interactions.[89]

### 3.4.2 Preparation of DNA-crosslinked and BIS-crosslinked pregel solutions

Both sets of gels were prepared by UV-initiated, free radical copolymerization of acrylamide along with either N,N'-methylenebis(acrylamide) (BIS) or a DNA duplex as the crosslinker (Fig. S3.1). To enable its copolymerization with acrylamide, the pre-annealed DNA duplex crosslinker contained oligonucleotides modified at the 5' end with an acrydite moiety. For the DNA pregel solution, stock solutions of the crosslink strands C and C' (which contain acrydite modifications), or the crosslink strands for the corresponding system, were first prepared by resuspending lyophilized DNA samples to a final concentration of approximately 25 mM in TAE buffer (40 mM tris-acetate, 1 mM EDTA) that had been previously diluted from 50x stock (Life Technologies, Catalog #24710-030) and supplemented with 12.5 mM magnesium acetate tetrahydrate (Sigma #228648), herein referred to as TAE/$Mg^{2+}$. Oligonucleotide concentrations were verified by absorbance spectroscopy at 260 nm. To prepare the DNA copolymer gel, referred to as poly(Am-*co*-DNA), TAE/$Mg^{2+}$ buffer supplemented with calcium chloride (Sigma #C1016) – herein referred to as TAE/$Mg^{2+}$/$Ca^{2+}$ – and MilliQ water were added to the crosslink strands. The calcium chloride was added to prevent premature dissolution of the poly(acrylic acid) (PAA) sacrificial layer. The DNA crosslinks were then annealed by incubating the solution at 90 °C for five minutes, followed by cooling the solution from 90 °C to 20 °C at 1 °C per minute to allow crosslinks to hybridize. Immediately before photopolymerization, acrylamide (Bio-Rad Catalog #161-0100), Irgacure 2100 (Ciba), and, if applicable, methacryloxyethyl thiocarbamoyl rhodamine B (Polysciences, Inc., catalog #23591) were added to the solution. In cases where the gels were stained with SYBR Green I nucleic acid stain (Invitrogen catalog #S7563), the rhodamine B co-monomer was omitted. The solution was then mixed *via* pipet and degassed under vacuum for 5 minutes to minimize the effect of $O_2$ on radical chain polymerization. The final concentrations of all pregel components are as follows: 1.154 mM of strands C and C’, 1x TAE/$Mg^{2+}$ buffer, 11.1 mM calcium chloride, 1.41 M acrylamide, 3 vol% of Irgacure 2100, and, if applicable, 2.74 mM methacrylated rhodamine B.

The BIS-crosslinked gel solutions were prepared by mixing MilliQ water, TAE/$Mg^{2+}$/$Ca^{2+}$ buffer, 40% (w/v) 19:1 Am:BIS (BioRad Laboratories, Inc., catalog #1610144), 50% (v/v) Irgacure 2100 in 1-butanol, and, if applicable, 50 mM fluorescein-O-methacrylate (Sigma, catalog #568864) into a test tube. The final concentrations of TAE/$Mg^{2+}$ buffer, and calcium chloride are the same as in the poly(Am-*co*-DNA) pregel solution. The final concentrations of the other species are as follows: 5% (w/v) of 19:1 Am:BIS, 1.5% (v/v) Irgacure 2100, and, if applicable, 2.74 mM fluorescein-O-methacrylate. The BIS and acrylamide pregel solution was then mixed and degassed following the same protocol of the DNA pregel solution.

### 3.4.3 Photolithography chamber preparation

The photolithography chambers were prepared according to a previously published protocol.[90] The bottom glass slide served as a substrate onto which the hydrogel samples adhered after photopatterning, while the top slide served as a chromium (Cr) photomask to selectively expose regions of the pregel solution to ultraviolet (UV) light and initiate radical chain polymerization. The top slide of the photolithography chamber was prepared by spin coating SC 1827 (Microposit S1800 Series) on a clean glass slide at 3500 rpm for 3 minutes, followed by baking at 115 °C for 60 seconds. The coated slides were irradiated with a 317 mJ/cm$^2$ dose of 365 nm UV light through film masks designed using AutoCAD and printed by Fineline Imaging. After UV exposure, the glass slides were developed with a 1:10 (w/w) solution of Microposit 351 Developer (Shipley) and DI water, and were dried with $N_2$ gas. Next, a 200 nm layer of Cr was deposited on the glass slide by physical vapor deposition (PVD), after which the slides were consecutively rinsed with acetone and isopropyl alcohol, and were dried under $N_2$ gas to remove the unexposed regions of 1827 positive photoresist. Once prepared, the Cr mask was spin-coated with CYTOP (Type M, Bellex International Corp.) at 4000 rpm and baked at 90 °C for 2 hours to ensure evaporation of the organic solvent. The CYTOP-coated chromium mask prevented the DNA gel from sticking to the mask and allowed for minimal edge roughness.

The bottom slides of the photolithography chamber (Catalog #16004-424, VWR) were prepared by sonicating in 10% (w/w) NaOH for 30 minutes, rinsing with MilliQ water, and drying under $N_2$ gas. The bottom slide was then treated with $O_2$ plasma for 5 minutes to fully oxidize the glass surface. Next, a single layer of polyimide tape (~60 µm thick) was placed along the width of the glass slide to act as a spacer. For thinner hydrogels, aluminum foil (~14 µm thick) was used as a spacer. A roughly 200 nm thick layer of 5% (w/w) PAA crosslinked with calcium was then deposited onto the substrate according to a previously reported protocol.[91] Additional washing (3 min in DI water) and baking steps (5 min at 150 °C) were added to the protocol to remove calcium salt deposits present on the substrate after crosslinking the PAA in a solution of $CaCl_2$. The final photolithography chamber was assembled by clipping the top Cr mask and bottom PAA-covered substrate together with binder clips (Office Depot). The chrome layer of the mask faced inward and came into direct contact with the pregel solution.

### 3.4.4 Photopatterning DNA gel monolayers and DNA/BIS gel bilayers.

To photopattern DNA hydrogel monolayers, the DNA pregel solution was injected via pipet into the photolithography chamber. The chamber was then exposed to 365 nm UV light (Neutronix Quintel aligner) for a total light dose of 240 mJ/cm$^2$ as determined by multiplying the measured UV intensity (Vari-Wave II, 365 nm sensor; Quintel) by the exposure time. The chamber was then gently disassembled and 1 mL of 1 M NaCl was aliquoted onto the substrate to dissolve the PAA sacrificial layer and yield freestanding samples. The monolayers were then placed into a PDMS-coated polystyrene dish to which approximately 2 mL of TAE/$Mg^{2+}$ was added.

To prepare the first hydrogel layer of a bilayer structure, the previous photopatterning protocol was followed using Am-*co*-BIS-*co*-fluorescein pregel solution except that after UV exposure the substrate was washed with approximately 200 µL of TAE/$Mg^{2+}$/$Ca^{2+}$ to remove unreacted pregel solution from the patterned structures. The UV dose for all BIS-crosslinked hydrogel structures is approximately 280 mJ/$cm^2$. The first gel layer was then allowed to dry at room temperature for approximately 20 minutes. The second layer of the hydrogel bilayer structures was fabricated using Am-*co*-DNA-*co*-rhodamine pregel solution. Prior to photopatterning the second gel layer, an additional layer of polyimide tape was placed on the substrate and the second Cr mask was then aligned with the first gel layer using a mask aligner. After satisfactory alignment was achieved, the Am-*co*-DNA-*co*-rhodamine solution was injected via pipet into the photolithography chamber and exposed to UV light for a total dose of 240 mJ/$cm^2$. At this point, when the bilayer bar structures were fabricated, the chamber was gently disassembled and approximately 1 mL of 1 M NaCl was aliquoted onto the substrate to dissolve the sacrificial layer and yield freestanding bilayer bar structures (Fig. S3.12). When the petal or crab bilayer structures were fabricated, the above process of washing the patterned structures, aligning the masks, injecting pregel solution, and exposing to UV light is repeated until the final hydrogel domain is patterned, at which point the photolithography chamber is disassembled and 1 M NaCl was added to yield free-floating hydrogel structures.

### 3.4.5 Quantifying the DNA-driven expansion and shape change of DNA gels.

To measure the rate of expansion and final uniaxial swelling rate of poly(Am-*co*-DNA) hydrogels driven by DNA polymerization, Am-*co*-DNA pregel solution was prepared as previously described, without methacryloxyethyl thiocarbamoyl rhodamine B, and gels were patterned into either 60 µm or 14 µm thick, 1 x 1 mm square shapes using appropriate photomasks. After fabrication, the DNA gels were stained overnight in a solution of 2x SYBR Green I (Invitrogen catalog #S7563) and TAE/$Mg^{2+}$ buffer. The SYBR staining solution was then removed and the samples were washed several times with TAE/$Mg^{2+}$ buffer. After the last wash, 2 mL of fresh TAE/$Mg^{2+}$ was added to the petri dish.

All DNA hairpin monomers were supplied by IDT in their lyophilized form and were resuspended to a final concentration of 2 mM in TAE/$Mg^{2+}$ buffer. All swelling and actuation experiments contained a final hairpin concentration (polymerizing hairpin monomer plus terminator hairpin monomer) of 20 μM. Prior to adding the hairpin solution to the DNA gel samples, the hairpin monomers were snap-cooled in order to remove any aggregates or polymers that may have formed by heating oligonucleotide solutions at 95 °C for at least five minutes, followed by cooling on ice for 2 minutes. Next, the hairpin solution was gently added via syringe so as not to disturb the gel samples. Swelling was recorded via time-lapse fluorescence imaging using a gel imager (Syngene EF2 G:Box) equipped with a blue light transilluminator (Clare Chemical, emission max ~450 nm) and a UV032 filter (Syngene, bandpass 572-630 nm). Images were captured in 20 minute intervals until a steady-state was reached or the gels were no longer visible. The uniaxial swelling ratio of the samples was measured manually in either MATLAB or ImageJ. MATLAB code available upon request.

For DNA-driven expansion of the bilayer structures in hairpin solution (20 μM, 98% polymerizing monomers, 2% terminating monomers), the volumetric swelling ratios of the BIS and DNA gel domains within the bilayer beams were measured using a Nikon AZ100 multi- zoom epifluorescence microscope and Zeiss AxioObserver Yokogawa CSU-X1 spinning disc confocal microscope. The sizes of the domains of the 12 bilayer beams were characterized. Some of the bilayers lain on their sides, which allowed us to image them top-down and others side-on. We measured the contour lengths, widths and thicknesses of the BIS and DNA layers of all the bilayers before and after adding DNA hairpins (20 μM solution composed of 98% polymerizing monomers and 2% terminating monomers) and averaged the values. The average volumetric swelling ratio was calculated by dividing the volume of the gels after and before adding DNA hairpins.

Images of bilayer, flower and crab structures were captured using a Nikon AZ100 multi-zoom epifluorescence microscope equipped with a Nikon DS-Fi1 camera. Fluorescence images of poly(Am-*co*-DNA-*co*-rhodamine) gel samples were captured using a Nikon B-2E/C filter cube (excitation 465-495 nm, bandpass emission filter 515-555 nm), whereas images for poly(Am-*co*- BIS-*co*-fluorescein) samples were captured using a Nikon G-2E/C filter cube (excitation filter 528-553 nm, bandpass emission filter 590-650 nm). Domains with different crosslink sequences (patterned in different sequence steps) were false colored in the fluorescence micrographs in Figure 3.4, and isolated devices are presented on a black background for clarity. MATLAB code available upon request.

### 3.4.6 SEM Imaging of poly(Am-co-DNA) hydrogels.

Two 5 mm x 5 mm hydrogel samples, each 600 µm thick, were fabricated by photopolymerization of pregel solution within a PDMS micromold. The pregel solutions were prepared without methacryloxyethyl thiocarbamoyl rhodamine B as previously described. Prior to photopolymerization the PDMS mold was treated with air plasma for five minutes using a surface corona treater (Electro-Technic Products, model BD-20). The pregel solution was then aliquoted into sample wells of the PDMS mold and exposed to 365 nm UV light (Neutronix Quintel aligner) at an intensity of 7.55 mW/cm$^2$ and dose of 680 mJ/cm$^2$ to ensure complete curing of the pregel solution. The samples were then gently excised from the mold and placed into separate petri dishes containing 2 mL of fresh TAE/Mg$^{2+}$ buffer. The gels were allowed to swell to equilibrium overnight via solvent uptake. To one DNA gel sample was added two 500 µL hairpin solutions, each containing 117.6 µM of the regular hairpin monomer and 2.4 µM of the respective terminator hairpin (e.g., 117.6 µM H1 and 2.4 µM H1T) for a final concentration of 19.6 µM and 0.4 µM of the polymerizing hairpin monomer and terminator monomer, respectively. One milliliter of TAE/Mg$^{+2}$ was added to the other sample as a control. The two samples were left out at room temperature for two weeks, at which point the swelling solution was removed and the gels were frozen in liquid nitrogen for five minutes.[92] The gel samples were then lyophilized for 24 hours to fully remove the swelling solution in preparation for SEM imaging (Labconco, Freezone Benchtop Freeze Dry System, Catalog #7382021).

## 3.5 FINITE ELEMENT MODEL OF BIS/DNA BILAYER ACTUATION

### 3.5.1 Constitutive Model

Various theoretical hydrogel models have been developed in recent years to explain the coupled mechanical and stimuli-responsive swelling behavior of hydrogels and to support the design of active hydrogel structures.[93,94] We previously developed a constitutive theory for thermoresponsive hydrogels and showed that it can accurately predict the equilibrium configuration of pNIPAM gels and composite structures in response to temperature and mechanical stimuli.[90,95,96] In our model, we neglected the kinetics of diffusion and assumed that the hydrogel remained in equilibrium throughout the deformation, which was justified by the short diffusion time permitted by micrometer-scale thickness of the bilayer structures.

For the constitutive model, we first defined a deformation field $\boldsymbol{x} = \varphi(\boldsymbol{X})$, that maps material points $\boldsymbol{X}$ in the initial undeformed dry polymer network configuration to spatial points $\boldsymbol{x}$ in the current deformed hydrogel configuration. The deformation gradient tensor is defined as $\boldsymbol{F} = \partial \boldsymbol{x}/\partial \boldsymbol{X}$ from the initial configuration to the current configuration. To model the stress-free swelling of the gel, the deformation gradient tensor $\boldsymbol{F}$ is further decomposed into a mechanical part, $\boldsymbol{F}_e$, and a swelling part, $\boldsymbol{F}_s$:

$$\boldsymbol{F} = \boldsymbol{F}_e \boldsymbol{F}_s, \qquad \text{(S3.1)}$$

where $\boldsymbol{F}_s = \varphi^{-1/3}\boldsymbol{I}$ and $\varphi$ is the polymer network volume fraction of the hydrogel. The polymer network volume fraction is expressed as $\varphi = 1/(1 + \nu c)$, where $\nu$ is the volume per solvent molecule and $c$ is the number of solvent molecules per polymer network volume. Since the gel is initially swollen, we define the swollen undeformed configuration as the reference configuration, and a deformation gradient $\boldsymbol{f}$ mapping from the stress-free reference configuration to the final swollen deformed configuration:

$$\boldsymbol{f} = \varphi_0^{\frac{1}{3}}\boldsymbol{F} \qquad \text{(S3.2)}$$

where $\varphi_0$ is the polymer network volume fraction in the reference state. The left Cauchy-Green deformation tensor and its first invariant are defined as, $\boldsymbol{b} = \boldsymbol{F}\boldsymbol{F}^T$ and $I_b = \mathrm{tr}(\boldsymbol{b})$. The $\boldsymbol{b}$ tensor can be expressed in terms of its principle values and principle directions as:

$$\boldsymbol{b} = \sum_{i=1}^{3} \boldsymbol{\lambda}_i^2 \mathbf{n}_i \otimes \mathbf{n}_i \qquad \text{(S3.3)}$$

and $\bar{\lambda}_i = \varphi_0^{\frac{1}{3}}\lambda_i$ are the corresponding principal stretches of $\boldsymbol{f}$ tensor. The change of volume from the initial dry configuration to the final configuration is related to the mechanical and swelling component as: $J = \det(\boldsymbol{F}) = \det(\boldsymbol{F}_e)\det(\boldsymbol{F}_s) = J_e\varphi^{-1}$.

We assumed that the free energy density of the hydrogel could be additively decomposed into a mechanical term arising from the stretching of a polymer network and a term describing the mixing energy of the polymer network and solvent system:

$$\Psi = \Psi_{mechanical}(I_b, J_e) + \Psi_{mixing}(\varphi) \qquad \text{(S3.4)}$$

The quasi-incompressible Neo-Hookean model is used to describe the strain energy of the network:[97]

$$\Psi_{mechanical}(I_b, J_e) = \frac{G}{2}(I_b - 3 - 2\log J) + \frac{K}{4}(J_e^2 - 2\log J_e - 1) \qquad \text{(S3.5)}$$

where $G$ and $K$ are the shear modulus and bulk modulus of the polymer network respectively.

The Flory-Huggins model[84] is used to express the free energy of mixing:

$$\Psi_{mixing}(\varphi) = \frac{RT}{\nu\varphi}[(1-\varphi)\log(1-\varphi) + \chi\varphi(1-\varphi)] \qquad \text{(S3.6)}$$

where $R$is the gas constant, and $\chi$ is the Flory-Huggins parameter.

The Cauchy stress tensor is derived from the free energy density as $\boldsymbol{\sigma} = (1/J)(\partial\Psi/\partial\boldsymbol{F})\boldsymbol{F}^T$, and the chemical potential is defined as $\mu = \partial\Psi/\partial c$, where $c$ is the number of solvent molecules per polymer network volume:

$$\sigma = \sum_{i=1}^{3}\left\{\frac{G\varphi_0}{\overline{\lambda_1}\overline{\lambda_2}\overline{\lambda_3}}\left(\varphi_0^{-2/3}\overline{\lambda_i^2} - 1\right) + \frac{K\varphi_0}{2\overline{\lambda_1}\overline{\lambda_2}\overline{\lambda_3}}\left[\left(\frac{\varphi}{\varphi_0}\overline{\lambda_1}\overline{\lambda_2}\overline{\lambda_3}\right)^2 - 1\right]\right\}\mathbf{n}_i \otimes \mathbf{n}_i \qquad \text{(S3.7)}$$

$$\mu = RT[\log(1-\varphi) + \varphi + \chi\varphi^2] - \frac{K\nu\varphi}{2}\left[\left(\frac{\varphi}{\varphi_0}\overline{\lambda_1}\overline{\lambda_2}\overline{\lambda_3}\right)^2 - 1\right] \qquad \text{(S3.8)}$$

The constitutive model was implemented into TAHOE (Sandia National Laboratories) for finite element simulation of hydrogel structures. The shear modulus of the DNA hydrogel was obtained from swelling experiments and finite element analysis of the folding of BIS/DNA hydrogel bilayer beams. For the swelling experiments of BIS/DNA hydrogel bilayer beams, the dimensions in the hydrated state before adding DNA hairpins were $l$=4.925 mm in contour length and $w$=0.528 mm in width. The thicknesses of the DNA and BIS layers were $t_{DNA}$=60.6 µm, $t_{BIS}$=71.6 µm. The initial bilayer curvature in the hydrated state was measured to be 0.2 mm$^{-1}$. DNA hairpins were added to the bilayer bars to induce sequence-driven swelling. The average curvature of swollen bilayer bars under equilibrium was measured to be 1.0 mm$^{-1}$. The dimensions of both layers in equilibrium were also measured and the volumetric swelling ratios of the DNA gel and BIS gel were calculated to be 6.91 and 4.42 respectively. The sequence- induced swelling of the BIS gel was caused by the interpenetration of DNA and BIS gels during the layer-by-layer fabrication process, which was confirmed by confocal imaging.

### 3.5.2 Finite element model of swelling-induced folding of a hydrogel bilayer

For the finite element model of the bilayer beam, the simulation started from the initial hydrated configuration, where the initial curvature of bilayer was 0.2 mm$^{-1}$ as measured in the experiments. The model geometry had the same dimensions as measured for the fully hydrated photopatterned bilayers (Fig. S3.19). The mesh was discretized using trilinear hexahedral elements. The dimensions of the elements were $l_e =$ 61.62 µm in length and $w_e = 52.8$ µm in width, and the thicknesses were $t_e^{DNA} = 15.15$ µm, $t_e^{BIS} = 17.9$

μm for DNA and BIS gel elements, respectively. The displacements at $X = 0$, $Y = 0$ and $Z = 0$ were fixed. The Young's modulus of the BIS gel in the fully hydrated state was measured to be 2.2 kPa from unconfined compression tests (Fig. S3.15). Assuming that the gels were mechanically incompressible resulted in 733 Pa for the shear modulus of the BIS gel. The bulk modulus was set to $K = 1000G$ to enforce mechanical incompressibility of the polymer network. Though the BIS gel exhibited DNA interpenetration, we assumed that the shear modulus of the BIS gel did not change significantly during DNA- driven swelling. It was difficult and expensive to prepare and fully expand a DNA-crosslinked hydrogel via hairpin incorporation (in a 2% terminating hairpin solution) large enough to perform a compression test using our equipment because of the long time required for diffusion of enough DNA hairpins into a very thick gel. Handling expanded hydrogels was also very difficult due to the softening that occurs during DNA-driven swelling. To determine the modulus of DNA gel in the fully swollen state, we therefore applied the finite element model to determine the shear modulus of the DNA gel needed to obtain the curvature measured for the actuated bilayer. The DNA sequence-driven swelling was simulated by varying the Flory-Huggins interaction parameter $\chi$. The Flory-Huggins interaction parameter for each domain in the hydrated and DNA-actuated states were selected so that the free swelling ratio of the gels in the simulation matched the results from swelling experiments of BIS/DNA hydrogel bilayers (Fig. S3.14). The average volumetric swelling ratios measured for 12 specimens were 6.91 and 4.42 for the DNA and BIS layers, respectively. The parameters used in the model are listed in Table S3.2.

The initial polymer network volume fraction $\varphi_0$ was obtained by solving equations S3.7 and S3.8 with the conditions $\boldsymbol{\sigma} = 0$ and $\mu = 0$. For the BIS and DNA gel domains, the Flory-Huggins interaction parameter was continuously decreased from 0.55 to 0.51, and at each value the deformation gradient field $\boldsymbol{f}(\boldsymbol{X})$ and polymer network volume fraction $\varphi(\boldsymbol{X})$ were determined by finite element analysis. We performed the finite element simulations while varying the shear modulus of the DNA gel from 2.29 to 350 Pa, and calculated for each case the equilibrium curvature of the bilayer bar at the equilibrium swelling. The equilibrium curvature of the bilayer was calculated as follows: the deformed positions of the points on the midline of the bilayer inner surface were obtained from the simulation result, and the radius of the best fit circle to the points was obtained using the method of least squares. The curvature was then calculated by taking the inverse of the radius. The calculated curvature of the bilayer was compared to the curvature of the actuated bilayer measured in experiments to determine the equilibrium shear modulus of the DNA gel. A shear modulus of 229 Pa produced the best fit to the experimentally measured bilayer average curvature at steady state.

### 3.5.3 Parameter Study

We applied the model to investigate the effect of the thickness, shear modulus and volumetric swelling ratio of the DNA gel on the curvature of folding BIS/DNA gel bilayer bars. We first varied the DNA gel thickness from 13 μm to 70 μm while keeping the BIS layer thickness of 71.6 μm, DNA gel shear modulus of 229 Pa and volumetric swelling ratio of 6.91 unchanged. Next, we kept the DNA gel thickness and volumetric swelling ratio constant at 60.6 μm and 6.91, respectively, and adjusted the DNA gel shear modulus from 2.29 to 350 Pa. We then kept the DNA gel thickness of 60.6 μm and shear modulus of 229 Pa unchanged while varying the DNA gel volumetric swelling ratio from 5 to 12. These parameters were varied independently, and in each simulation the average equilibrium curvature of actuated BIS/DNA gel bilayer was calculated using the method described in the above section.

Theoretical solutions for the curving of thin film-thick substrate bilayer system have been derived based on the century-old Stoney formula[98] for stresses in the deposited thin film. This formula assumes small strains and rotations, and that the material of each layer is isotropic, homogeneous, and linear elastic. For the case where the thicknesses of each layer are comparable (e.g., $t_{BIS}{\sim}t_{DNA}$), Freund *et al.*[85] derived a modified Stoney formula for the bilayer curvature, which for an initially flat bilayer can be expressed as, $K = 2\eta$. The bilayer ratio, $\eta$, is given by,

$$\eta = \frac{\frac{E_{DNA}}{E_{BIS}}\frac{t_{DNA}}{t_{BIS}^2}(1+\frac{t_{DNA}}{t_{BIS}})\Delta\theta}{1+4\left(\frac{E_{DNA}}{E_{BIS}}\right)\frac{t_{DNA}}{t_{BIS}}+6\left(\frac{E_{DNA}}{E_{BIS}}\right)\left(\frac{t_{DNA}}{t_{BIS}}\right)^2+4\left(\frac{E_{DNA}}{E_{BIS}}\right)\left(\frac{t_{DNA}}{t_{BIS}}\right)^3+\left(\frac{E_{DNA}}{E_{BIS}}\right)^2\left(\frac{t_{DNA}}{t_{BIS}}\right)^4} \tag{S3.9}$$

for the case when the Poisson's ratio is the same in each layer. The $E_{DNA}$ and $E_{BIS}$ are the Young's moduli of the DNA and BIS gels (Pa); $t_{DNA}$ and $t_{BIS}$ are the thicknesses of DNA and BIS gel layers (mm); and $\Delta\theta$ is the difference in the volumetric swelling ratio between the DNA and BIS gels. The modified Stoney formula provided a poor prediction of the simulation results for the curvature of the BIS/DNA gel bilayer, likely because the simulations exhibited large deformation and nonlinear elastic behavior, which violated the assumptions of the theory. However, we found that the simulation results for the curvature change scaled with the bilayer ratio. Plots of the curvature as a function of the bilayer ratio for all cases of the parameter study fell on a straight line of the form $K = C\eta + K_0$ (Fig 3.3B in § 3.2). A linear regression returned $C = 0.21$ for the proportionality constant and $K_0 = 0.2$ mm$^{-1}$ for the initial curvature, which agreed with the average initial curvature of the bilayers measured in the hydrated state (0.21 mm$^{-1}$).

The bilayer ratio $\eta$ depends nonlinearly on the modulus and thickness ratio of the DNA and BIS gels, and depends linearly on the difference in the volumetric swelling ratio. Figure S3.20 shows the variation of the equilibrium bilayer curvature with the DNA gel shear modulus, BIS gel shear modulus, DNA gel thickness and volumetric swelling ratio. Increasing the DNA gel thickness or shear modulus increased the flexural stiffness of the DNA gel resulting in a higher curvature, signifying a more curved bilayer. Likewise, increasing the DNA gel volumetric swelling ratio increased the curvature. As shown in the figure, the curvature was most sensitive to the DNA gel volumetric swelling ratio. Changing the BIS gel shear modulus had a small effect on the final curvature, with a less stiff BIS gel leading to only slightly more folding. In contrast, the shear modulus of the DNA gel had a pronounced effect. When the DNA gel shear modulus was increased from 2.29 to 850 Pa, the equilibrium curvature increased asymptotically until the DNA gel shear modulus reached the BIS gel shear modulus. In Figure 3.3C of the main text we plotted the equilibrium bilayer curvature as a function of the DNA layer thickness, $t_{DNA}$, for BIS layer thicknesses of 51.6 µm, 71.6 µm, and 91.6 µm. Increasing the BIS gel thickness resulted in a lower curvature due to the increased flexural stiffness of BIS layer. However, the effect of varying the thickness of the DNA gel was more complicated. For each BIS gel thickness, there was an optimum thickness of DNA gel for which the bilayer curvature was maximized. For example, the optimal DNA gel thickness was 60.6 µm for a BIS gel thickness of 71.6 µm. The bilayer curvature decreased for larger and smaller values of DNA gel thickness. A DNA gel layer that is too thin did not exert enough force to bend the bilayer, while a DNA gel layer that is too thick was negligibly affected by the BIS gel layer and underwent uniform swelling rather than inducing folding. The optimal thickness increased with the BIS gel thickness. For the BIS gel thicknesses of 51.6 µm, 71.6 µm and 91.6 µm, the optimum DNA gel thicknesses were 42, 60.6 and 69.8 µm, respectively.

The parameter study also showed that the high degree of swelling of the DNA gel should allow millimeter to centimeter sized bilayer structures to achieve a large shape change. For example, we asked whether a 10 mm long flat bilayer beam that was also several millimeters thick (as opposed to 0.1 mm or less as we had studied previously) could fold into a complete circle. The relation obtained from the parameter study was $K = 0.21\eta + 0.2$, where 0.2 $\mathrm{mm}^{-1}$ represents the initial curvature of the bilayers in the hydrated state. Using the relation $K = 0.21\eta$ and assuming the 10 mm long bilayer beam was initially flat, we determined that the 10 mm long bilayer with the optimum DNA gel thickness can be as thick as 7.23 mm and still fold into a complete circle for the maximum experimentally measured swelling ratio of 3.72 ± 0.11.

## 3.6 SUPPORTING INFORMATION (SI)

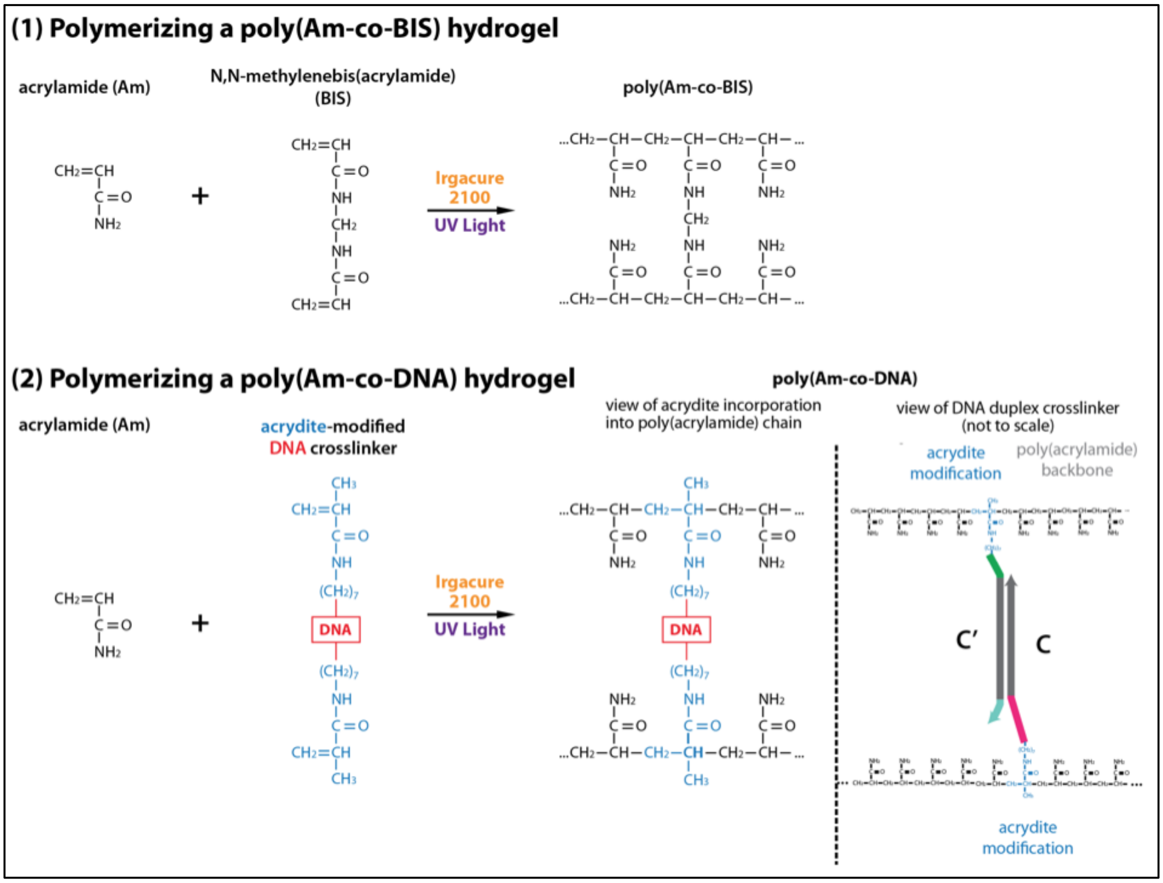

**Figure S3.1 Chemistry for synthesizing a poly(Am-co-BIS) or poly(Am-co-DNA) hydrogel.** Both poly(Am-*co*-BIS) and the poly(Am-*co*-DNA) hydrogels were prepared by standard UV-initiated, radical copolymerization chemistry. In the case of poly(Am-*co*-DNA) gels, a pre-annealed DNA duplex –with each strand modified at the 5' end with a standard, commercially available, acrydite moiety – was used as a crosslinker. The acrydite-modified DNA strands were obtained from IDT in their lyophillized form.

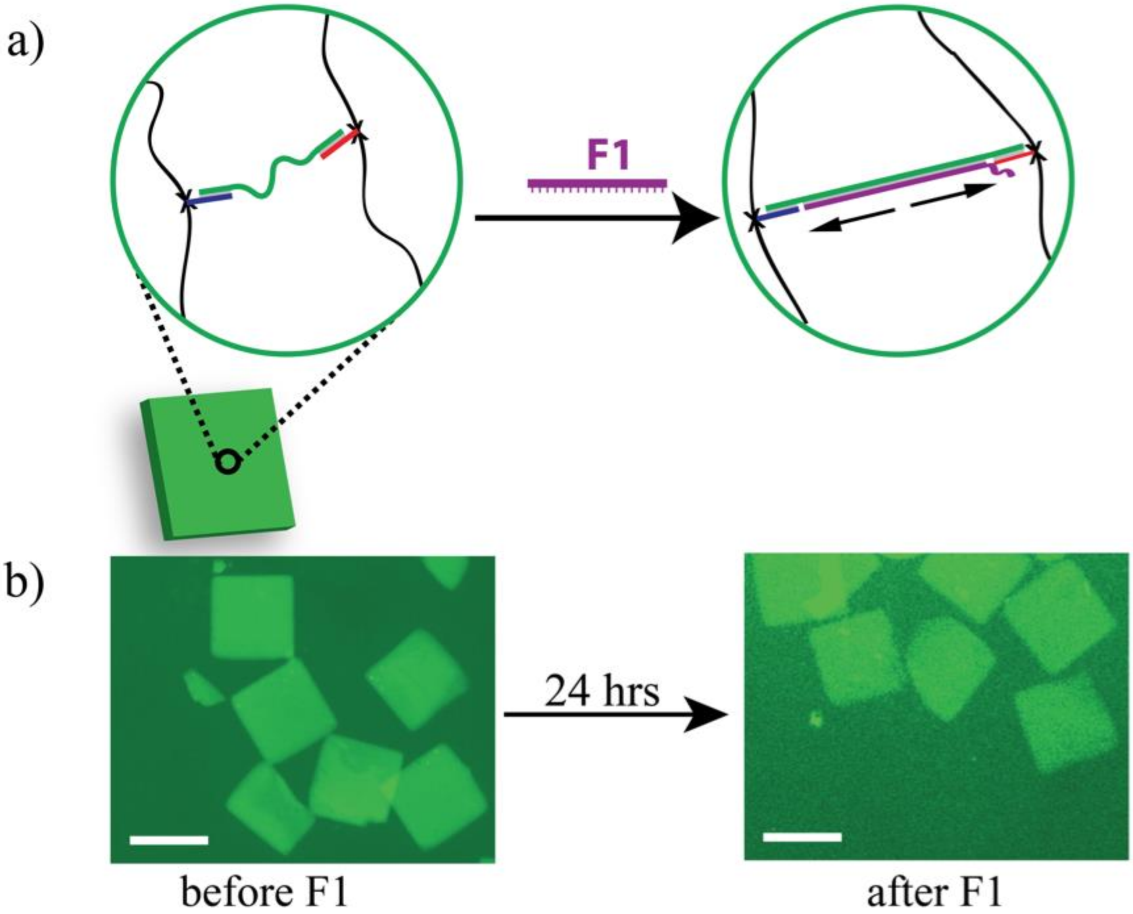

**Figure S3.2 Hydrogel expansion driven by a single- to double-stranded crosslink transition.** (**a**) To quantify the amount of hydrogel expansion that would result from a simple hybridization process within hydrogel crosslinks, we use a 3-strand crosslink architecture studied previously by Lin et al (see reference 45). Hydrogel squares with these crosslinks were fabricated according to the protocol listed in Methods (§ 3.4). The resulting structures swelled to equilibrium due to solvent uptake in TAE/$Mg^{2+}$ buffer, after which the samples were immersed in TAE/$Mg^{2+}$ buffer containing 33.3 μM of F1 DNA strand that is complementary to the single stranded region within the crosslink. (**b**) Representative images of samples before and after treatment with F1. Approximately 24 hours after the addition of F1 strand, the gels had swelled uniaxially by roughly 5%. Brightness and contrast of the images was adjusted using ImageJ. Scale bars are 2 mm.

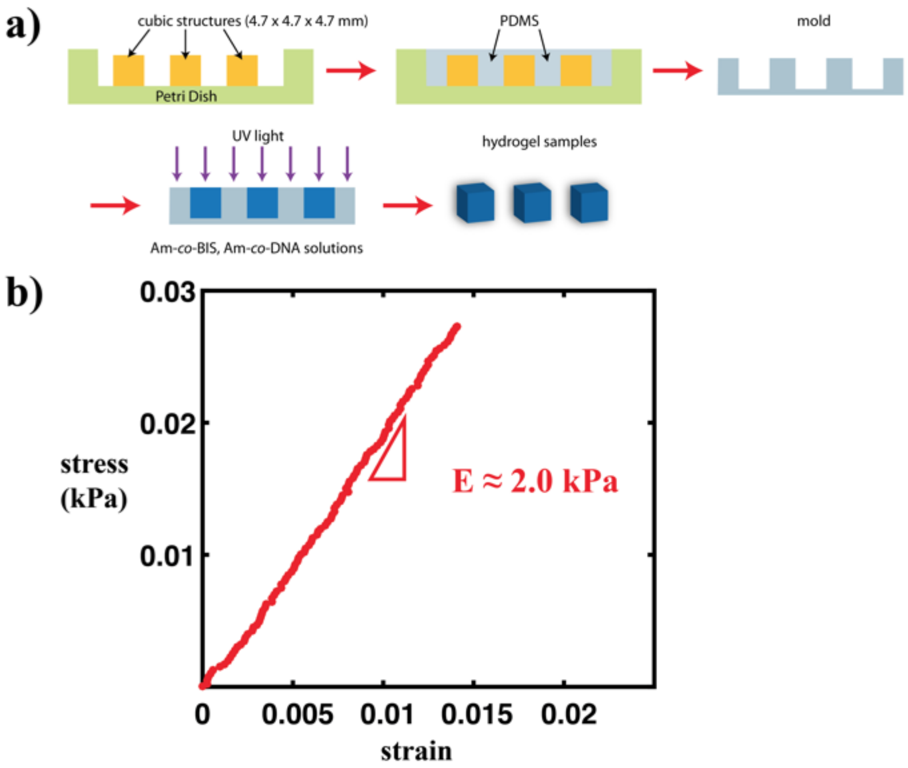

**Figure S3.3 Micromolding and stress-strain measurements of a poly(Am-co-DNA) hydrogel.** To determine the stiffness of the DNA-crosslinked hydrogels used in this study, elastic moduli measurements were obtained for a fully hydrated poly(Am-co-DNA) hydrogel. (**a**) A PDMS micromold was prepared by mixing base and curing components of Sylgard 184 in a 1:10 volume ratio. The resulting solution was poured over a negative pattern, wooden cubes, in a petri dish. The mixture was then heated at 70 °C for one hour and allowed to cool to room temperature. The PDMS mold was then peeled off the negative pattern and taken out of the petri dish. A poly(Am-co-DNA) gel cube sample with dimensions of roughly 4.7 x 4.7 x 4.7 mm was prepared by photopolymerization of a system 1 pregel solution in the PDMS mold. The gel was exposed to 365 nm UV light with an intensity of 7.55 mW/cm$^2$ for five minutes to ensure complete curing of the pregel solution. The gel sample was then placed in 3 mL of fresh TAE/Mg$^{+2}$ buffer and was allowed to swell due to solvent uptake to equilibrium over a period of roughly two weeks, with the buffer being replaced approximately every 3 days. (**b**) The elastic modulus of the DNA gel sample was measured using a controlled force, unconfined compression test at room temperature (Q800 DMA; TA instruments). The applied force on the gel sample was ramped to a maximum static force of 2 mN at a rate of 1 mN/min. Once the maximum static force was reached, the applied force was ramped down to 0 N at the same rate. Static force and displacement data for the loading portion of the compression test were used to generate true stress and true strain curves for the sample. The elastic modulus was measured as the slope of the best-fit line to the stress-strain curve. Previously D. C. Lin *et al.* (*J. Biomech. Eng.* **2004**, *126*, 104-110) reported that the elastic moduli for a poly(Am-co-DNA) gel ranges from 59 Pa to 11.6 KPa depending on crosslink density, consistent with these measurements.

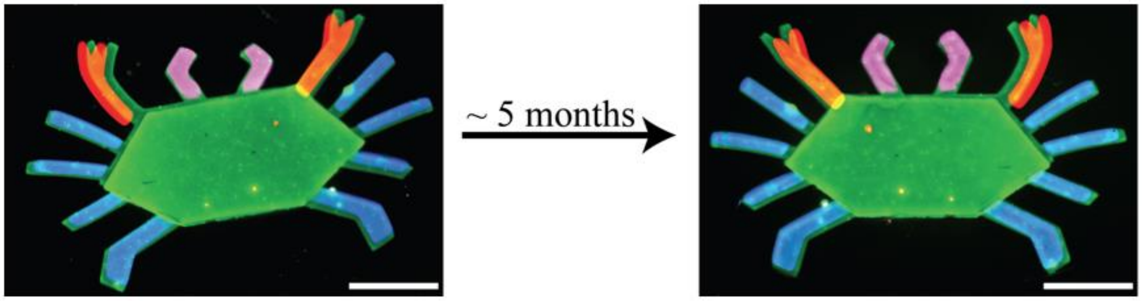

**Figure S3.4 Long-term stability of photopatterned poly(Am-co-DNA) gel architectures.** Poly(Am-co-BIS) /poly(Am-co-DNA) crab architectures were prepared as described in § 3.4 Methods and Fig. S3.17. The micrographs show a typical crab (left) after fabrication and immersion in TAE/$Mg^{2+}$ buffer for 24 hours, and then (right) the same structure after storage at 4 °C in TAE/$Mg^{2+}$ buffer for roughly five months. Prior to imaging the crab after storage, the sample was flipped over in the course of handling. Scale bar is 2 mm.

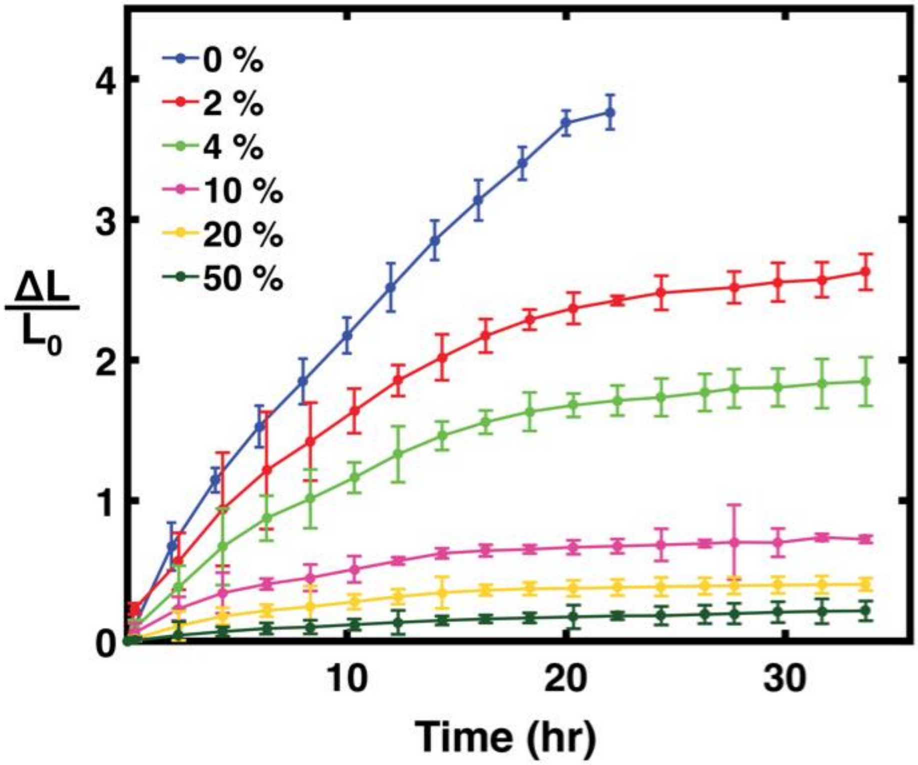

**Figure S3.5 The degree of swelling of poly(Am-co-DNA) gels can be controlled by adjusting the relative percentages of terminator and polymerizing hairpins.** To assess the degree of expansion, poly(Am-co-DNA) gel squares and hairpin solutions with a total hairpin concentration of 20 μM of each of the two hairpin types (e.g. H1, H2) – with the percentages of terminator shown in the legend – were prepared following the protocols listed in the Methods section. Before the gel squares were added to the hairpin solution, they were allowed to take up buffer in a DNA-free solution for 24 hours. This DNA-free solution also contained 2x SYBR Green I nucleic acid stain to enable the gels to be imaged via fluorescence during swelling. For each percentage listed, 4 hydrogel squares were mixed with 3 mL of buffer containing the corresponding hairpin concentrations in a standard petri dish. After the gels were added to the hairpin solutions, images of the gels were captured every 20 minutes in standard gel imager. At each time point, all four sides of each DNA gel sample were measured manually and averaged, then divided by the average lengths of the sides at time zero to obtain a uniaxial swelling measurement, which we denote as $\Delta L/L_0$. For samples that curled during expansion (some of the 0% and 2% terminator samples), the lengths of observable sides were averaged to calculate the degree of uniaxial swelling. Samples were tracked for 36 hours. Data for the 0% sample is not shown after 24 hours because the squares dimmed and their size could no longer be tracked reliably. Error bars represent a single standard deviation about the mean swelling value (N = 4).

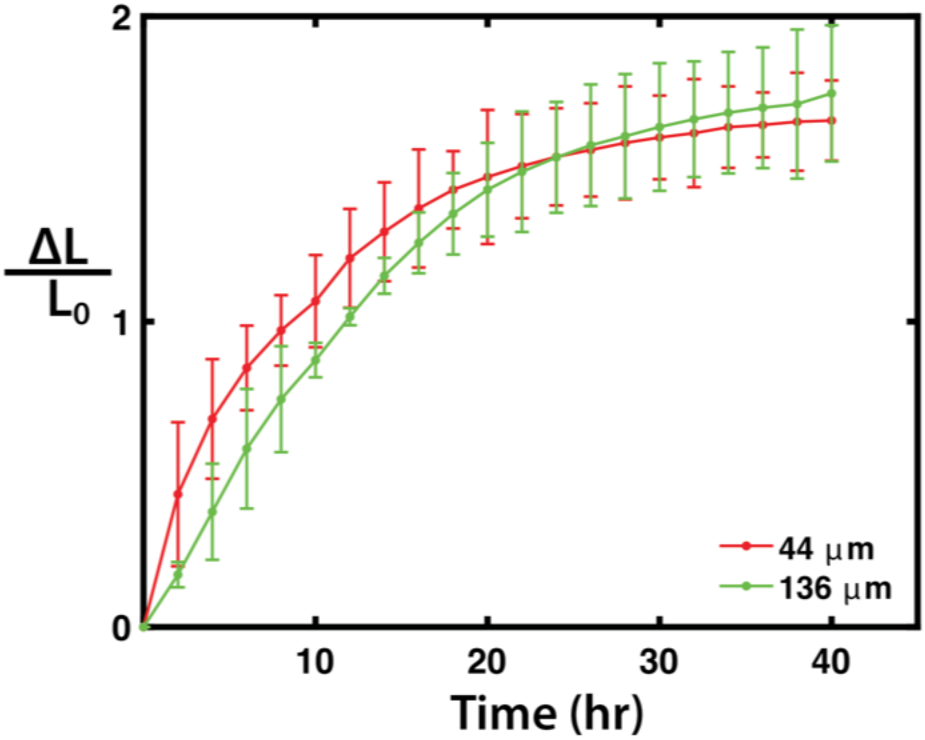

**Figure S3.6 Swelling of poly(Am-co-DNA) films of different thicknesses.** The swelling kinetics of 1x1 mm, system 1 poly(Am-co-DNA) hydrogel squares, with measured thicknesses of 44 μm ± 3 μm and 136 μm ± 2 μm (mean ± SD), in response to system 1 hairpins. The thickness was measured before the addition of hairpins for 4 samples using a confocal microscope as described in Methods. Uniaxial swelling is averaged for at least three samples for each thickness. Error bars represent a single standard deviation about the mean swelling value.

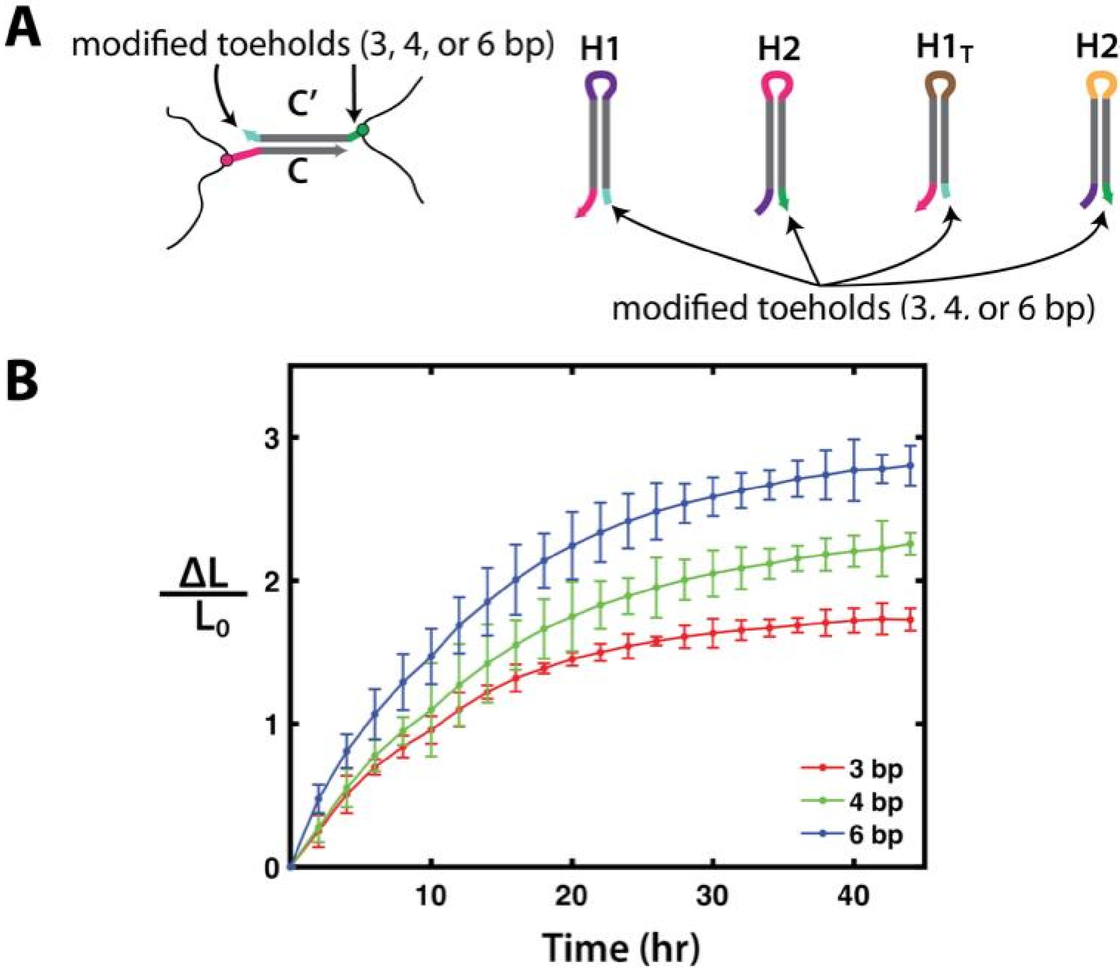

**Figure S3.7 Swelling of poly(Am-co-DNA) films with different hairpin toehold lengths.** (**A**) DNA crosslinker and hairpin systems containing either 3, 4 or 6 base pair toeholds were designed. The altered domains are indicated with arrows. The DNA crosslinker and hairpin system with the 3 bp toeholds are designated in the main text as "system 1." (**B**) The crosslinker complexes were prepared by annealing strand C with a C' strand containing 3 bp, 4 bp, or 6 bp toehold regions according to the protocol outlined in the Methods section. The 1 mm x 1 mm x 60 μm photopatterned poly(Am-*co*-DNA) hydrogel squares were swelled via the addition of a 20 μM, 2% terminator hairpin solution consisting of polymerizing and terminator hairpins with regions complementary to the 3 bp, 4 bp, or 6 bp toehold regions. Uniaxial swelling values are averaged for at least three samples for each toehold length. Error bars represent a single standard deviation about the mean swelling value.

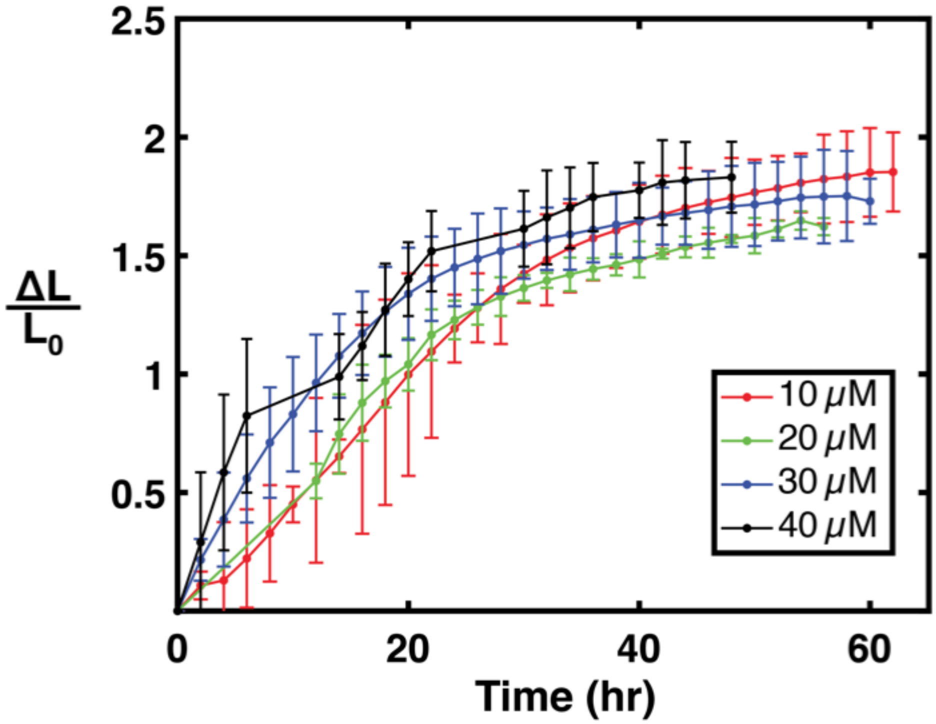

**Figure S3.8 Swelling of poly(Am-co-DNA) films with different total hairpin concentrations.** The swelling kinetics of 1 mm x 1 mm x 14 µm photopatterned poly(Am-co-DNA) hydrogel squares containing system 1 crosslinker. The samples were placed in 3 mL of buffered solution containing 10, 20, 30 or 40 µM of overall hairpins, 2% of which was terminator hairpin monomers. Uniaxial swelling values are averaged for at least 3 samples for each hairpin concentration. Error bars represent a single standard deviation about the mean swelling value.

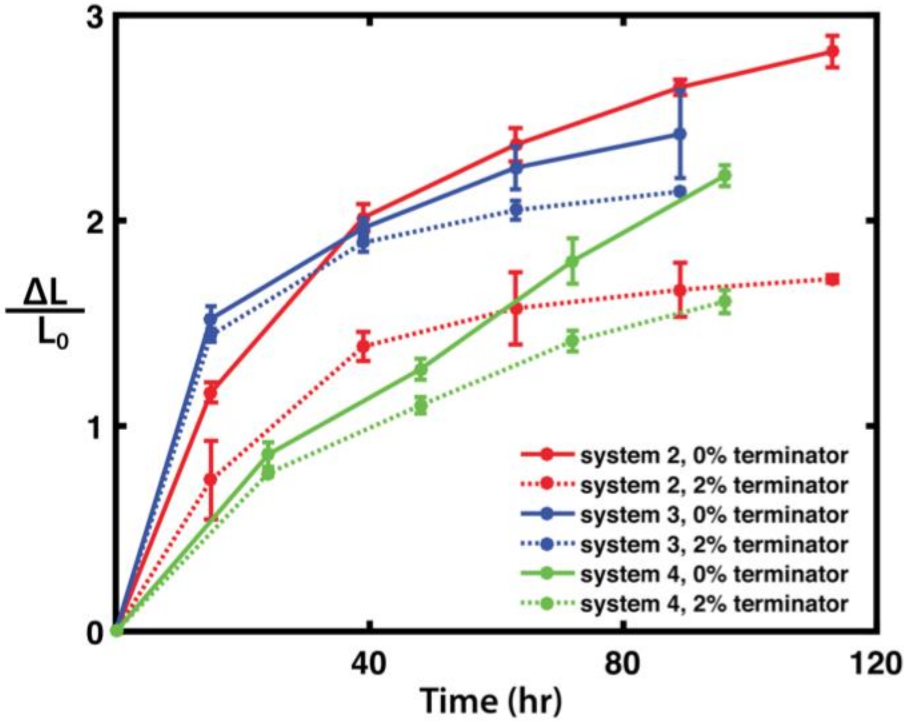

**Figure S3.9 DNA-driven expansion of poly(Am-co-DNA) gels crosslinked by different sequences in response to their respective polymerizing hairpins.** Poly(Am-co-DNA) gel samples were prepared as described in the Methods section with either system 2, system 3 or system 4 crosslink complexes. All gel samples were 1 mm x 1 mm x 60 µm in size. To visualize the gels, samples were stained overnight in 2x SYBR Green I nucleic acid stain and subsequently washed in fresh TAE/$Mg^{2+}$ buffer before being added to a 20 µM hairpin solution containing either 0% or 2% terminator hairpin and were monitored via fluorescence microscopy. Sample dimensions were measured manually using ImageJ software. The error bars show a single standard deviation about the mean swelling value of at least four samples in a particular hairpin solution.

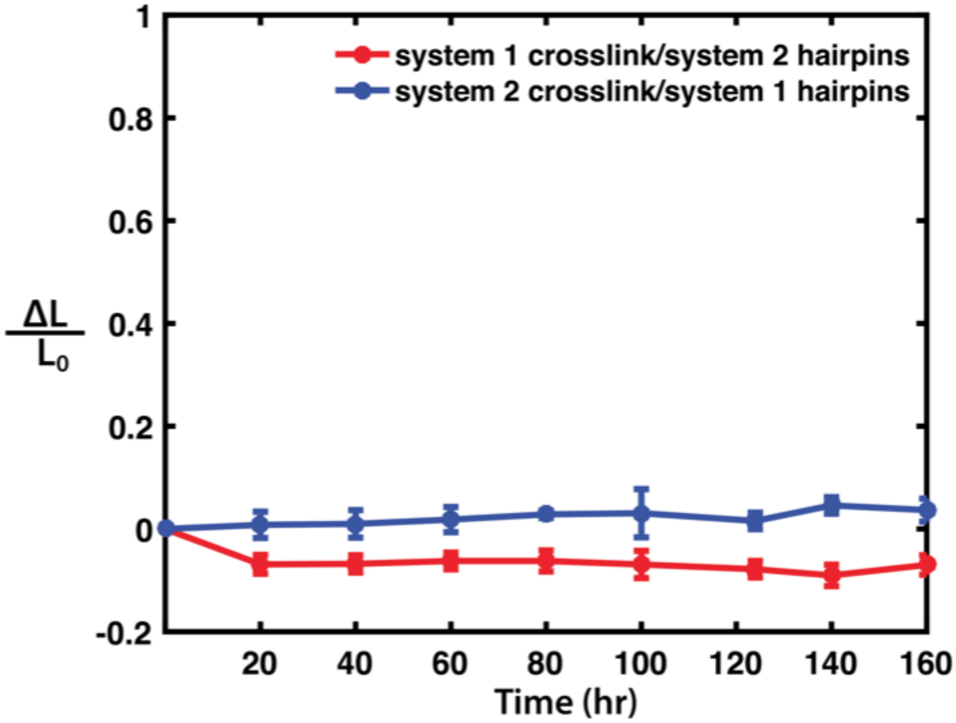

**Figure S3.10 Poly(Am-co-DNA) gels do not expand in solutions of non-complementary hairpin types.** Poly(Am-co-DNA) gels containing either system 1 or system 2 crosslinks were prepared following the protocol listed in the Methods section. The gels were stained overnight in 2x SYBR Green I nucleic acid stain and were subsequently washed in fresh TAE/Mg$^{2+}$ buffer prior to adding the DNA hairpin solution. Four gel samples crosslinked with system 1 DNA complexes were placed in a 20 µM solution of system 2 polymerizing hairpins (with 0% terminator). Conversely, four gel samples crosslinked with system 2 DNA complexes were placed in a 20 µM solution of system 1 polymerizing hairpins (with 0% terminator). The gels were monitored via fluorescence microscopy; sample dimensions were manually measured using ImageJ software. The error bars represent a single standard deviation about the mean swelling value of all the samples exposed to a given hairpin solution.

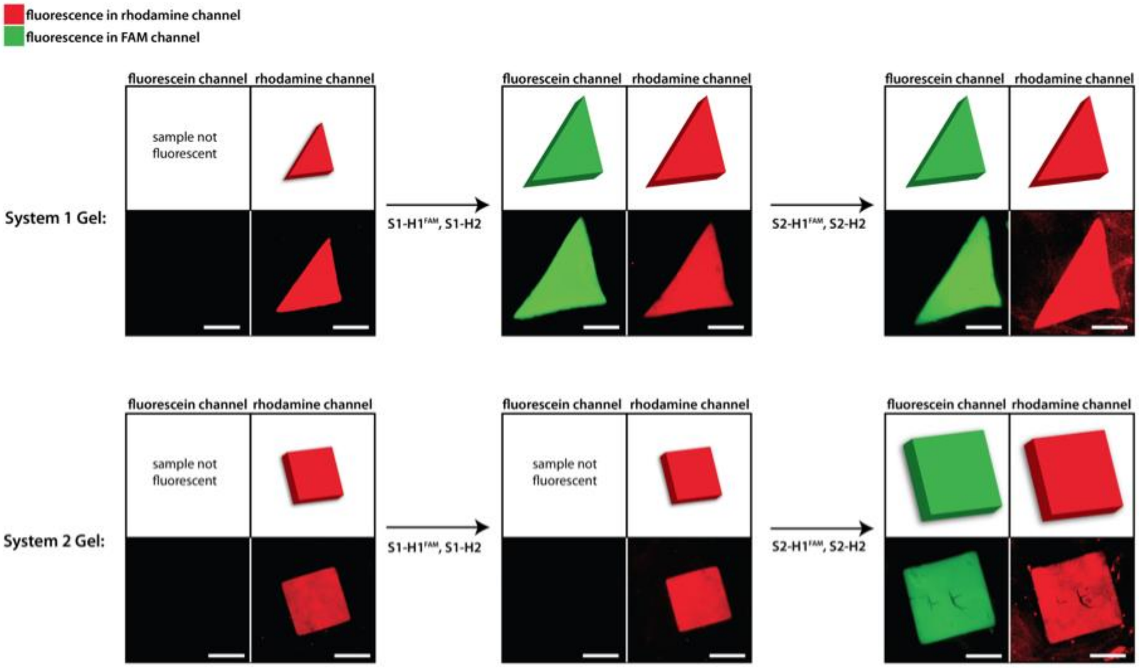

**Figure S3.11 Sequence-specific incorporation of hairpins into poly(Am-co-DNA) gels during expansion.** To verify that DNA hairpins accumulate in poly(Am-co-DNA) gels when expansion occurs but not otherwise, two sets of poly(Am-co-DNA-co-rhodamine) gels – one crosslinked with system 1 and the other crosslinked with system 2 – were each first exposed to a solution of system 1 hairpins, then to a solution of system 2 hairpins. The H1 polymerizing hairpin in each system was labeled on the 5' end with a FAM fluorophore. The system 1 gel was patterned as a triangle, whereas the system 2 gel was patterned as a square so that the type of crosslinks within the gel could be identified by the gel's shape. Before the addition of hairpins, both samples were visible under a Nikon AZ100 epifluorescence microscope using a G-2E/C filter cube (528-533 nm excitation, 590-650 bandpass) because of the rhodamine dye; no significant fluorescence was observed when imaging with the FAM filter. After the addition of 19.6 µM of FAM-labeled system 1 hairpins and 0.4 µM unlabeled system 1 terminator hairpins (i.e. a 2% fraction of the total hairpins, following other experiments), the gel with system 1 crosslinks (the triangle) expanded and was readily visible in the FAM channel, whereas the other shape was not visible. The samples were then transferred to a solution of 19.6 µM of FAM-labeled system 2 hairpins and 0.4 µM unlabeled system 2 terminator hairpins (i.e. a 2% fraction of the total hairpins, following other experiments). In this solution the system 1 crosslinked-gel did not change significantly in size or brightness, but the system 2-crosslinked gel expanded and became visible in the FAM channel. Scale bars are 1 mm.

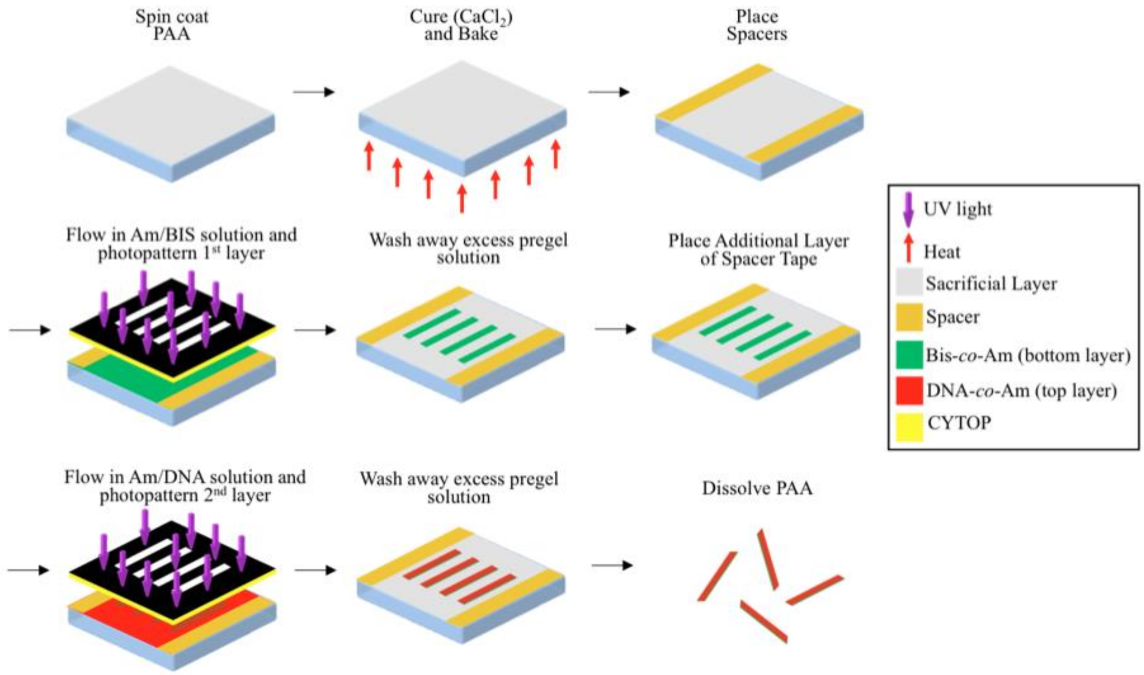

**Figure S3.12 Process Diagram for poly(Am-co-BIS) / poly(Am-co-DNA) Hydrogel Bilayer Fabrication.**Parameters such as bake temperature/time, spacer thickness and solution concentrations are given in the Methods section. After each UV exposure, the resulting samples were washed with TAE/Mg$^{2+}$/Ca$^{2+}$ buffer to remove unpolymerized monomers and DNA crosslinks. The calcium cations in the buffer prevent degradation of the ionic crosslinks of the poly(acrylic acid) sacrificial layer.

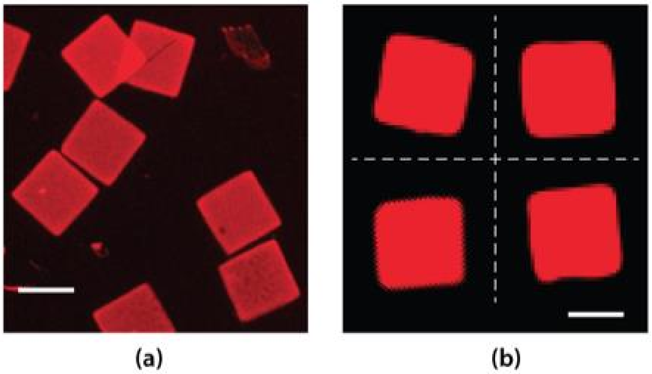

**Figure S3.13 Swelling of poly(Am-co-BIS) and poly(Am-co-DNA) hydrogels after patterning due to solvent uptake.**Both the poly(Am-co-BIS) and poly(Am-co-DNA) gels swell in TAE/$Mg^{2+}$ buffer after photopatterning due to solvent uptake. This solvent uptake controls the initial size of the gels when DNA is added to induce specific actuation. Differential swelling of poly(Am-co-BIS) and poly(Am-co-DNA) gels due to solvent uptake caused the bilayers in Fig. 3.3 to curve slightly before DNA-driven actuation, as seen in Fig. 3.3A. To measure the extent of swelling through solvent uptake for each gel type, poly(Am-co-BIS) and poly(Am-co-DNA) hydrogels were photopatterned as described in Methods. The poly(Am-co-BIS) gels were labeled with rhodamine B via copolymerization with acrylamide and BIS, whereas the poly(Am-co- DNA) gels were stained overnight in 2x SYBR Green dye. The gels were then allowed to equilibrate in TAE/$Mg^{2+}$ buffer for 24 hrs. The poly(Am-co-BIS) gels swelled uniaxially due to solvent uptake by an average of 0.12 ± 0.04 (mean ± SD, N = 5). The poly(Am-co-DNA) gels uniaxially swelled due to solvent uptake by an average of 0.36 ± 0.04 (mean ± SD, N = 4). Images of sample (a) poly(Am-co-BIS) and (b) poly(Am-co-DNA) gels after 24 hours of equilibration in solvent are shown. The degree of swelling was calculated using pattern dimensions of the photomask as the initial lengths of the gel edges. Scale bars are 1 mm.

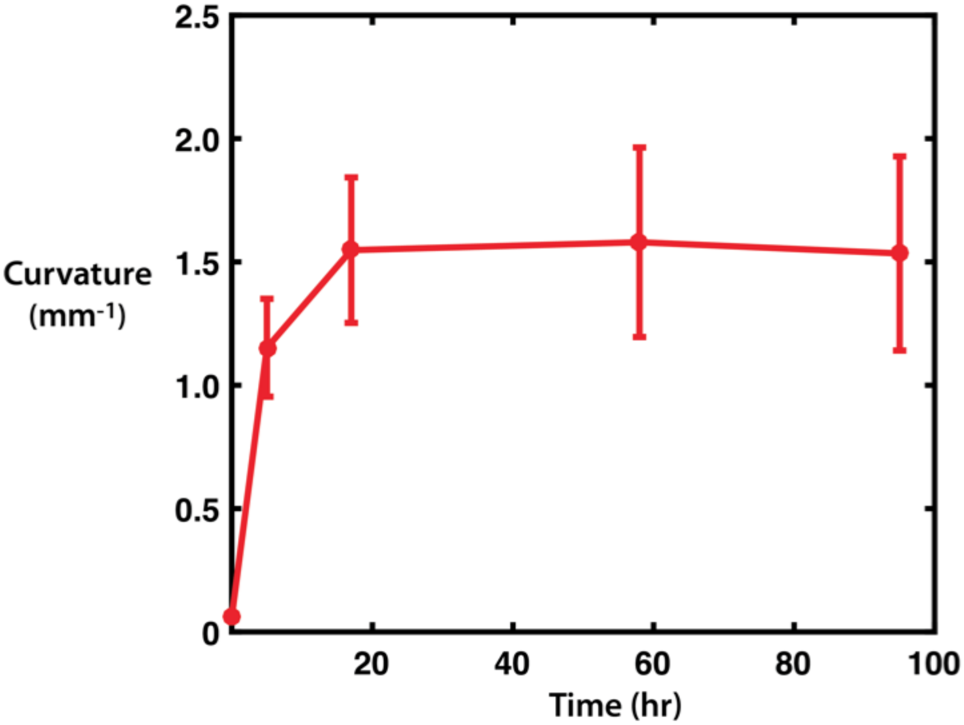

**Figure S3.14 Kinetics of BIS/DNA bilayer actuation.** Gel bilayer architectures comprised of a bottom poly(Am-co-BIS) layer and a top poly(Am-co-DNA) layer were fabricated as described in Methods and Fig. S3.12. After fabrication, the gel structures were allowed to equilibrate in TAE/$Mg^{2+}$ for at least 24 hours. Next, the samples were placed in 3 mL of 20 µM hairpin solution containing 2% terminator hairpin. The curvature of the samples was monitored via fluorescence microscopy and was measured using ImageJ software. Each of the data points represents measurements from 3 samples. Error bars represent a single standard deviation about the mean curvature value.

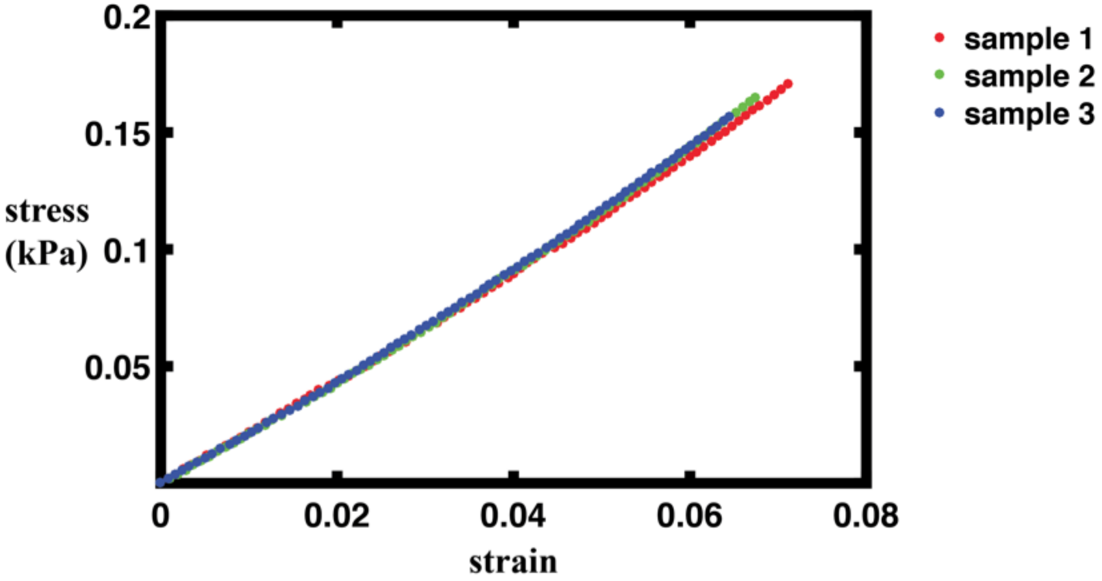

**Figure S3.15 Measurement of the Young's modulus for poly(Am-co-BIS) hydrogels.** Three poly(Am-co-BIS) hydrogel samples, each 8 mm x 8 mm x 8 mm in size, were fabricated via photopolymerization of 5% Am:BIS (19:1) pregel solution in a previously prepared PDMS mold (see Fig. S3.3). The hydrogel samples were then placed in 1x TAE/$Mg^{2+}$ for two days to swell to equilibrium via solvent uptake. To obtain elastic moduli values for the gels, the samples were subjected to an unconfined compression, controlled-force deformation test (Q800 DMA, TA instruments). The applied force was increased at a rate of 0.01 N/min until a maximum static force of 0.015 N was reached, after which the load was reduced at the same rate to 0 N. True stress-strain curves were generated from the raw static force and displacement data. Elastic moduli values were calculated as the tangent to the best fit quadratic curve at 1% strain, and were determined to be 2.24 kPa, 2.18 kPa and 2.17 kPa for samples 1, 2 and 3, respectively. They are on the order of previously determined elastic moduli values for poly(Am-co-BIS) gels prepared with similar concentrations of Am and BIS (see *Curr. Protoc. Cell Biol.* **2010**, Chapter 10, Unit 10.16).

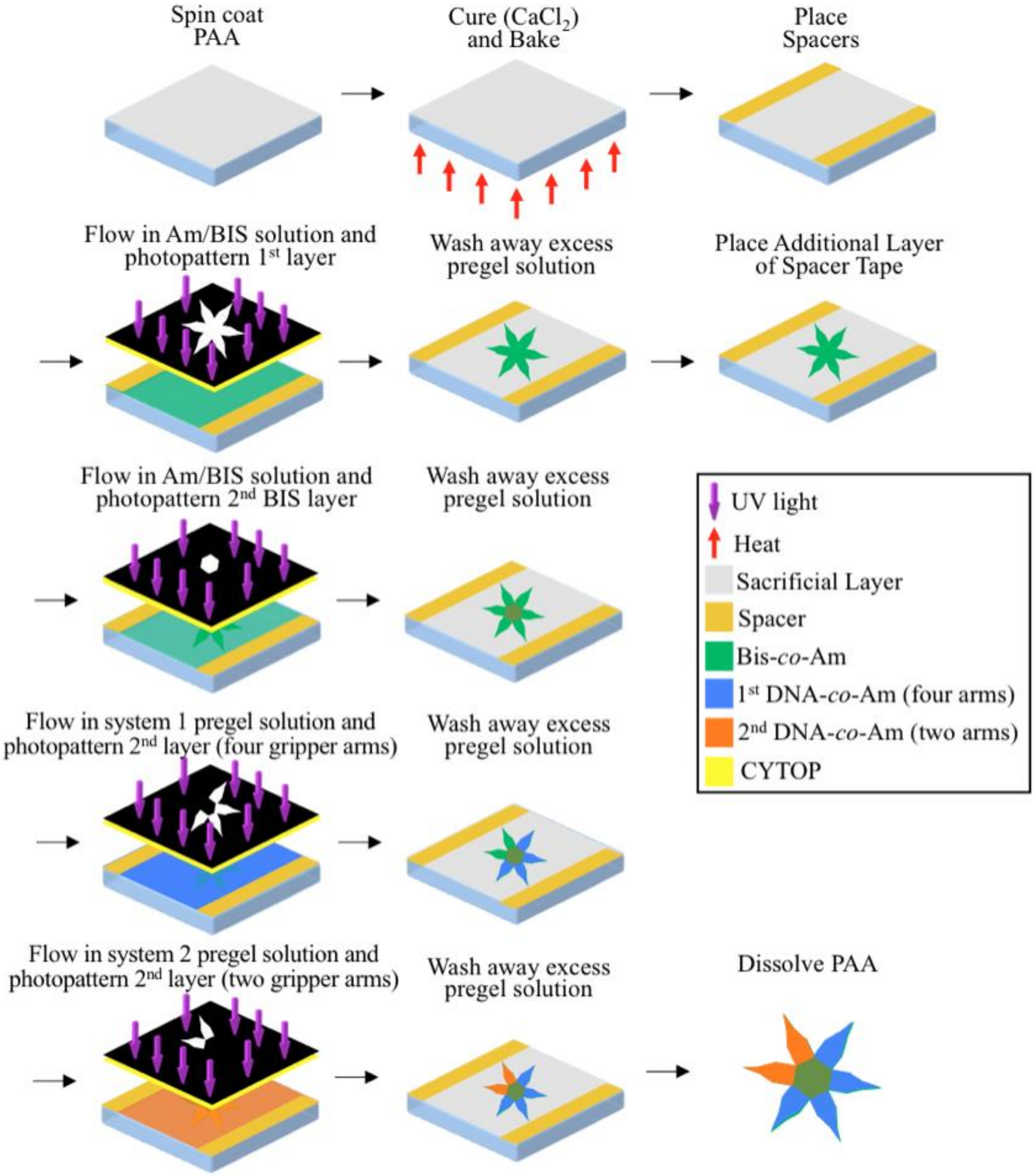

**Figure S3.16 Flower fabrication.** Parameters such as bake temperature/time, spacer thickness and solution concentrations are listed in Methods.

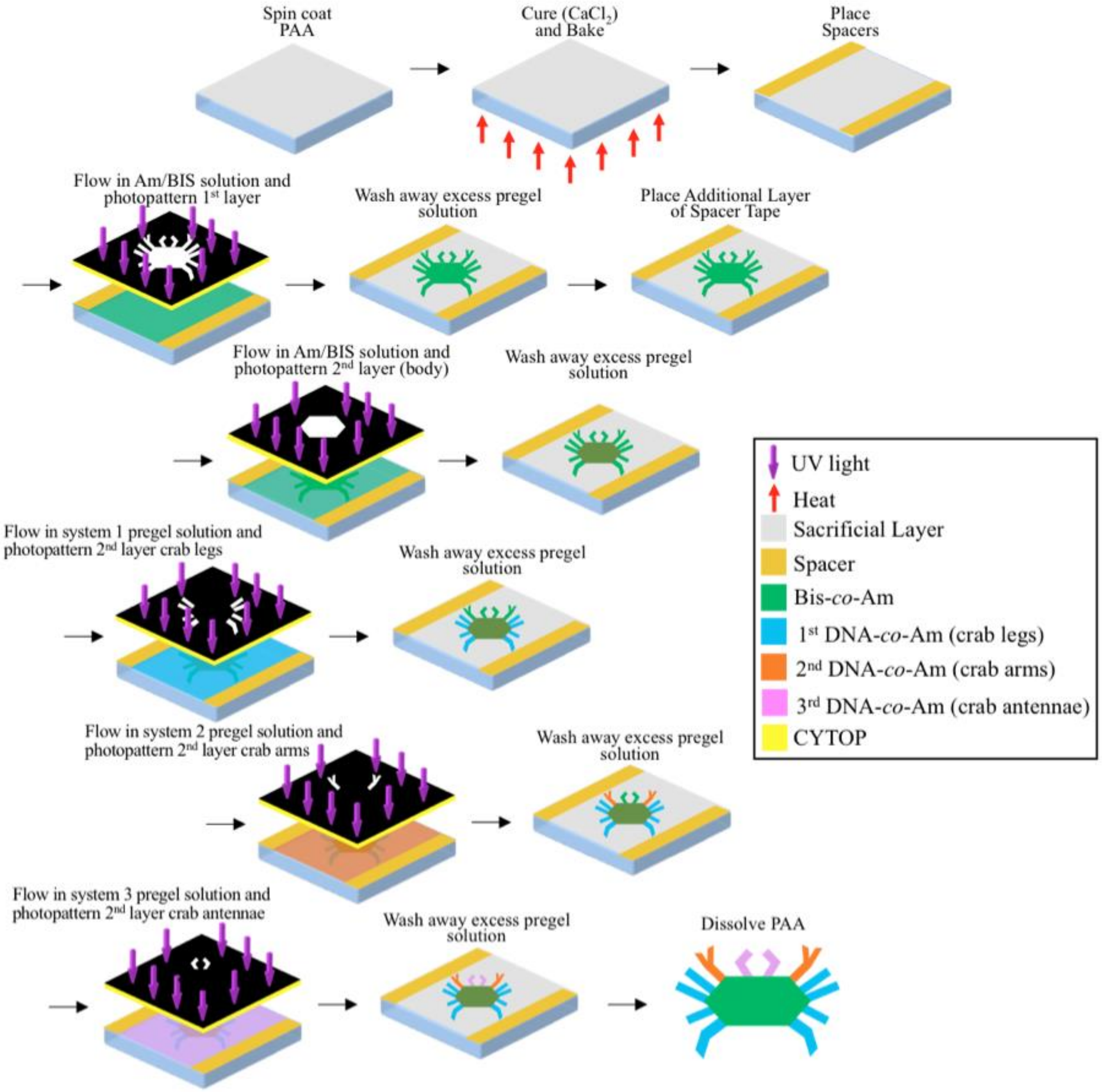

**Figure S3.17 Crab fabrication.** Parameters such as bake temperature/time, spacer thickness and solution concentrations are listed in Methods.

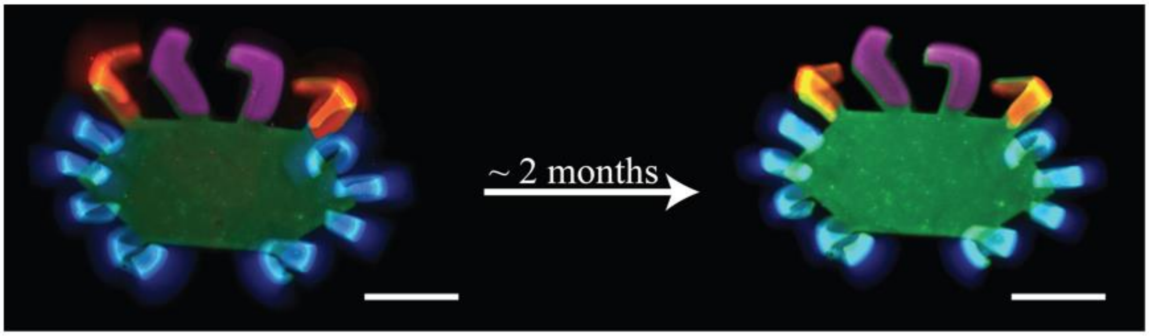

**Figure S3.18 BIS/DNA bilayer crab stability after actuation.** Poly(Am-co-BIS)/poly(Am-co- DNA) crab architectures were prepared according to the protocol described in Methods and Fig. S3.17. Each DNA domain of the bilayers was actuated via treatment with a solution containing 20 µM of the systems 1-3 hairpins, with 2% terminator, for at least 24 hours at room temperature. The actuated crab bilayers then were stored in this same buffer at 4 °C for 2 months. The samples were imaged after the room temperature incubation (left) and after storage at 4 °C for two months (right) via fluorescence microscopy. Scale bars are 2 mm.

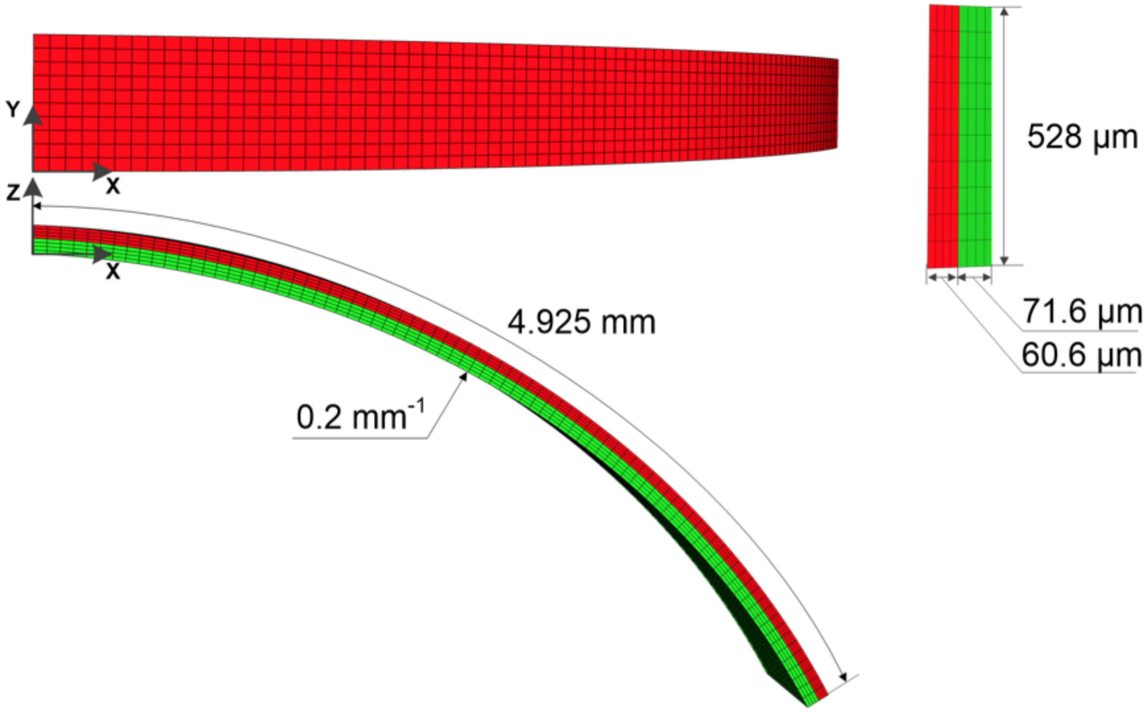

**Figure S3.19 Finite element model of the BIS/DNA hydrogel bilayer.** Green represents poly(Am-co-BIS) hydrogel and red represents poly(Am-co-DNA) hydrogel.

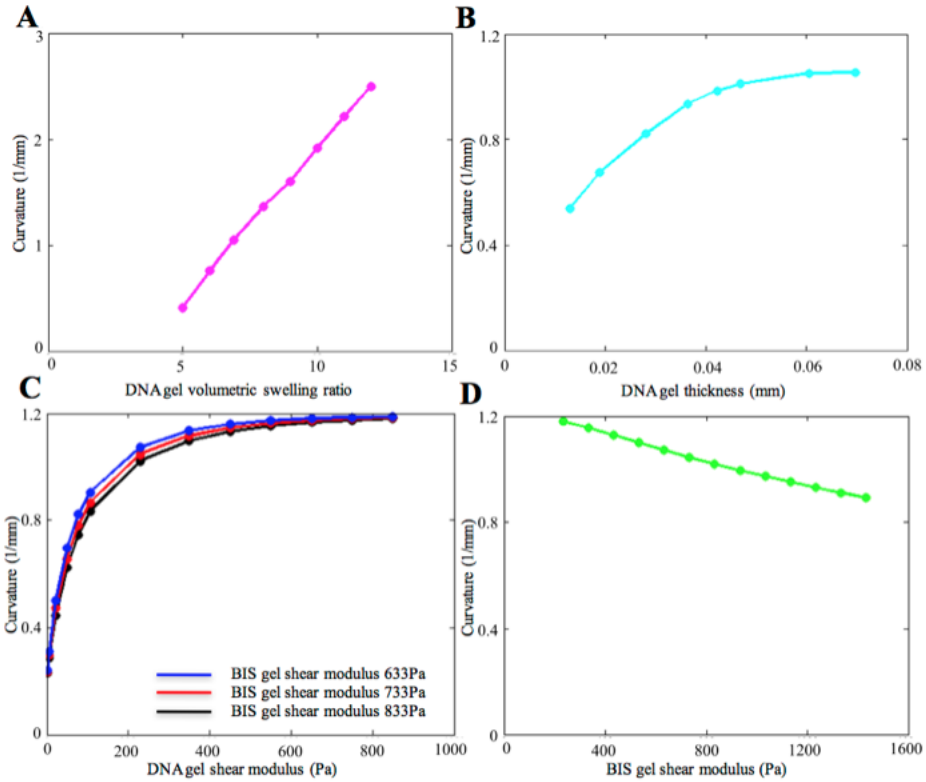

**Figure S3.20 Computational predictions of bilayer curvature as DNA gel swelling ratio, DNA gel thickness, and DNA and BIS gel shear moduli are individually varied.** (**A**) DNA gel volumetric swelling ratio was changed from 5 to 12, while a DNA gel thickness of 60.6 µm, DNA gel shear modulus of 229 Pa, BIS gel thickness of 71.6 µm and BIS gel shear modulus of 733 Pa were kept constant; (**B**) DNA gel thickness was changed from 0.013 to 0.07 mm, while a DNA gel shear modulus of 229 Pa, DNA gel volumetric swelling ratio of 6.91, BIS gel thickness of 71.6 µm and BIS gel shear modulus of 733 Pa were kept constant; (**C**) DNA gel shear modulus was changed from 2.29 to 850 Pa for a BIS gel shear modulus of 633~833 Pa, while a DNA gel thickness of 60.6 µm, DNA gel volumetric swelling ratio of 6.91 and BIS gel thickness of 71.6 µm were kept constant; (**D**) BIS gel shear modulus was changed from 233 to 1433 Pa while a DNA gel shear modulus of 229 Pa, DNA gel thickness of 60.6 µm, DNA gel volumetric swelling ratio of 6.91 and BIS gel thickness of 71.6 µm were kept constant.

**Table S3.1 DNA sequences of crosslinker and hairpin systems.** All sequences were ordered from IDT in their lyophilized form and resuspended with TAE/$Mg^{2+}$. Sequences for acrydite-modified strands are preceded with a /5ACryd/ designation.

**System 1 Strands**

| DNA Strand | Sequence |
|---|---|
| S1-C | /5ACryd/TAAGTTCGCTGTGGCACCTGCACG |
| S1-C’ | /5ACryd/CAACGTGCAGGTGCCACAGCGTGG |
| S1-H1 | CCACGCTGTGGCACCTGCACGCACCCACGTGCAGGTGCCACAGCGAACTTA |
| S1-H2 | TGGGTGCGTGCAGGTGCCACAGCGTAAGTTCGCTGTGGCACCTGCACGTTG |
| S1-H1$_T$ | CCACGCTGTGGCACCTGCACGTAGACTCGTGCAGGTGCCACAGCGAACTTA |
| S1-H2$_T$ | TGGGTGCGTGCAGGTGCCACAGCGGCCTAGCGCTGTGGCACCTGCACGTTG |
| S1-H1_FAM | /56-FAM/CCACGCTGTGGCACCTGCACGCACCCACGTGCAGGTGCCACAGCGAACTTA |
| Control Hairpin | GCTATCTAGCATCGCACGCTCTTTTTGAGCGTGCGATGCTAGATGCGTAC |

**System 2 Strands**

| DNA Strand | Sequence |
|---|---|
| S2-C | /5ACryd/CTGTCTGCCTACCACTCCGTTGCG |
| S2-C’ | /5ACryd/ATTCGCAACGGAGTGGTAGGCTTT |
| S2-H1 | AAAGCCTACCACTCCGTTGCGGAACCTCGCAACGGAGTGGTAGGCAGACAG |
| S2-H2 | AGGTTCCGCAACGGAGTGGTAGGCCTGTCTGCCTACCACTCCGTTGCGTTG |
| S2-H1$_T$ | AAAGCCTACCACTCCGTTGCGTCAAGCCGCAACGGAGTGGTAGGCAGACAG |
| S2-H2$_T$ | AGGTTCCGCAACGGAGTGGTAGGCAATCGTGCCTACCACTCCGTTGCGTTG |
| S2-H1_FAM | /56-FAM/AAAGCCTACCACTCCGTTGCGGAACCTCGCAACGGAGTGGTAGGCAGACAG |

**System 3 Strands**

| DNA Strand | Sequence |
|---|---|
| S3-C | /5ACryd/GGAACTCGGCAGTCGTCCAAGCGA |
| S3-C’ | /5ACryd/ATCTCGCTTGGACGACTGCCGTAT |
| S3-H1 | ATACGGCAGTCGTCCAAGCGATACGGCTCGCTTGGACGACTGCCGAGTTCC |
| S3-H2 | GCCGTATCGCTTGGACGACTGCCGGGAACTCGGCAGTCGTCCAAGCGAGAT |
| S3-H1$_T$ | ATACGGCAGTCGTCCAAGCGACTGAGTTCGCTTGGACGACTGCCGAGTTCC |
| S3-H2$_T$ | GCCGTATCGCTTGGACGACTGCCGCAGATCCGGCAGTCGTCCAAGCGAGAT |

**System 4 Strands**

| DNA Strand | Sequence |
|---|---|
| S4-C | /5ACryd/ATCGGACCAGCACTTCGCCTACGG |
| S4-C’ | /5ACryd/TGACCGTAGGCGAAGTGCTGGATG |
| S4-H1 | CATCCAGCACTTCGCCTACGGCTCTACCCGTAGGCGAAGTGCTGGTCCGAT |
| S4-H2 | GTAGAGCCGTAGGCGAAGTGCTGGATCGGACCAGCACTTCGCCTACGGTCA |
| S4-H1$_T$ | CATCCAGCACTTCGCCTACGGAAGGTGCCGTAGGCGAAGTGCTGGTCCGAT |
| S4-H2$_T$ | GTAGAGCCGTAGGCGAAGTGCTGGTGTATGCCAGCACTTCGCCTACGGTCA |

**System 1: 4 Basepair Toehold**

| DNA Strand | Sequence |
|---|---|
| S1_4bp-C’ | /5ACryd/ACAACGTGCAGGTGCCACAGCGTGGA |
| S1_4bp-H1 | TCCGCGCTGTGGCACCTGCACGCACCCACGTGCAGGTGCCACAGCGAACTTA |
| S1_4bp-H2 | TGGGTGCGTGCAGGTGCCACAGCGTAAGTTCGCTGTGGCACCTGCACGTTGT |
| S1-4bp-H1$_T$ | TCCGCGCTGTGGCACCTGCACGAAACGGCGTGCAGGTGCCACAGCGAACTTA |
| S1-4bp-H2$_T$ | TGGGTGCGTGCAGGTGCCACAGCGCGACAACGCTGTGGCACCTGCACGTTGT |

**System 1: 6 Basepair Toehold**

| DNA Strand | Sequence |
|---|---|
| S1_6bp-C’ | /5ACryd/GTACAACGTGCAGGTGCCACAGCGTGGATC |
| S1_6bp-H1 | GATCCGCGCTGTGGCACCTGCACGCACCCACGTGCAGGTGCCACAGCGAACTTA |
| S1_6bp-H2 | TGGGTGCGTGCAGGTGCCACAGCGTAAGTTCGCTGTGGCACCTGCACGTTGTAC |
| S1-6bp-H1$_T$ | GATCCGCGCTGTGGCACCTGCACGAAACGGCGTGCAGGTGCCACAGCGAACTTA |
| S1-6bp-H2$_T$ | TGGGTGCGTGCAGGTGCCACAGCGGCCTAGCGCTGTGGCACCTGCACGTT |

**3-Strand Crosslink System Strands**

| DNA Strand | Sequence |
|---|---|
| SA1 | ACGGAGGTGTATGCAATGTC |
| SA2 | CATGCTTAGGGACGACTGGA |
| L3 | TCCAGTCGTCCCTAAGCATGTGTTCGACGGTACAAGAAGAGGGTTACGCTAATGAGTGCTGACATTGCATACACCTCCGTA |
| F1 | AGCACTCATTAGCGTAACCCTCTTCTTGTACCGTCGAACAGATAGAGCTG |

**Table S3.2 Parameters determined for DNA and BIS hydrogels.**

| Parameters | *G* (Pa) | $^{c}$ for the hydrated state | $^{c}$ for the DNA-actuated state |
|---|---|---|---|
| DNA gel | 229 | 0.55 | 0.51 |
| BIS gel | 733 | 0.55 | 0.51 |

**Movie S3.1 DNA-hairpin driven expansion of a poly(Am-*co*-DNA) gel in a solution of 20 µM polymerizing hairpins.** Time lapse fluorescence video of a 1 mm x 1 mm x 60 µm, SYBR Green-stained poly(Am-*co*-DNA) gel over 44 hours. The video is shown 8,300x faster than real time. The gel sample was visualized using a Syngene gel imager and blue light transilluminator (see Methods). Individual frames were subjected to histogram clipping and contrast stretching in MATLAB.

**Movie S3.2 DNA-driven expansion of a poly(Am-co-DNA) gel in a solution of 98% polymerizing hairpin and 2% terminator hairpins.** Total hairpin concentration is 20 µM. Time lapse video of a SYBR Green-stained, 1 mm x 1 mm x 14 µm poly(Am-co-DNA) gel showing expansion to well-defined final size when exposed to a solution of polymerizing and terminator hairpin. The video is shown 8,600x faster than real time. The gel sample was visualized using a Syngene gel imager and blue light transilluminator (see Methods). Individual frames were subjected to histogram clipping and contrast stretching in MATLAB.

## 3.7 ACKNOWLEDGEMENTS

We thank D. Scalise, J. Fern, J. Zenk, H. R. Kwag, A. M. Mohammed, D. Wirtz, and M. McCaffrey for discussions and technical assistance. We acknowledge funding from U.S. Army Research Office award W911NF-15-1-0490 and U.S. Department of Energy award 221874 for some materials characterization.

# CHAPTER 4 ADDITIONAL CROSSLINKER SCHEMES, SWELLING RESULTS, AND SACRIFICIAL LAYER PROTOCOLS

## 4.1 INTRODUCTION

Prior to discovering the large degree of expansion enabled by the crosslinker design and DNA insertion mechanism detailed in the previous chapter, numerous other DNA-based crosslinkers and accompanying swelling reactions were attempted. The purpose of this chapter is to succinctly report on the methods and results of these swelling experiments. These previous DNA crosslinker designs were largely taken from previously published work by Lin *et. al.*, although minor modifications were made in an attempt to increase swelling (e.g., addition of a hairpin-loop structure). In addition to DNA-induced hydrogel expansion, alternative approaches to achieving a chemoresponsive sacrificial layer were explored as well. Attempts to use $Ca^{2+}$-crosslinked alginate, or a DNA-crosslinked hydrogel material itself, as a sacrificial element will be briefly discussed.

## 4.2 RESULTS & DISCUSSION

### 4.2.1 Alternative approaches to a chemoresponsive sacrificial layer

Before ultimately settling on a poly(acrylic acid) sacrificial layer protocol that was originally developed by the Whitesides laboratory,[91] the suitability of several other materials as sacrificial layers was explored. The main parameters that determined whether a material was suitable as a sacrificial layer were: (a) whether hydrogel structures could be reliably photopatterned on top of the sacrificial layer (which, in turn, presumably relies on homogeneity and surface roughness of the layer), (b) whether the layer can selectively dissolve in the presence of specific chemical triggers, and (c) whether any of the components of the sacrificial layer or dissolving agents will destabilize poly(Am-co-DNA) gels.

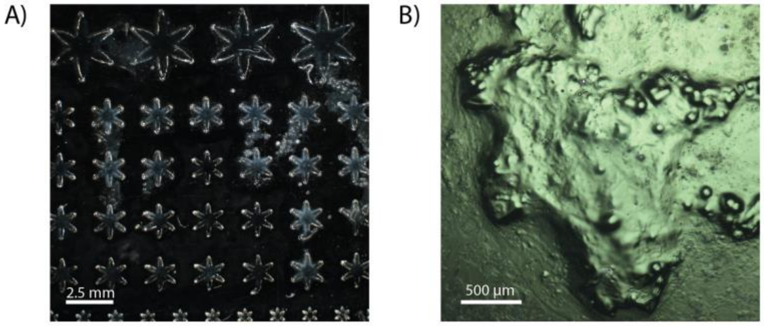

**Figure 4.1 Fabrication of gels on a $Ca^{2+}$-crosslinked alginate sacrificial layer.** (**A**) Fabrication of star-shaped 5% (wt/wt) poly(Am-co-BIS) hydrogel structures on a sacrificial layer of calcium-crosslinked alginate. (**B**) Attempted fabrication of star-shaped poly(Am-co-BIS) hydrogel structures on a similarly-produced sacrificial layer of alginate. It was estimated that the thickness of the alginate layer was approximately 10 microns.

The first material that was explored as a possible sacrificial layer was $Ca^{2+}$-crosslinked sodium alginic acid, herein referred to as alginate. While previously used as a sacrificial element for the capture of cells[99] and fabrication of 3D hydrogel structures,[100,101] it had not been employed in the photolithographic production of hydrogel structures. The chemically selective fabrication and dissolution of the alginate sacrificial layer is due to the reversible, ionic nature of its crosslinking: alginate strands are ionically crosslinked in the presence of divalent cations, while ionic crosslinks are disrupted in the presence of monovalent cations or chelators. The monovalent cations simply replace divalent cations as coordinate sites for the anionic ligands, whereas a chelator disrupts the ionic crosslink by sequestering the divalent cations themselves. With respect to alginate, calcium cations are often used as the cation of choice, whereas ethlyenediaminetetraacetic acid (EDTA) is often used due to its availability, cost, and well-studied properties.[102]

To test whether alginate was a suitable sacrificial element for our gel fabrication protocol, a roughly 10 micron-thick layer of alginate was deposited onto clean glass slides, which were then treated with aqueous $CaCl_2$ to crosslink the alginate polymer strands. Once crosslinking was complete, the alginate-coated glass slides were then used as substrates for photopatterning poly(Am-co-BIS) and poly(Am-co-DNA) hydrogel structures (see § 4.4 Materials & Methods). While BIS-crosslinked gels were successfully photopatterned onto the alginate sacrificial layer, only roughly 30% of the samples lifted off the substrate when treated with EDTA (Figure 4.1A). Patterning the DNA-crosslinked hydrogels proved more challenging as a well-defined structure was never produced (Figure 4.1B), possibly due the rough profile of the alginate sacrificial layer.

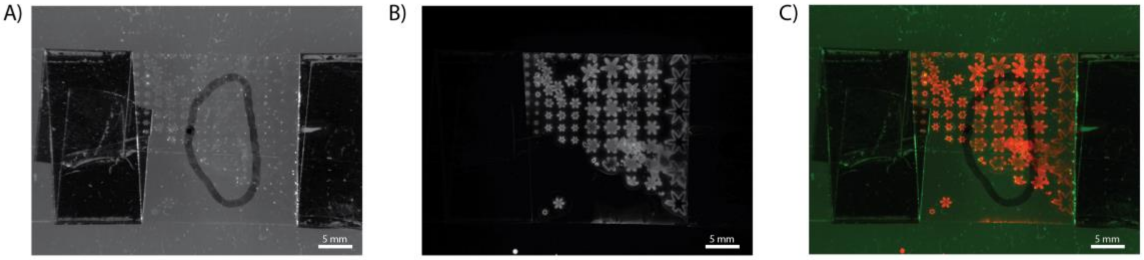

**Figure 4.2 DNA-crosslinked polyacrylamide hydrogel as a sacrificial layer.** (**A**) Brightfied image of a glass substrate partially coated with a DNA-crosslinked polyacrylamide sacrificial layer. The black marker outlines the approximate area covered by the DNA copolymer gel layer. This was visually confirmed immediately after polymerization of the sacrificial layer. Poly(Am-co-BIS) gels are faintly apparent on top of the sacrificial layer and substrate. (**B**) Upon staining with 100x SYBR Gold, it appeared that the DNA sacrificial layer disintegrated either upon photopatterning of the poly(Am-co-BIS) hydrogels or subsequent washing. (**C**) Multichannel, RGB image comprised of the grayscale images given in (**A**) and (**B**). Image (**A**) populates the green channel, whereas image (**B**) populates the red channel.

Due to the difficulty of patterning DNA-crosslinked hydrogels, alginate was abandoned as a prospective sacrificial layer.

In addition to alginate, DNA-crosslinked polyacrylamide hydrogels themselves were tested as a potential sacrificial layer. Owing to the large sequence space inherent in DNA-based reactions, a large number of orthogonal DNA crosslinking sets – where each set is comprised of DNA strands that form the crosslinking complex as well as the accompanying release strands that disrupt it – could be designed such that each set is unreactive towards any other set. This made DNA-crosslinked hydrogels a potential candidate to serve as a sacrificial layer since multiple, non-interacting DNA-crosslinked gels could be designed. To test whether a poly(Am-co-DNA) gel could be used as a sacrificial layer, a pre-gel solution consisting of acrylamide monomers, SA3•SA4•L2 crosslinker complex, and Irgacure 2100 photoinitiator was dropcast onto a clean glass slide and photopolymerized with UV light to form a sacrificial DNA hydrogel layer (Fig. 4.2). Onto the sacrificial layer was photopatterned star-shaped poly(Am-co-BIS) hydrogels in an array of different sizes. While the BIS-crosslinked hydrogels were precisely photopatterned – with strong fidelity to the sample dimensions on the chrome mask – from fluorescence imagery it appeared that the poly(Am-co-DNA) sacrificial layer disintegrated upon either photopatterning the BIS-crosslinked gels or subsequent washing with TAE/$Mg^{2+}$ buffer. Despite several additional attempts, the poly(Am-co-DNA) hydrogels sacrificial layer consistently disintegrated after photopatterning gel samples. Poly(Am-co-DNA) hydrogels were therefore abandoned as a potential sacrificial layer. See § 4.4.2 for a description of hydrogel components.

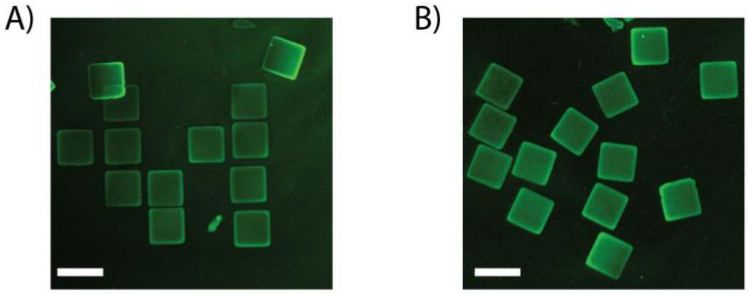

**Figure 4.3 Photopatterning and liftoff of poly(Am-co-DNA) hydrogels on a PAA sacrificial layer.** (**A**) Photopatterned poly(Am-co-DNA) hydrogels (see § 3.4 for a description of hydrogel synthesis). The regular order of the gel samples indicates that are adhered to the PAA sacrificial layer substrate. (**B**) Upon the addition of NaCl, the PAA sacrificial layer dissolves and the samples liftoff from the substrate.

The failure of both DNA-crosslinked polyacrylamide and $Ca^{2+}$-crosslinked alginate sacrificial layers to meet the proposed criteria for a sacrificial layer led to a search for a new base material – one that would dissolve upon exposure to specific reagents compatible with DNA and, in addition, allow for subsequent photopatterning of hydrogel materials. Upon reading the work by Linder *et al.*[91] it became apparent that poly(acrylic acid) (PAA) could meet our criteria: its ion specific gelation and dissolution via $Ca^{2+}/Na^{+}$, respectively, as well as its proven ability to serve as a sacrificial element for subsequent photopatterning of soft materials make it an ideal candidate to employ in the construction of DNA-programmable soft matter devices. As shown in Figure 4.3, PAA was mechanically, and chemically, robust enough to withstand subsequent patterning of DNA-crosslinked gels. See § 3.4 for a description of how to fabricate and dissolve the PAA sacrificial layer.

### 4.2.2 Swelling of poly(Am-co-DNA) gels using alternative crosslinker schemes

Prior to the discovery of roughly 100-fold volumetric swelling of poly(Am-co-DNA) gels via the autonomous polymerization scheme detailed in Venkataraman *et al.*,[82] several other crosslinking motifs were explored to determine whether swelling sufficient for hydrogel-based devices was achievable. The designs for these motifs were largely based on previous studies by given by Lin *et al.*[39,40] Using these DNA crosslinker designs we sought to swell photopatterned poly(Am-co-DNA) hydrogels by either disrupting, lengthening, or stiffening the DNA-based crosslinker complex.

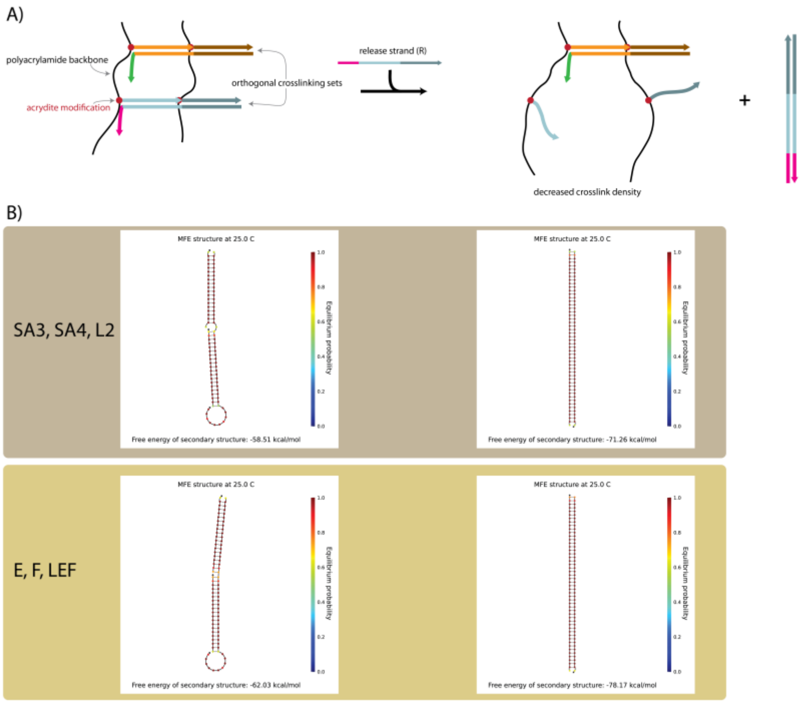

**Figure 4.4 DNA crosslinker design and NUPACK analysis.** (**A**) Schematic of DNA crosslinkers in a polyacrylamide gel. Reverse complementary domains are given the same color. The gel matrix is fabricated with two sets of orthogonal DNA crosslinkers. One of the crosslinker complexes is disrupted upon the addition of its respective release strand. (**B**) Thermodynamic stability, predicted by NUPACK, of each crosslinker complex and the resulting duplex that is formed upon addition of release strand.

To determine the efficacy of each DNA crosslinker, swelling experiments similar to, but not the same as, those detailed in Chapter 3 were performed. Here, each swelling experiment used square gels – roughly 60-70 $m$ thick – that were stained in SYBR Green nucleic acid dye to enable monitoring of lateral gel dimensions via fluorescent imaging (see § 3.4 for protocol). Since it was impossible to track the swelling of individual samples over time (due to equipment constraints), $\Delta L/L_0$ was defined as

$$\frac{\Delta L}{L_0} = \frac{\langle L_i \rangle - \langle L_0 \rangle}{\langle L_0 \rangle} \tag{4.1}$$

where $\langle L_0 \rangle$ is the average length of (at least) ten samples prior the addition of DNA reactants. and $\langle L_i \rangle$ is the average length of (at least) ten gel samples at time $t_i$. Furthermore, the average length of each sample at any time point was itself calculated as the average length of two adjacent sides. It was assumed that $\langle L_i \rangle$ and $\langle L_0 \rangle$ are independent random variables and, as a result, that the error can be approximated by the following expression:

$$Error \approx \sqrt{\left(-\frac{\langle L_i \rangle}{\langle L_0 \rangle^2}\right)^2 s_{L_0}^2 + \left(\frac{1}{\langle L_0 \rangle}\right)^2 s_{L_i}^2} \tag{4.2}$$

where $s_{L_0}$ and $s_{L_i}$ represent the standard deviations of the initial, $t_0$, and final, $t_i$, length measurements, respectively.

Initially, we tested the swelling response of hydrogels crosslinked with 3-strand DNA complexes of the design previously used by Lin *et al.*[40] Since a hydrogel crosslinked with only one set of DNA crosslinker complexes would liquefy upon crosslink disruption, an orthogonal DNA crosslinker – of the same secondary structure – was added to the pregel solution (Figure 4.4A). After photopolymerization the resulting gel was crosslinked by two orthogonal sets of DNA complexes, thereby preventing the complete dissolution of the poly(Am-co-DNA) upon the addition of a release strand to disassemble one of the crosslinker complexes (Figure 4.4A).

Poly(Am-co-DNA) hydrogels were initially fabricated containing 0.577 mM of each DNA crosslinker complex, thus bringing the total DNA crosslinker concentration to 1.154 mM. This is consistent with DNA crosslinker concentrations used in the swelling studies presented in Chapter 3. See Table 4.1 for DNA sequence information. As shown in Figures 4.5 and 4.6, the swelling of these gels in response to either DNA strand REF (the release strand for the E•F•LEF crosslinker complex) or DNA strand R1 (the release

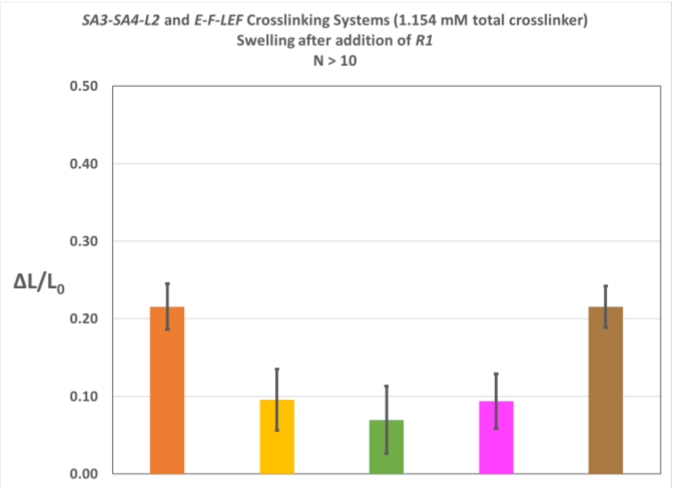

**Figure 4.5 Swelling after addition of strand R1.** Swelling of poly(Am-co-DNA) hydrogels containing crosslinker complexes E•F•LEF and SA3•SA4•L2, each of which is at 0.577 mM. DNA strand R1 reacts with the latter complex to remove the linker (L2) ssDNA. The swelling reaction was allowed to proceed for at least 24 hours. Individual batches of samples (i.e., from an individual pregel solution) are represented by different colors in the bar plot. Error bars are calculated according to Eqn 4.2.

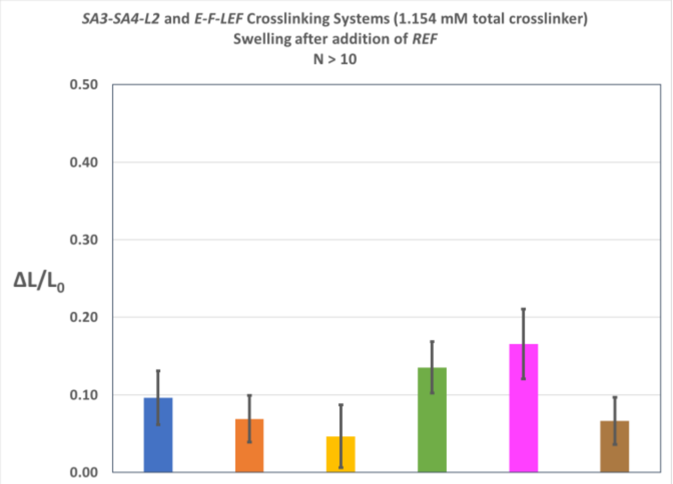

**Figure 4.6 Swelling after addition of strand REF.** Swelling of poly(Am-co-DNA) hydrogels containing crosslinker complexes E•F•LEF and SA3•SA4•L2, each of which is at 0.577 mM. DNA strand REF reacts with the former complex to remove the linker LEF strand. The swelling reaction was allowed to proceed for at least 24 hours. Individual batches of samples (i.e., from an individual pregel solution) are represented by different colors in the bar plot. Error is calculated according to Eqn. 4.2.

strand for the SA3•SA4•L2) was investigated. Both strand REF and R1 were added to approximately 8x mole excess relative to the crossslinker concentration (assuming 100% incorporation during radical chain copolymerization). In either case, over multiple different batches of samples, the gels never swelled more than 0.30 – far below what was predicted necessary to achieve deformation of DNA- or BIS-crosslinked hydrogel devices. Assuming that each DNA crosslinking complex has similar levels of reactivity with acrylamide monomers during radical chain polymerization, then it would be expected that disrupting either the E•F•LEF or SA3•SA4•L2 crosslinker complex would lead to similar levels of uniaxial swelling, which was observed among the repeated swelling experiments. Among all swelling experiments similar levels of variation were observed.

With equimolar amounts of each crosslinking complex the largest decrease in crosslink density, and concomitant increase in swelling, that one can expect to achieve is 50%. To increase this value, poly(Am-co-DNA) gels were fabricated containing twice the total concentration of DNA crosslinker complex and, more importantly, skewed relative concentrations of each crosslinker complex. Seventy percent and ninety percent reductions in crosslink density were attempted by adding R1 strand to gels containing 70/30 and 90/10 ratios of SA3•SA4•L2/E•F•LEF crosslinker complexes, respectively. Unfortunately, these swelling experiments yielded uniaxial swelling values similar to what we achieved with a 1.154 mM total DNA crosslinker concentration.

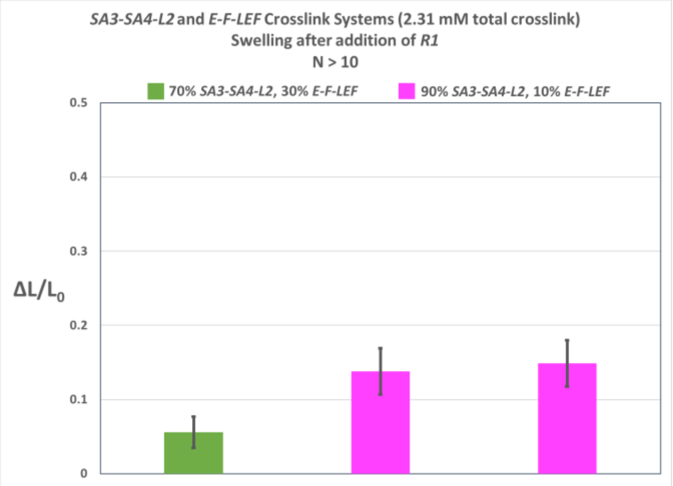

**Figure 4.7 Swelling of poly(Am-co-DNA) hydrogels containing higher proportions of removable crosslinker.** The total concentration of DNA crosslinker complex is 2.31 mM. One batch of gels was produced with a 70/30 distribution of SA3•SA4•L2/E•F•LEF crosslinker complexes, whereas another batch was produced with a 90/10 distribution of SA3•SA4•L2/E•F•LEF crosslinker complexes. Two groups of samples from the 90/10 batch were swelled (magenta bars). Error is calculated according to Eqn. 4.2.

In light of the results obtained with crosslinker designs from Lin *et al.*'s 2004 publication, poly(Am-co-DNA) hydrogels were synthesized containing the "tensegrity" design in their 2005 publication.[39] The secondary structure of this complex differs from the 2004 design via the insertion of a 40 nucleotide single-stranded region into the linker strand – referred to as L3 in the 2005 design – between the domains that hybridize to the acrydite-modified strands SA1 and SA2 (Figure 4.8). Upon hybridization of an external fuel strand, termed F1, to the single-stranded region in L3, the crosslinker complex stiffens and can act as a rigid strut capable of supporting external loads applied to the gel. It was thought that there would some swelling accompanying this stress-generating process. Additionally, since the crosslinker complex maintains contact with both original polyacrylamide backbone strands throughout this stiffening process, only a single DNA crosslinker set would be necessary to maintain the integrity of the gel and prevent dissolution. Unfortunately, this stiffening process exhibited swelling extents smaller than that shown for gels crosslinked with DNA complexes taken from Lin *et al.*'s 2004 publication (Figure 4.9).

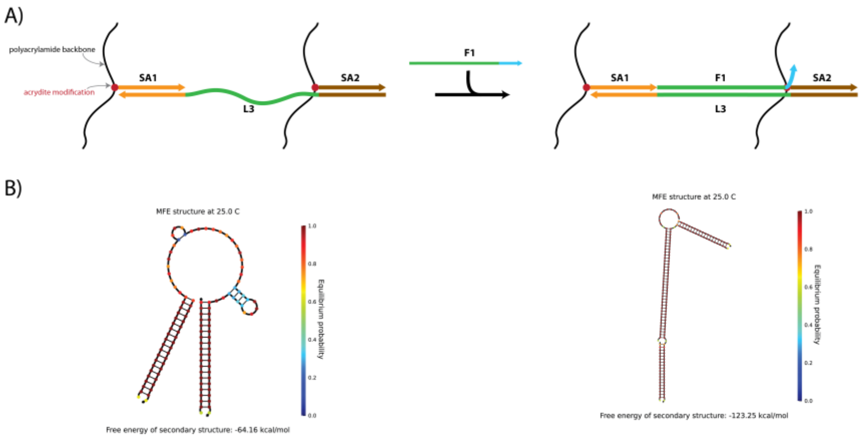

**Figure 4.8 Tensegrity crosslinker design and NUPACK thermodynamic analysis.** (**A**) Design of crosslinker motif taken from Lin *et al.*'s 2005 publication (see reference 45). The addition of the fuel F1 strand increases the stiffness of the crosslinker complex and induces swelling. (**B**) NUPACK simulation of the thermodynamic stability of the crosslinkber complex before (left) and after (right) the addition of F1 strand. The low probability of forming secondary structures within the 40 nucleotide single-stranded region is not believed to impact the swelling reaction.

It was thought that the insufficient swelling obtained from employing Lin *et al.*'s 2005 tensegrity crosslinker design stemmed from the small change in length accompanying the transition of the linker strand from partially double-stranded to fully double-stranded. Therefore, the 40 nucleotide single-stranded region in L3 was redesigned to contain a hairpin (14 basepair stem and 4 base loop) domain that, when opened via the addition of a corresponding fuel strand F1hp, would form a linear DNA duplex (Figure 4.10). To ensure that the swelling of the poly(Am-co-DNA) gels is not limited by the kinetics of the hairpin-opening reaction, an eight-base toehold domain was inserted directly adjacent (on the 3' side) of the hairpin domain. Upon the

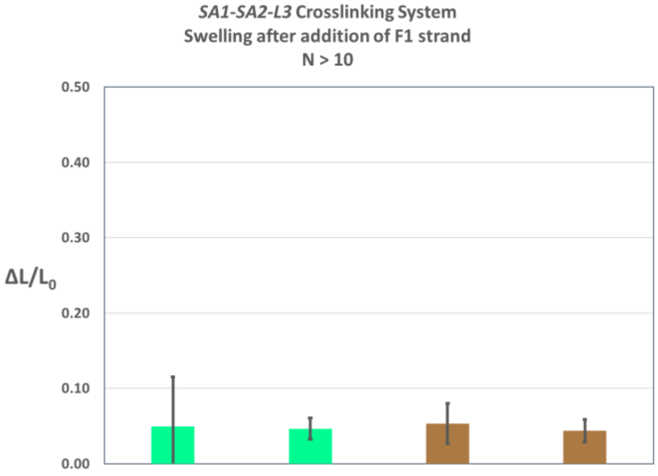

**Figure 4.9 Swelling upon addition of F1 strand to poly(Am-co-DNA) gels crosslinked with SA1•SA2•L3.** Bars with the same color represent swelling results of gels from the same original batch (i.e., pre-gel solution). Error is calculated according to Eqn. 4.2.

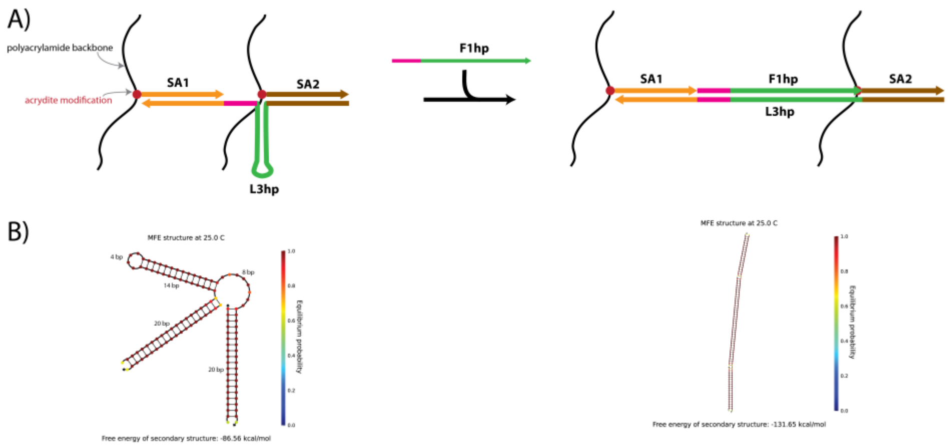

**Figure 4.10 Hairpin crosslinker design and thermodynamic stability.** (**A**) DNA hairpin crosslinker design. The hairpin domain – stem and loop – are colored green, whereas the eight base toehold region directly adjacent is colored magenta. (**B**) Minimum free energy structure at 25 ℃ of the hairpin crosslinker before addition of fuel F1hp strand (left) and after (right).

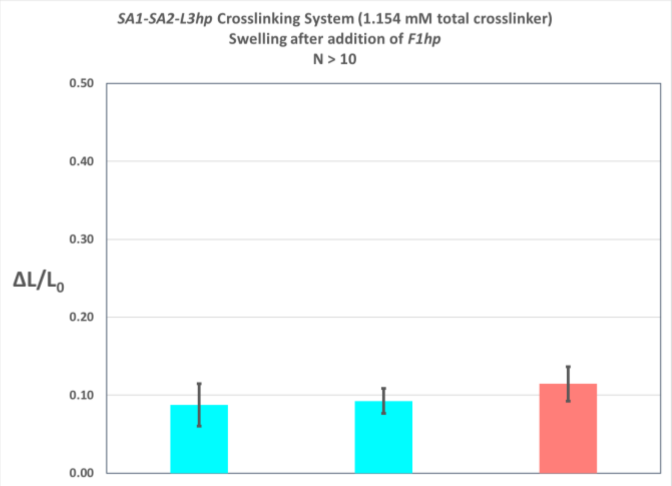

**Figure 4.11 Swelling upon addition of F1hp strand.** Bars with the same color represent swelling of gels from the same batch (i.e., pre-gel solution). Error is calculated according to Eqn 4.2.

addition fuel strand – here termed F1hp – the poly(Am-co-DNA) hydrogels swelled roughly ten percent – too small to achieve mechanical actuation in a soft matter device comprised of poly(Am-co-BIS) and poly(Am-co-DNA) hydrogels (Figure 4.11).

## 4.3 CONCLUSION

Successful fabrication, swelling, and mechanical actuation of the hydrogel devices presented in Chapter 3 required testing of various materials and DNA crosslinker designs, respectively. Due to its chemoselective gelation/dissolution response, as well as mechanical robustness, $Ca^{2+}$-crosslinked PAA is by far the superior candidate for a sacrificial layer when compared to $Ca^{2+}$-crosslinked alginate and poly(Am-co-DNA). Likewise, the high-degree swelling of poly(Am-co-DNA) hydrogels via the autonomous polymerization mechanism detailed in Chapter 3 ($\Delta L/L_0$ ~ 3.8) also far outperforms the alternatives presented here. The swelling extents provided by the crosslinker designs of Lin *et al.* do not approximate the swelling necessary to achieve actuation of DNA- or BIS-crosslinked hydrogel devices.

## 4.4 MATERIALS & METHODS

### 4.4.1 Preparation of substrates with $Ca^{2+}$-crosslinked alginate sacrificial layer

The substrates with alginate sacrificial layer were prepared by first sonicating plain glass slides (25 mm x 75 mm x 1 mm thick) in 10% (wt/vol) NaOH solution for 30 minutes, drying with N2 gas, and etching with O2 plasma for three minutes. Next, a 2% (wt/vol) solution of uncrosslinked alginate was prepared by dissolving sodium alginic acid (Scientific Polymer Products, Inc.) into MilliQ water. Approximately 2 mL of alginate solution was then aliquoted onto a clean glass slide and spun at 1,000 rpm to achieve a layer approximately 10 microns thick. To crosslink the alginate, the pre-gel sacrificial layer was then gently sprayed with 250 mM $CaCl_2$. Two minutes after spraying, 2-3 mL of 250 mM $CaCl_2$ was then aliquoted onto the glass slide, after which the glass slides left alone for 3 minutes to allow for additional crosslinking to occur. Excess 250 mM $CaCl_2$ was removed from the substrates and replaced with 2-3 mL of 2 mM $CaCl_2$. The slides were then twice washed with MilliQ water and left out at room temperature overnight to dry.

### 4.4.2 Preparation of substrates with poly(Am-co-DNA) sacrificial layer

The poly(Am-co-DNA) pre-gel solution was prepared according to the protocol given in § 3.4.2. The SA3, SA4, and L2 strands were not annealed prior to adding the acrylamide monomers or Irgacure 2100 photoinitiator. After the glass slides were cleaned via sonication in 10% NaOH solution, roughly 13 $\mu$L of the pre-gel solution was dropcast onto the glass slide. The slide was then exposed to 365 nm UV light (intensity in the range of 5-8 mW/cm$^2$) for 225 seconds. This substrate was then used to assemble a photolithography chamber (as described in § 3.4.3). Next, a poly(Am-co-BIS) pre-gel solution consisting of 5% (wt/vol) of 19:1 Am:BIS (BioRad Laboratories, Inc., catalog #1610144), TAE/$Mg^{2+}$, and 10% (vol/vol) of Irgacure 2100 was prepared and aliquoted into the assembled photolithography chamber. The chamber was then exposed to 30 seconds of 365 nm UV light to pattern the BIS-crosslinked hydrogels.

The poly(Am-co-DNA) sacrificial layer was then visualized by staining the patterned area with 100 $\mu$L of 100x SYBR Gold stain (Invitrogen, Inc., catalog #S11494) and imaging in a gel imaging box (Syngene EF2 G:Box) equipped with a blue light transilluminator (Clare Chemical, emission max ~450 nm) and a UV032 filter (Syngene, bandpass 572-630 nm).

### 4.4.3 Poly(Am-co-DNA) gel fabrication and swelling studies

The preparation of the poly(Am-co-DNA) pre-gel solution and subsequent photopatterning followed the protocols outlined in § 3.4. After patterning, the gels were stained overnight in a solution of 2x SYBR Green I nucleic acid stain (Invitrogen catalog #S7563). Before swelling, the gels were washed with excess TAE/$Mg^{2+}$ to remove unbound SYBR Green I dye. In all swelling experiments, the release (R)- or fuel (F1)-based strands were present in 8x mole excess relative to the crosslinker concentration. Again, this assume 100% incorporation of the crosslink complex during radical chain polymerization. The swelling of the gels was monitored by fluorescence microscopy using a Nikon AZ100 stereoscope (see § 3.4 for filter cube details). Gels were allowed to swell for at least 24 hours to allow DNA-induced swelling reactions to reach equilibrium.

**Table 4.1 DNA Sequences**

| Strand Name | Strand Sequence |
|---|---|
| SA1 | ACGGAGGTGTATGCAATGTC |
| SA2 | CATGCTTAGGGACGACTGGA |
| L3 | TCCAGTCGTCCCTAAGCATGTGTTCGACGGTACAAGAAGAGGGTTACGCTAATGAGTGCTGACATTGCATACACCTCCGT |
| F1 | AGCACTCATTAGCGTAACCCTCTTCTTGTACCGTCGAACAGATAGAGCTG |
| SA3 | AGCTGGATCTGAGGATTAGT |
| SA4 | AGTATCGCACACACCTACTT |
| L2 | ACTAATCCTCAGATCCAGCTAAGTAGGTGTGTGCGATACTTTACATTGAT |
| R1 | ATCAATGTAAAGTATCGCACACACCTACTTAGCTGGATCTGAGGATTAGT |
| E | ACGGAGGTGTATGCAATGTC |
| F | CATGCTTAGGGACGACTGGA |
| LEF | TCCAGTCGTCCCTAAGCATGGACATTGCATACACCTCCGTAGTGTTGGTC |

| | |
|---|---|
| REF | GACCAACACTACGGAGGTGTATGCAATGTCCATGCTTAGGGACGACTGGA |
| L3hp | TCCAGTCGTCCCTAAGCATGGCGAGGCTGTGCCGTTTTCGGCACAGCCTCGCTCGTAGTGGACATTGCATACACCTCCGT |
| F1hp | CACTACGAGCGAGGCTGTGCCGAAAACGGCACAGCCTCGC |

## 4.5 ACKNOWLEDGMENTS

I thank C.K. Yoon for assistance in fabricating and imaging the hydrogels, and D. Gracias for discussions and general technical assistance. Additionally, I thank J. Liu, J. Guo, and V. Nguyen for enlightening discussions regarding hydrogel swelling mechanics.

# CHAPTER 5 FORCE-SENSING DNA COPOLYMER HYDROGELS

## 5.1 INTRODUCTION

The construction of synthetic materials capable of initiating chemical reactions in response to external mechanical stimuli, i.e., mechanochemically responsive (MCR) materials, is an area of intense focus within the material science community.[103,104] In recent years, the covalent attachment of mechanophores – molecules that undergo chemical transformations when subjected to mechanical forces – to organic polymer backbones has been one method of imbibing materials with MRC-type behavior.[105] In this design, forces applied to the macroscopic material are transduced to the mechanophore via the polymer network. When sufficiently high forces are applied to the polymer network, the mechanophore undergoes a chemical transformation and produces an output signal (e.g., increased fluorescence, Figure 5.1). To predict the behavior of mechanophore-conjugated materials, microphysical models have been developed that couple the kinetics of mechanophore activation to the macroscopic deformation experienced by the polymeric material.[106,107] While these approaches have yielded materials with predictable chemical responses to external mechanical stimuli, no MCR materials capable of biomolecular outputs have been developed.

One way to construct MCR materials capable of interfacing with biological systems is to employ a biomolecule as the mechanophore. Ideally, the response of this biomolecule to mechanical forces should be well-characterized, and the use of this biomolecule as an engineering material should be well-documented. The latter point is crucial since this will facilitate integration ohjymnjf the force sensing mechanism to downstream chemical reactions and outputs. One biomolecule that fits this description is undoubtedly DNA:

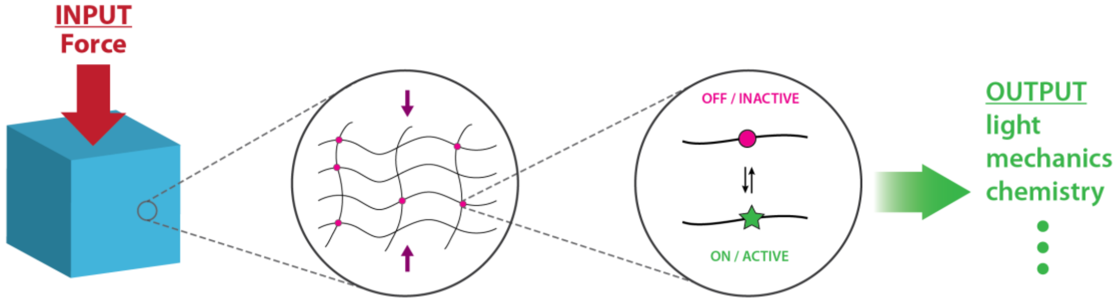

**Figure 5.1 Schematic of MCR material.** The mechanical force applied to the macroscale material is transduced to the inactive mechanophore crosslinks (magenta circles) via the polymer network. When sufficient forces are reached, the mechanophore undergoes a chemical transformation and emits an output (e.g. light, chemical reactions, change in mechanical properties of the MCR material, etc.).

over the past several decades elaborate circuits,[23,108] nanostructures,[109,110] and molecular-scale motors[111,112] have been constructed entirely from DNA while, over roughly this same period time, the advent of single-molecule experimental techniques has enabled a quantitative understanding of the response of DNA to mechanical forces present in cells.[113] Using optical tweezers, for example, RNA polymerase was estimated to exert roughly 20 pN of force on DNA polymers during transcription in *E. coli* bacteria.[114,115] On the other hand, during DNA replication T7 DNA polymerase has been shown to generate forces as high as 35 pN on DNA polymers.[116,117]

Furthermore, knowledge of the stress-strain behavior of individual DNA molecules has enabled their use as a molecular force sensor.[118] Wang and Ha, for example, used DNA duplex shear and unzipping force sensors to gauge the force of cell adhesion to the extracellular matrix as well as the force required to activate the Notch signaling pathway.[119] In similar fashion, Zhang *et al.* used hairpin force sensors to estimate the force dynamics experienced by a population of integrin molecules during the formation of focal adhesions.[120] Herein we detail the design, construction, and characterization of similar force-sensing DNA complexes which we conjugate to a hydrophilic polymer network. These efforts culminate in the synthesis of a proof-of-concept, programmable MCR material capable of interfacing with biological systems via the production of initiating biomolecular reactions in response to external mechanical forces.

## 5.2 RESULTS & DISCUSSION

### 5.2.1 Theory: Arruda-Boyce model

In order to rationally design a force sensing gel equipped with a mechanophore, the relationship between stress and strain of the bulk material and the forces experienced by the polymer network must be determined. Here, an Arruda-Boyce based-model was used to derive the forces felt by the polymer network as a function of the stretch of the bulk material. To start, the overall free energy of the hydrogel, $W$, is assumed to be the sum of two components: the stretching of the polymer network and the thermodynamic mixing of the polymer network and solvent molecules,[93]

$$W = W_{stretch} + W_{mixing} \tag{5.1}$$

where $W_{stretch}$ and $W_{mixing}$ are the contributions from stretching and mixing, respectively. We assume that all molecular components of our system are incompressible and therefore can undergo configurational changes without a change in volume (i.e., can change their shape much easier than they change their volume). This principle is expressed as

$$J = 1 + \nu C = \det(\boldsymbol{F}) \tag{5.2}$$

where $\nu$ is the volume of the solvent molecules, $C$ is the number of solvent molecules per polymer volume, $\boldsymbol{F}$ is the deformation tensor, and $J$ is the Jacobian. The determinant of the deformation tensor represents the overall volume change of the gel. Molecular incompressibility can be enforced by constraining the system via a Lagrange multiplier, $\pi$, thus giving the total free energy expression of a hydrogel:

$$W = W_{stretch} + W_{mixing} - \pi[1 + \nu C - \det(\boldsymbol{F})] \tag{5.3}$$

The free energy of mixing the long polymer chains and solvent molecules can be expressed using Flory-Huggins theory[84] as,

$$W_{mixing} = \frac{kT}{\nu}\left[\nu C \log\left(\frac{\nu C}{1 + \nu C}\right) + \chi \frac{\nu C}{1 + \nu C}\right] \tag{5.4}$$

where $k$ is the Boltzmann constant and $\chi$ is the dimensionless Flory-Huggins parameter that describes the propensity of the polymer strands and solvent molecules to mix. If $\chi$<0, then mixing of the polymer strands and solvent molecules becomes favorable, whereas if $\chi$>0, then mixing is unfavorable.

In Chapter 3 the free energy component due to stretching of the polymer chains was expressed using Neo-Hookean theory via the Ogden model.[97] Since we would like to relate the macroscopic stretch of our hydrogel to the stretch of individual polymer chains at high strains, the Arruda-Boyce model[121] was used to express $W_{stretch}$ as,

$$W_{stretch} = NkTn\left(\frac{\beta}{\tanh\beta} + \ln\frac{\beta}{\sinh\beta}\right) \tag{5.5}$$

where $N$ is the number of polymer chains per polymer gel volume, $n$ is the number of Kuhn segments per polymer chain between two crosslinkers, and $T$ is the absolute temperature in Kelvin. Here $\beta$ is defined as

$$\beta = L^{-1}\left(\frac{\lambda_{chain}}{\sqrt{n}}\right) \tag{5.6}$$

where $L^{-1}$ is the inverse Langevin function, which is defined as $L(x) = \coth(x) - 1/x$, and can be approximated as

$$L^{-1}(x) \approx x\frac{3-2.6x+0.7x^2}{(1-x)(1+0.1x)} \tag{5.7}$$

Lastly, the stretch of the individual polymer chains, $\lambda_{chain}$, is given by

$$\lambda_{chain} = \sqrt{\frac{\lambda_1^2+\lambda_2^2+\lambda_3^2}{3}} \tag{5.8}$$

where $\lambda_1$, $\lambda_2$, and $\lambda_3$ are the macroscopic stretches in the three directions. At equilibrium the Helmholtz free energy reduces to zero, giving the expression

$$dW - S_1 d\lambda_1 - S_2 d\lambda_2 - S_3 d\lambda_3 - \mu dC = 0, \qquad \text{where } \mu = \frac{dW}{dC} \tag{5.9}$$

where $S_1$, $S_2$, and $S_3$ are the three principle nominal stresses and $\mu$ is the chemical potential. Inserting the derivative of Eqn. 5.3 into Eqn 5.9, and noting the expression for $\mu$ above, yields the following equations of state for a hydrogel:

$$\begin{aligned} S_1 &= \frac{NkT\sqrt{n}\beta}{3\lambda_{chain}}\lambda_1 + \pi\lambda_2\lambda_3 \\ S_2 &= \frac{NkT\sqrt{n}\beta}{3\lambda_{chain}}\lambda_2 + \pi\lambda_1\lambda_3 \\ S_3 &= \frac{NkT\sqrt{n}\beta}{3\lambda_{chain}}\lambda_3 + \pi\lambda_1\lambda_2 \\ \mu &= kT\left[\log\left(\frac{\nu C}{1+\nu C}\right) + \frac{\nu C}{1+\nu C} + \frac{\chi}{(1+\nu C)^2}\right] - \pi\nu \end{aligned} \tag{5.10}$$

Since no external forces are applied to our hydrogels in the $\boldsymbol{e_2}$ or $\boldsymbol{e_3}$ directions, $S_2$ and $S_3$ equal zero. It should be noted that $\lambda_2$ and $\lambda_3$ do not equal zero due material incompressibility and the assumed Poisson effect.

To calculate the force experience by a polymer chain upon deformation we start with an expression for the energy stored in a polymer chain. According to Langevin chain statistics[122] this can be expressed as follows:

$$\begin{aligned} w &= \frac{W}{N} = kTn\left(\frac{\beta}{\tanh\beta} + \ln\frac{\beta}{\sinh\beta}\right) \\ \beta &= L^{-1}\left(\frac{r}{nl}\right) = L^{-1}\left(\frac{\lambda_{chain}}{\sqrt{n}}\right) \end{aligned} \tag{5.11}$$

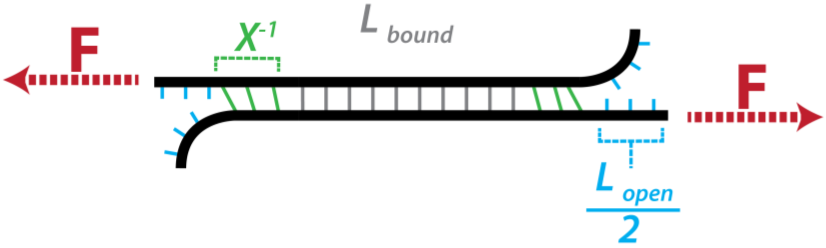

**Figure 5.2 deGennes model of shearing DNA duplex.** A force (here represented by $F$) applied to a DNA duplex of length $L_{bound}$ will be felt by $X^{-1}$ basepairs from the ends.

where $r$ is the end-to-end distance of one polymer chain between two crosslinkers and $l$ is the length of one Kuhn monomer. The force experienced by a polymer chain in a hydrogel can then be calculated as,

$$f = \frac{\partial w}{\partial r} = \frac{kT}{l} L^{-1}\left(\frac{\lambda_{chain}}{\sqrt{n}}\right) \tag{5.12}$$

### 5.2.2 Theory: DNA-based shear force sensors

A thorough understanding of how DNA nanostructures respond to varying external forces – e.g., shearing, unzipping, twisting, bending etc. – can not only further elucidate phenomena such as DNA replication and transcription but inform the discovery of nanostructures with novel functions. This understanding is crucial for the development of DNA force sensor nanostructures that rupture and execute a programmed series of chemical reactions upon the application of an external load. Due to the secondary structures of the force sensors we developed, we focus on the shearing behavior of DNA duplexes and the unzipping behavior of DNA hairpin structures.

In 2001 Pierre deGennes proposed that the force required to shear a DNA duplex does not indefinitely scale with duplex length, as had been previously thought, but approaches a maximum value as the duplex length increases.[123] Furthermore, he predicted that stress experienced by the DNA duplex is not evenly distributed to all the bases, but rather is felt by only a few bases located at the ends of the duplex (Figure 5.2). These bases, which are in mechanical equilibrium, are represented by the parameter $X^{-1}$ in the deGennes model. This result implies a certain elasticity to the phosphodiester backbone since if it was infinitely stiff, any applied force would be felt evenly across the duplex. According to deGennes's theory the critical force, $f_c$, necessary to shear a duplex of length $L_{bound}$ is given by the expression,

$$f_c = 2f_1\left[X^{-1}\tanh^{-1}\left(\frac{XL_{bound}}{2}\right)+1\right] \tag{5.13}$$

where $f_1$ is the force necessary to rupture a single basepair and $L_{bound} = L_{seq} - L_{open}$, with the total number of bases in the DNA sequence given by $L_{seq}$, and the number of bases not bound in duplex form given by $L_{open}$. It is assumed that at the initial application of external force $L_{open}$ is zero. The parameter $X^{-1}$ is defined as,

$$X^{-1} = \sqrt{\frac{Q}{2R}} \tag{5.14}$$

with $Q$ defined as the spring constant of stretching the DNA backbone and $R$ the spring constant of stretching the hydrogen bonds between the base pairs. In the case of an infinitely long DNA duplex, $\tanh(XL_{bound}/2) \rightarrow 1$, and the critical force required to shear a DNA duplex reaches a maximum, $f_m$, given by,

$$f_m = 2f_1[X^{-1}+1] \tag{5.15}$$

From single-molecule pulling experiments, Hatch *et al.* estimated that $f_1$ to be 3.9 pN, $X^{-1}$ to be 6.8 basepairs, and the ratio $Q/R$ to be 92.5.[124] They also demonstrated an approximately linear increase in $f_c$ from basepair lengths of 12 through 24, at which point $f_c$ approaches an asymptotic limit of roughly 61.4 pN.

### 5.2.3 Theory: DNA-based hairpin unzipping force sensors

The prevalence of DNA hairpin structures in physiologically-relevant biochemical pathways has made their structure and function very rich areas of research. Single-molecule techniques have made possible thermodynamic and kinetic descriptions of hairpin opening and closing transformations in the presence of external forces. To describe the behavior of our hairpin-based DNA sensor, we employ a model detailed by Woodside *et al.*[125] which combines the energy from DNA folding – i.e., the energy of duplex formation calculated via nearest-neighbor parameters[29] – and the energy from mechanical stretching of single-stranded DNA (ssDNA). The overall free-energy of a DNA hairpin under extension, $\Delta G$, is thus given by the expression,

$$\Delta G(f,x) = \Delta G_{fold}(x) + \Delta G_{stretch}(x) + f \cdot x \tag{5.16}$$

where $f$ is the externally exerted force on the hairpin, $\Delta G_{fold}$ is the free energy of duplex formation from hairpin folding, $\Delta G_{stretch}$ is the free energy of stretching ssDNA from $f = 0$ to $f = f_{\frac{1}{2}}$, which is the force at which 50% of DNA hairpins unfold. In essence, $\Delta G_{fold}$ represents the energy of hairpin folding at $f = 0$ and can be found by using any software suite that calculates the free energy of formation of DNA structures at equilibrium, e.g., NUPACK, IDT OligoAnalyzer 3.1, etc. The free energy from stretching, $\Delta G_{stretch}$, can be calculated using the worm-like chain model:

$$\Delta G_{stretch}(x) = \frac{k_B T}{L_p} \frac{L_0}{4\left(1 - \frac{x}{L_0}\right)} \left[3\left(\frac{x}{L_0}\right)^2 - 2\left(\frac{x}{L_0}\right)^3\right] \tag{5.17}$$

where $k_B$ is the Boltzmann constant, $T$ is the temperature, $L_p$ is the persistence length of ssDNA (~1.3 nm), $L_0$ is the contour length per nucleotide (~0.63 nm), and $x$ represents the hairpin extension from equilibrium calculated as $0.44 \times (n - 1)$ nm, where $n$ represents the number of bases comprising the hairpin. When $f = f_{\frac{1}{2}}$, the overall free energy $\Delta G(f, x)$ equals zero and Eqn 5.16 can be rearranged as follows:

$$f_{\frac{1}{2}} = \frac{\Delta G_{fold}(x) + \Delta G_{stretch}(x)}{\Delta x} \tag{5.18}$$

where $\Delta x$ represents the hairpin displacement needed for unfolding and is estimated to be $(x - 2)$ nm. Note that 2 nm is subtracted from $x$ since this represents the width of a DNA duplex.

### 5.2.4 Experimental determination of model parameters

Initially, two materials were considered for use as the polymeric backbone of the force sensor material: poly(ethylene glycol) diacrylate (PEGDA, $M_n \sim 575$) and poly(Am-co-BIS). To determine which of the two would allow for higher forces to be exerted on the polymeric backbone, and concomitantly the DNA force sensor complex, swelling and unconfined uniaxial compression experiments were performed to determine the values of $N$ and $n$ in the equations of state (Eqn 5.10). PEGDA and poly(Am-co-BIS) hydrogels were prepared according to the protocol given in § 3.4 and Figure S3.15, with PEGDA at a concentration of 10 % (wt/vol). In addition, one PEGDA gel was prepared and swelled in a sodium-based buffer (SPSC) since DNA duplexes are known to be less stable – and thus more apt to rupture – in the presence of monovalent cations.[126] On the other hand, divalent cations such as $Mg^{2+}$ are known to stabilize DNA duplexes to much larger extents, increasing the force required to shear or unzip a DNA duplex. From

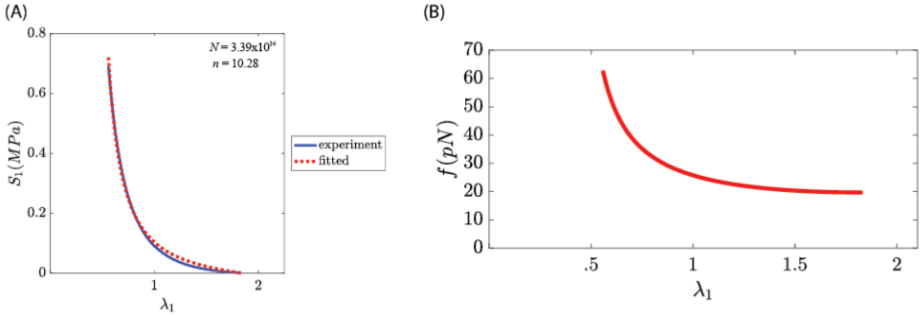

**Figure 5.3 Determining model parameters and the resulting chain force for a 10% PEGDA gel in SPSC buffer.** (**A**) 10% PEGDA hydrogels were swelled in sodium-based buffer and subjected to a controlled force, unconfined uniaxial compression test to produce nominal stress $S_1$ as a function of stretch $\lambda_1$. The equilibrium swelling ratio $Q$ was determined to be approximatley 6.2. The resulting data was then fit to the equations of state given in Eqn. 5.10, and the parameters $n$ and $N$ were determined to be 3.39x$10^{24}$ and 10.28, respectively. (**B**) The values of $n$ and $N$ were then used to calculate the force $f$ experienced by the polymer chains as a function of $\lambda_1$ according to Eqn 5.12.

the fitted $N$ and $n$ parameters (see Figure 5.3) it was derived that PEGDA-based gels could achieve chain forces in the range of 50-100 pN, whereas poly(Am-co-BIS)-based gels only reached values in the range 10-45 pN (data not shown). Therefore, PEGDA hydrogels prepared in sodium-based buffer were used to construct the force-sensing material.

### 5.2.5 Structure and qPCR testing of DNA force sensor complexes

As discussed in § 5.2.2 and § 5.2.3, depending on their secondary structure, DNA complexes can denature in response to a range of external forces. Since we desired to construct force sensor materials capable of responding to both large and small forces alike, two different DNA force sensor complexes were designed such that they would rupture in different force ranges. One of the complexes, a 24 basepair duplex herein referred to as the shear force sensor (SFS) (Figure 5.4), was designed to shear upon the application of roughly 60 pN to the polymer network (calculated using Eqn. 5.13). The other complex, herein referred to as the hairpin force sensor (HFS) (Figure 5.5), was comprised of a hairpin domain – comprised of a 13 basepair stem and 4 basepair loop – adjacent to a 21 basepair duplex. Due to the smaller forces necessary to unzip a hairpin stem compared to those needed to shear a DNA duplex, the HFS was estimated to rupture at forces

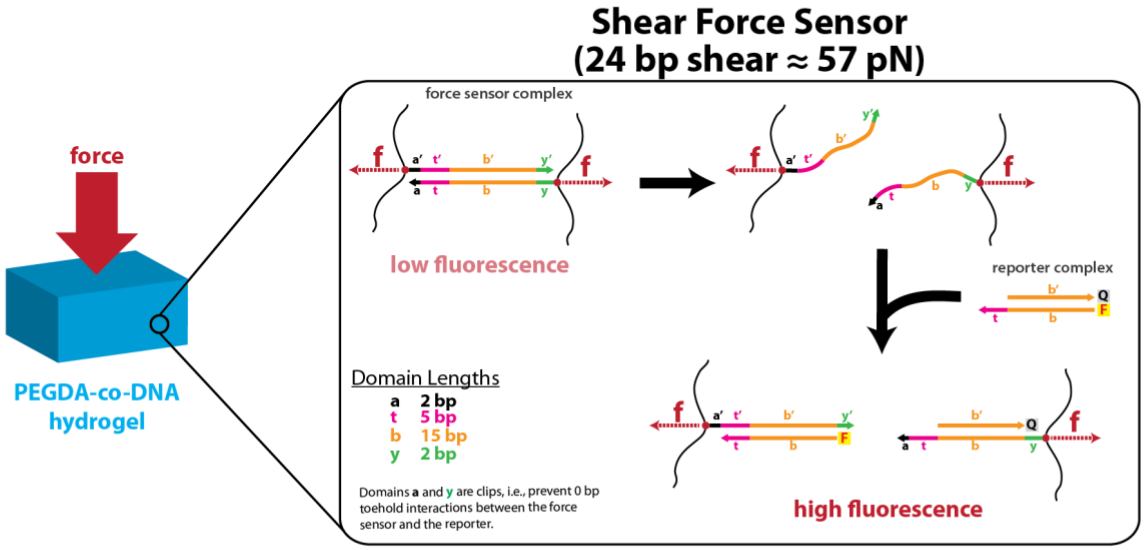

**Figure 5.4 Schematic of SFS.** Each strand of the shear force sensor (SFS) complex is modified with acrydite at the 5' end. The complex is incorporated into the PEGDA polymer network (represented by thin black lines) via radical chain polymerization. Colors indicate domain type and its complement. The toehold domain (magenta) is denoted by the letter *t*. Upon the application of roughly 57 pN of force, the DNA duplex ruptures, exposing a toehold domain which is able to react with the reporter complex and generate a fluorescence output.

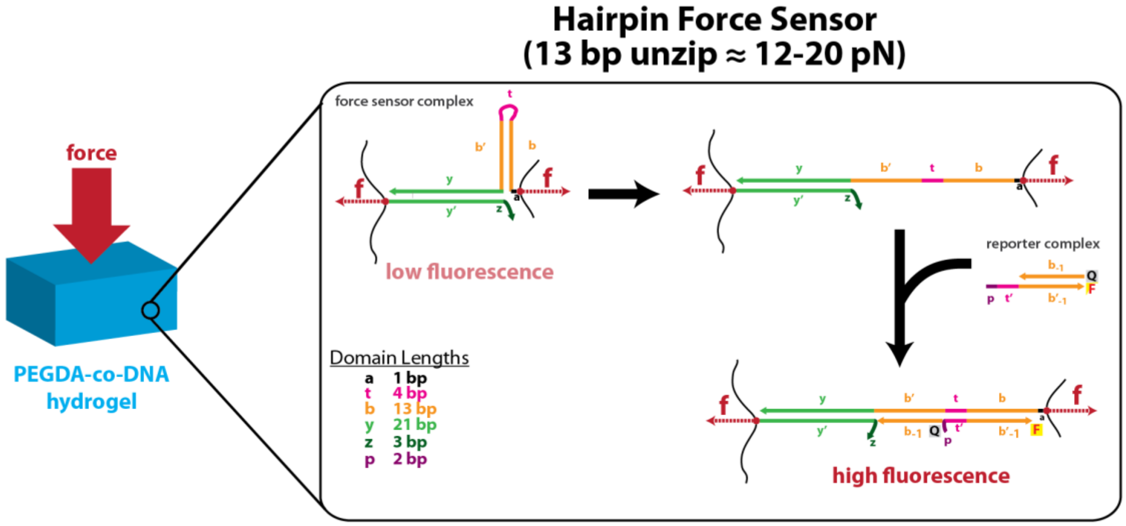

**Figure 5.5 Schematic of hairpin force sensor.** Depending on the free energy of formation of the hairpin complex, the hairpin force sensor (HFS) will rupture when subject to forces in the range of 12-20 pN. Colors indicate domain type and its complement. The toehold domain (magenta) is denoted by the letter *t*.

in the range of 13-20 pN. Both the HFS and SFS contain toehold domains that are sequestered when the force sensor is in its native inactive state but, upon rupturing, become exposed and able to participate in

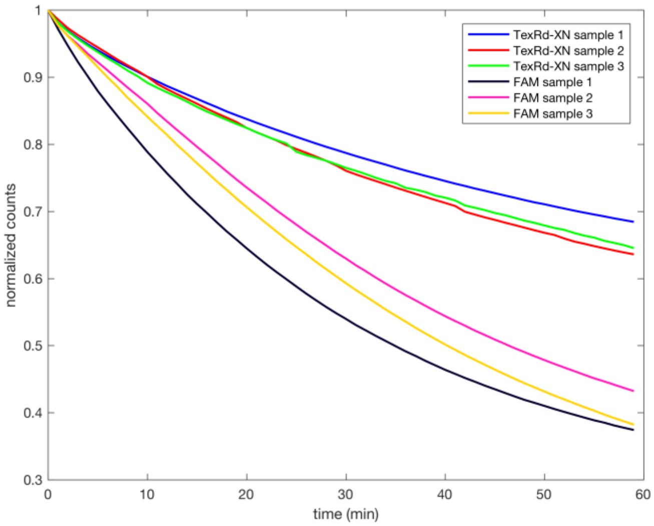

**Figure 5.6 Photobleaching extent of PEGDA gels equilibrated in solutions of ssDNA modified with FAM and Texas Red® fluorophore.** Normalized count values for gels equilibrated in either a solution of FAM-modified ssDNA (n=3) or Texas Red® modified DNA (n=3). Texas Red® photobleaches to a lesser extent and with slower kinetics.

downstream DNA-based reactions. For the studies conducted here, the toehold domains were designed to react with reporter complexes and produce a fluorescence output.

It is well-established that fluorophores bleach upon extensive exposure to light at wavelengths within their excitation range. To mitigate the reduction of outuput signal from photobleaching, we performed a quick experiment to determine the optimal fluorophore to use in our reporter complex. The fluorophore choices were initially narrowed to two: a fluorescein derivative termed FAM, and Texas Red®. To test which fluorophore experiences less bleaching, 10 % (wt./vol.) PEGDA gels were fabricated, swelled to equilibrium in SPSC buffer, and then allowed to soak in 100 nM solutions of ssDNA containing either a FAM fluorophore modification, or a Texas Red® fluorophore modification. The gels were then continuously exposed to light in their respective excitation ranges for approximately one hour, with fluorescence micrographs captured every minute. A plot of the normalized fluorescence intensity of each gel (three samples for each fluorophore) over time clearly indicates that the Texas Red fluorophore photobleaches to a lesser extent and with slower kinetics (Figure 5.6).

Unwanted leak reactions are always a concern in DNA-based schemes.[108] In the context of the force sensing schemes outlined in Figs 5.5 and 5.6, the presence of leak reactions would produce a false signal.

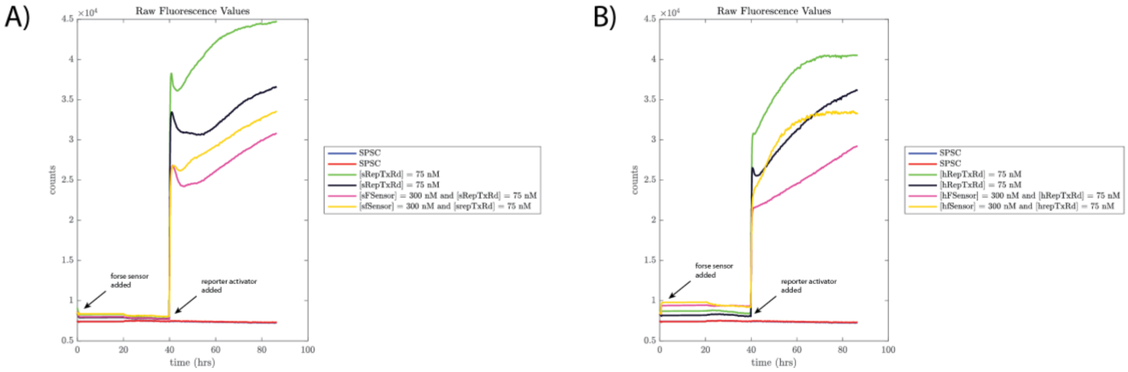

**Figure 5.7 Force sensor leak quantitated with qPCR.** In each case the force sensor was added after an initial baseline fluorescence was achieved with a solution of SPSC buffer and reporter complex. (**A**) Fluorescence profile of a well-mixed solution of the SFS and its reporter complex. No leak (i.e., premature activation) of the force sensor is apparent. (**B**) Fluorescence profile of a well-mixed solution of the HFS and its reporter complex. A slight leak (~5 %) is apparent with the HFS.

Therefore, the propensity of each force sensor complex in its native, inactive state to react with its respective reporter complex was tested in well-mixed solution using quantitative PCR techniques (see § 5.4.4 for experimental details). The HFS complex was slightly leaky relative to the approximately fully-activated reporter complex (~5 %), whereas the SFS complex exhibited approximately no leak (Figure 5.7). The failure of the fluorescence profile in either Fig. 5.7A or B to reach an equilibrium value makes a precise determination of force sensor leak impossible. This will need to be rectified in future experiments.

### 5.2.5 Compression of gels with various force sensor designs

Upon verifying the integrity of the force sensor complexes via qPCR, macroscale cylinder-shaped poly(PEGDA-co-SFS) and poly(PEGDA-co-HFS) hydrogels (~ 3 mm height, 4 mm diameter) were prepared according to the protocol detailed in § 5.4.2. After one sample of each was successfully fabricated via standard photopolymerization and micromolding techniques – akin to those used in Chapter 3 – the gels were immersed in a 500 nM solution of their respective reporter complex and allowed to equilibrate over at least 48 hours. To investigate the fluorescence dynamics of the material subject to an external load, a multifunctional force microscope (MFM)[127] was used to uniaxially compress the gels in the z-direction while simultaneously capturing fluorescence micrographs of the samples from below. In short, the MFM instrument is an epifluorescence (i.e., inverted) microscope equipped with a cantilever on a z-translation stage. As the height of the z-translation stage decreases, the cantilever lens comes into contact with the sample, which then

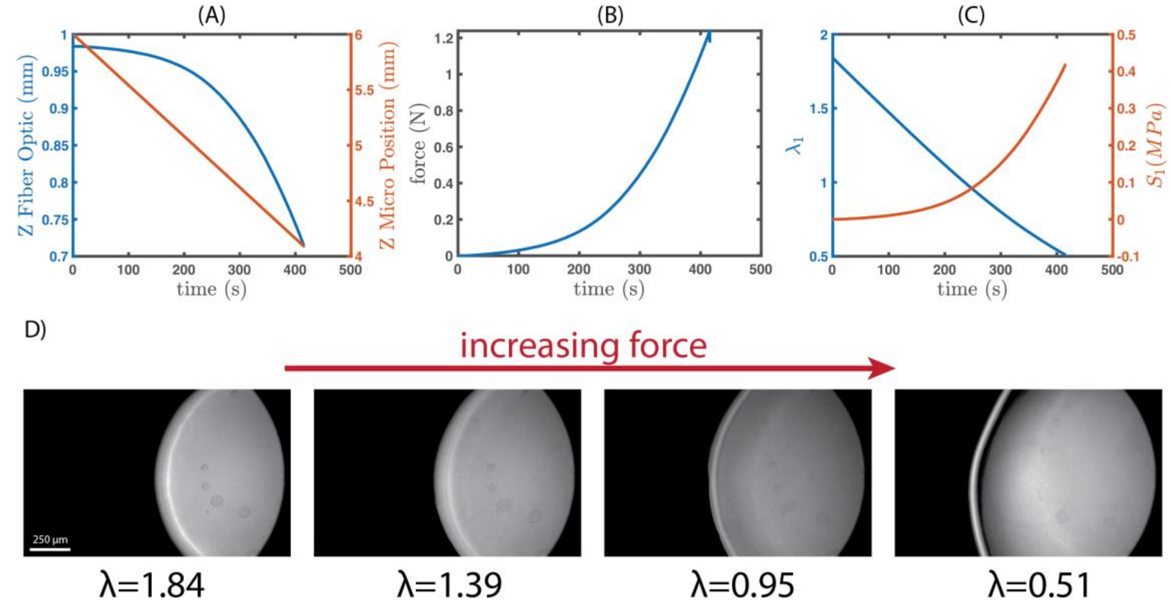

**Figure 5.8 MFM profile of poly(PEGDA-co-SFS) force sensing gel.** (**A**) The deflection of the MFM cantilever during uniaxial compression of the sample is represented by the decrease in distance between the z-fiber optic cable and the mirror placed on top of the cantilever (blue plot). The z-microtranslation stage decends onto the sample at a constant strain rate of 0.2% of the sample height. (**B**) The static force applied to the SFS gel is calculated via Hooke's law ($k_s =$ 4602 N/m, see § 5.4.3). (**C**) Uniaxial stretch $\lambda_1$ and nominal stress $S_1$ of the gel during loading are calculated using the equilibrium swelling ratio $Q$ of a 10% PEGDA hydrogels in sodium-based buffer. The reference state for these calculations is the dry, undeformed state of the PEGDA polymer network. (**D**) Fluorescence micrographs of the poly(PEGDA-co-SFS) gel during uniaxial compression. The images were linearly scaled to the maximum and minimum pixel intensity values of the entire set of images obtained during the run. The scale bar is 250 $\mu$m.

experiences a load. As the z-translation stage continues to descend the cantilever is deflected vertically (Figure 5.8A), the extent of which is measured by the fiber optic probe and mirror on top of the cantilever. The stiffness of the cantilever, represented by the spring constant by $k_s$, has previously been determined by Roberts *et al.*[127] The load applied to the sample can be calculated simply by using Hooke's law (see § 5.4.3). For the poly(PEGDA-co-SFS) sensor gel, a maximum load of 1 N and stretch value of 0.5 was attained upon unconfined compression of the sample (Figure 5.8B and C). The force sensing gel appeared to increase in fluorescence as stretch values of 0.6 and below were obtained (Figure 5.8D), indicating activation of the DNA mechanophore. This response qualitatively coincides with the polymer network forces necessary to shear the SFS duplex (Figure 5.3). On the other hand, the fluorescence intensity of the poly(PEGDA-co-HFS) force sensing gel appeared to decrease upon uniaxial compression (Figure 5.9). Since the HFS mechanophore is predicted to activate under loads of roughly 12-18 pN – approximately a third of those required for the SFS –a positive fluorescence output was expected from the poly(PEGDA-co-HFS) sample.

Our contrary findings could be the result of the lower mechanical load experienced by the HFS gel relative to the SFS gel (Figure 5.9B), or – more likely – the activation of the HFS mechanophore from the swelling of the gel to equilibrium in SPSC buffer prior to compression (see Figure 5.3). Further experimentation is needed to confirm the activation of the poly(PEGDA-co-SFS) gel as well as the absence of fluorescence output with respect to the poly(PEGDA-co-HFS) gel.

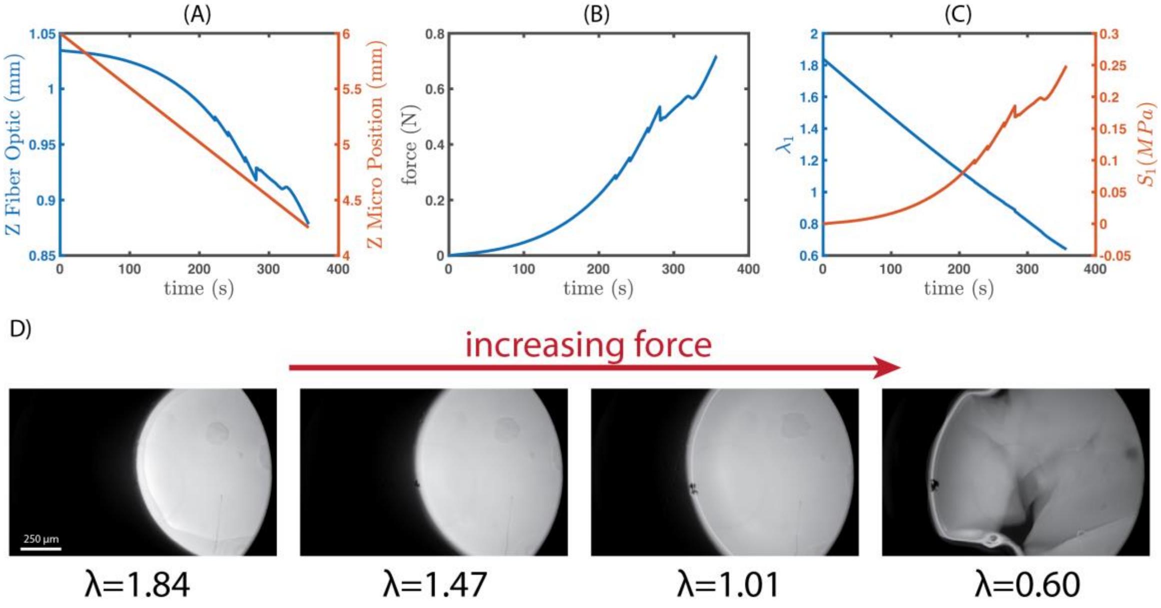

**Figure 5.9. MFM profile of the poly(PEGDA-co-HFS) force sensing gel.** (**A**) The z-microtranslation stage decends onto the sample at a constant strain rate of 0.2% of the sample height. (**B**) The static force applied to the SFS gel is calculated via Hooke's law ($k_s = 4602$ N/m, see § 5.4.3). (**C**) Uniaxial stretch $\lambda_1$ and nominal stress $S_1$ of the gel during loading are calculated using the equilibrium swelling ratio $Q$ of a 10% PEGDA hydrogels in sodium-based buffer. The reference state for these calculations is the dry, undeformed state of the PEGDA polymer network. (**D**) Fluorescence micrographs of the poly(PEGDA-co-SFS) gel during uniaxial compression. The images were linearly scaled to the maximum and minimum pixel intensity values of the entire set of images obtained during the run. The scale bar is 250 $\mu$m.

## 5.3 CONCLUSION

DNA is an ideal biomolecular mechanophore due to the detailed understanding of its single-molecule mechanics as well as its established record as an engineering material. As exemplified by our design of simple duplex and hairpin-based force sensor complexes, the large space of possible secondary structures enables the construction of force sensors tuned to different force. While further experimentation is needed to fully characterize and quantify the response of DNA copolymer MCR gels, the results presented herein suggest the possibility of a new class of materials capable of autonomously and programmably interacting with biological systems.

## 5.4 MATERIALS & METHODS

### 5.4.1 DNA sequences and preparation of DNA stock solutions

All oligonucleotide sequences are listed in Table 5.1 and were supplied by Integrated DNA Technologies (IDT) in their lyophilized form. The reporter strands containing a Texas Red®-X NHS Ester modification were ordered HPLC-purified. All other strands were purified via a standard desalting protocol. Stock solutions were prepared by resuspending the lyophilized samples with MilliQ water up to the desired concentration, which was verified by absorbance spectroscopy at 260 nm. Stock solutions of force sensor complex were prepared by annealing 50 $\mu$M of each force sensor DNA strands in SPSC (1 M NaCl, 50 mM $Na_2HPO_4$, pH ~ 7.5) buffer using an Eppendorf Mastercycler PCR; the annealing protocol consisted of incubating the solution at 90 °C for five minutes, followed by cooling the solution from 90 °C to 20 °C at 1 °C per minute to allow the strands to hybridize. SPSC buffer was used in lieu of $Mg^{2+}$-based buffers since DNA duplexes are more stable – i.e., have a lower $\Delta G_{fold}$ – when formed in the presence of divalent cations. To make the DNA force sensor complexes less stable, and more apt to rupture under a given load from the polymer backbone, sodium was chosen as the cation that would stabilize our DNA complexes.

**Table 5.1 Sequences for the SFS, HFS, and their respective reporter complexes.**

| Strand Name | Sequence (5' to 3') |
|---|---|
| SFS_1 | /5ACryd/CGCATCTCACATAACAACCACAGC |
| SFS_2 | /5ACryd/GCTGTGGTTGTTATGTGAGATGCG |
| SFS_Rep_F | /5TexRd-XN/TGTGGTTGTTATGTGAGATG |
| SFS_Rep_Q | CACATAACAACCACA/3IAbRQSp/ |
| HFS_1 | /5Acryd/TAGACAGGAAAAGAAGAATCTTTTCCTGTCTGCCTACCACTCCGTTGCGAAT |
| HFS_2 | /5Acryd/ATTCGCAACGGAGTGGTAGGCTTT |
| HFS_Rep_F | TTTTCTTCTTTTCCTGTC/3TxRed-XN/ |
| HFS_Rep_Q | /5IAbRQ/GACAGGAAAAGA |

### 5.4.2 Synthesis of a PEGDA and DNA force sensor hydrogels

All force sensor hydrogels were prepared via the micromolding and photopolymerization protocol detailed in, § 3.4, Figure S3.3, and Figure S3.15. In lieu of cubes, cylinder magnets approximately 3 mm x 4 mm (height x diameter) were used. The final concentrations of all pregel componenets are as follows: 10% (wt./v) PEGDA ($M_n$ 575, Sigma catalog #437441), SPSC buffer, 1 $\mu$M of DNA force sensor complex, and 1% (v/v) of a 50% (v/v) mixture of Irgacure 2100 and 1-butanol. After aliquoting the mixture into the cylindrical molds, the pregel solution was polymerized via exposure to 365 nm UV light for roughly 30 minutes. The UV light intensity was approximately 4 mW/cm$^2$. The gels were then gently excised from the molds and placed in SPSC buffer for at least 24 hours to swell to equilibrium.

### 5.4.3 Determining hydrogel equilibrium swelling ratios

The equilibrium swelling ratio of PEGDA and poly(Am-co-BIS) hydrogels was obtained gravimetrically by measuring the weight of swollen and dehydrated gel samples. PEGDA hydrogels hydrogels were fabricated according to the protocol detailed in § 5.4.2. The 5% Am:BIS (19:1) hydrogel was prepared according to the protocol described in § 3.4 and Figure S3.15. After fabrication, the gels were swelled to equilibrium in either 1x TAE/Mg$^{2+}$ or 1x SPSC and then weighed. The gels were then completely dried by incubating in an oven at approximately 80 ℃ for at least 48 hours or until a stable weight was achieved. The equilibrium swelling ratio, $Q$, was obtained via the following well known relation:

$$Q = 1 + (q - 1)\frac{d_p}{d_w} \quad (5.17)$$

where $q$ is the ratio of the swollen hydrogel mass to the mass of the completely dehydrated gel, $d_p$ is the density of the polymer (here assumed to be 1.12 g/mL for PEGDA and 1.35 g/mL for polyacrylamide), and $d_w$ is the density of water (assume to be approximately the density of 1x SPSC).

### 5.4.2 Compression of force sensor gels using MFM microscope

PEGDA hydrogels were prepared as detailed in § 5.4.1 and allowed to swell to equilibrium. Once at equilibrium, the gels were submerged in approximately 200 $\mu$L of reporter complex. The reporter complex concentration was allowed to equilibrate throughout the gel over the course of roughly two days. Next, the height and diameter gels were recorded, and the gel was placed onto a multifunctional force microscope (MFM) developed by Roberts *et al.* The cantilever probe was lowered such that the probe surface was in contact with the gel sample. A normal force was then applied to the gel by lowering the cantilever (via the z-micro-translation stage) at a rate of either .2% or .1% of the total sample height per second. Throughout the deformation, the gel was imaged using a Chroma Red#1 FISH filter set (catalog #49306) and a Grasshopper3 U3 camera (type GS3-U3-23S6). For most MFM experiments, the gel sample was compressed until it fractured.

### 5.4.3 Analysis of MFM data

At the end of each run, the MFM outputs the position of the z-micro-translation stage, $z_{micro}$, and z-fiber optic distance, $z_{FO}$, over time. It also lists the fluorescence images taken by the Grasshopper3 that correspond to those data points. Given a spring constant of $k_s$, the normal force applied to the gel, $F_1$, was calculated using Hooke's law as follows:

$$F_1 = k_s(\Delta z_{FO}) \quad (5.17)$$

where $\Delta z_{FO}$ represents the total amount of deflection of the cantilever. Additionally, the total amount of indentation, $\Delta h$, of a hydrogel originally of height $h_0$ in the fully hydrated state can be expressed as,

$$\Delta h = \Delta z_{micro} - \Delta z_{FO} \quad (5.17)$$

from which the height of the sample during deformation, $h$, can be easily found. The stretch value $\lambda_1$can therefore be derived using the swelling ratio as follows:

$$\lambda_1 = \frac{h}{h_d} = \frac{h\sqrt[3]{Q}}{h_0}, \qquad \text{where } \sqrt[3]{Q} = \frac{h_0}{h_d} \tag{5.17}$$

with the reference state being the dehydrated sample and $h_d$ representing the theoretical height of a fully dehydrated cylindrical gel sample. Note that at $\lambda_1 = 1$ the height of the sample is the same as this theoretical height. Finally, the normal nominal stress $S_1$can be calculated as follows:

$$S_1 = \frac{F_1}{A} = \frac{F_1}{\frac{1}{4}\pi d_d^2} = \frac{4F_1 Q^{2/3}}{\pi d_0^2}, \qquad \text{where } \sqrt[3]{Q} = \frac{d_0}{d_d}$$

with $\sqrt[3]{Q}$ now expressed in terms of the sample diameter in the fully swollen, $d_0$, and dehydrated states, $d_d$.

### 5.4.4 qPCR testing of force sensor leak

To test whether the force sensor complexes were prone to give a false-positive signal, i.e., signal in the absence of any applied force, the fluorescence of a well-mixed solution of force sensor and reporter complex was monitored over several days using quantitative PCR (qPCR) machines (Agilent Stratagene Mx3000 and Mx3005 series). In a typical experiment, 75 nM reporter complex, 1x SPSC buffer, and MilliQ water were added to multiple wells in a 96-well plate. The resulting solution was mixed via pipet and the fluorescence was monitored (for roughly one hour) until a stable baseline count value was achieved. Next, 300 nM of the force sensor complex (SFS or HFS) was added to the wells and mixed via pipette. The fluorescence was then monitored for roughly two days, at which point an activator strand for the reporter was added to the mixture. This activator strand was added at roughly 1.5x the reporter complex concentration.

## 5.5 ACKNOWLEDGEMENTS

I thank P. Roberts and J. Frechette for use of their MFM instrument, overall technical assistance, and general discussions on hydrogel adhesion properties. I thank J. Liu and V. Nguyen for their work applying the Arruda-Boyce model to our materials and their expertise in soft material mechanics.

# CHAPTER 6 CONCLUSIONS AND FUTURE DIRECTIONS

Overall, the work presented in this thesis attempts to develop soft programmable matter potentially capable of complex, autonomous routines not seen in current soft robotic devices. We approach this task using the insights of DNA nanotechnology to confer on bulk materials an initial, primitive version of the programmable behavior that may, someday, be achieved. To bring this goal a little closer to fruition, there's an abundance of research on the DNA-acrylamide copolymer materials and swelling mechanism presented in *Chapter 3* that has yet to be done. First and foremost, the incorporation of reaction-diffusion dynamics into the constitutive model would greatly increase the accuracy of finite-element simulations and lead to better predictions of the end, deformed states that any device comprised of these materials can achieve. In addition, the change in material properties (i.e., elastic modulus, internal stress, etc.) that accompany the hairpin polymerization reaction should also be thoroughly investigated. The current constitutive model does not take into account the drastic change in these properties as the hydrogel swells via hairpin incorporation. For example, the current model assumes that the polymer network volume fraction (and concurrent mass fraction) remains constant over time, but simple back-of-the-envelope calculations show that this is not the case. For a gel swollen in a solution containing 2% terminator hairpins, assuming roughly 50 hairpins get incorporated at each DNA crosslinker site, the mass percent of the DNA in the materials goes from roughly 10% before swelling to approximately 90% after swelling. At the molecular scale, additional work should be performed to reverse the autonomous polymerization mechanism that drives gel swelling. Devising a DNA-based reaction scheme whereby the DNA crosslinks contract and expand dynamically, and with a large length range, would greatly enhance the applicability of these materials. Lastly, altering the hairpin polymerization reaction scheme or polymer network architecture to increase the actuation speed would also enhance the performance of these DNA-programmable soft matter devices.

Even though ample work could be done to more precisely characterize the polymer *science* behind the materials presented in *Chapter 3*, there already exists numerous applications of these materials in the biomedical space. For example, in the *New England Journal of Medicine* Arianna Menciassi posited the use of these materials to treat saccular cerebral aneurysms.[128] In this context the DNA-crosslinked gel would be deposited into the aneurysm and then expanded via the addition of DNA hairpins. The shape-changing properties of these hydrogels would make them better suited force these tasks then the currently-used wire coils. Lastly, these gels could also be used for targeted, chemoresponsive drug-delivery applications, albeit the material space for these applications is already somewhat crowded.

While it is admittedly in its infancy, the work presented in *Chapter 5* requires a significant amount of experimental verification before one can be confident that a DNA-programmable, force-sensing material has even been fabricated. More work will be required to cipher out true fluorescence signal from background noise due to processes that occur during deformation of the DNA-PEGDA copolymer hydrogels. It would be quite useful, and should be very feasible, to develop a DNA-based reaction protocol that can confirm, post-compression, that the fluorescence signal observed originates from the ruptured DNA mechanophores and their reaction with the reporter complex.

# REFERENCES

(1) Toffoli, T.; Margolus, N. Programmable Matter: Concepts and Realization. *Phys. D* **1991**, *47* (1–2), 263–272.

(2) Hawkes, E.; An, B.; Benbernou, N. M.; Tanaka, H.; Kim, S.; Demaine, E. D.; Rus, D.; Wood, R. J. Programmable Matter by Folding. *Proc. Natl. Acad. Sci.* **2010**, *107* (28), 12441–12445.

(3) McEvoy, M. A.; Correll, N. Materials That Couple Sensing, Actuation, Computation, and Communication. *Science.* **2015**, *347* (6228), 1261689.

(4) Hughes, D.; Correll, N. A Soft, Amorphous Skin That Can Sense and Localize Textures. In *Proceedings - IEEE International Conference on Robotics and Automation*; Hong Kong, 2014; pp 1844–1851.

(5) Profita, H. P.; Farrow, N.; Correll, N. Flutter: An Exploration of an Assistive Garment Using Distributed Sensing, Computation and Actuation. In *Proceedings of the 9th International Conference on Tangible, Embedded, and Embodied Interaction*; Association for Computing Machinery: New York, NY, 2015; pp 359–362.

(6) Farrow, N.; Sivagnanadasan, N.; Correll, N. Gesture Based Distributed User Interaction System for a Reconfigurable Self-Organizing Smart Wall. In *Proceedings of the 8th International Conference on Tangible, Embedded and Embodied Interaction - TEI '14*; Association for Computing Machinery: New York, NY, 2014; pp 245–246.

(7) Trivedi, D.; Rahn, C. D.; Kier, W. M.; Walker, I. D. Soft Robotics: Biological Inspiration, State of the Art, and Future Research. *Appl. Bionics Biomech.* **2008**, *5* (3), 99–117.

(8) Trivedi, D.; Lotfi, A.; Rahn, C. D. Geometrically Exact Dynamic Models for Soft Robotic Manipulators. *IEEE Trans. Robot.* **2008**, *24* (4), 773–780.

(9) Rus, D.; Tolley, M. T. Design, Fabrication and Control of Soft Robots. *Nature* **2015**, *521* (7553), 467–475.

(10) Laschi, C.; Mazzolai, B.; Cianchetti, M. Soft Robotics : Technologies and Systems Pushing the Boundaries of Robot Abilities. *Sci. Robot.* **2016**, *1* (1), eaah3690.

(11) Ilievski, F.; Mazzeo, A. D.; Shepherd, R. F.; Chen, X.; Whitesides, G. M. Soft Robotics for Chemists. *Angew. Chemie - Int. Ed.* **2011**, *50* (8), 1890–1895.

(12) Wehner, M.; Truby, R. L.; Fitzgerald, D. J.; Mosadegh, B.; Whitesides, G. M.; Lewis, J. A.; Wood, R. J. An Integrated Design and Fabrication Strategy for Entirely Soft, Autonomous Robots. *Nature* **2016**, *536* (7617), 451–455.

(13) Anseth, K. S.; Bowman, C. N.; Brannon-peppas, L. Mechanical Properties of Hydrogels and Their Experimental Determination. *Biomaterials* **1996**, *17* (17), 1647–1657.

(14) Kirschner, C. M.; Anseth, K. S. Hydrogels in Healthcare: From Static to Dynamic Material Microenvironments. *Acta Mater.* **2013**, *61* (3), 931–944.

(15) Rosales, A. M.; Anseth, K. S. The Design of Reversible Hydrogels to Capture Extracellular Matrix Dynamics. *Nat. Rev. Mater.* **2016**, *1* (2), 15012.

(16) Peppas, N. A.; Hilt, J. Z.; Khademhosseini, A.; Langer, R. Hydrogels in Biology and Medicine: From Molecular Principles to Bionanotechnology. *Adv. Mater.* **2006**, *18* (11), 1345–1360.

(17) Lu, Y.; Aimetti, A. A.; Langer, R.; Gu, Z. Bioresponsive Materials. *Nat. Rev. Mater.* **2017**, *2* (1), 16075.

(18) Jeon, S.; Hauser, A. W.; Hayward, R. C. Shape-Morphing Materials from Stimuli-Responsive Hydrogel Hybrids. *Acc. Chem. Res.* **2017**, *50* (2), 161–169.

(19) Koetting, M. C.; Peters, J. T.; Steichen, S. D.; Peppas, N. A. Stimulus-Responsive Hydrogels: Theory, Modern Advances, and Applications. *Mater. Sci. Eng. R Reports* **2015**, *93*, 1–49.

(20) Yoon, C.; Xiao, R.; Park, J.; Cha, J.; Nguyen, T. D.; Gracias, D. H. Functional Stimuli Responsive Hydrogel Devices by Self-Folding. *Smart Mater. Struct.* **2014**, *23* (9), 94008.

(21) Hauser, A. W.; Evans, A. A.; Na, J. H.; Hayward, R. C. Photothermally Reprogrammable Buckling of Nanocomposite Gel Sheets. *Angew. Chemie - Int. Ed.* **2015**, *54* (18), 5434–5437.

(22) Therien-Aubin, H.; Wu, Z. L.; Nie, Z.; Kumacheva, E. Multiple Shape Transformations of Composite Hydrogel Sheets. *J. Am. Chem. Soc.* **2013**, *135* (12), 4834–4839.

(23) Qian, L.; Winfree, E. Scaling up Digital Circuit Computation with DNA Strand Displacement Cascades. *Science.* **2011**, *332* (6034), 1196–1201.

(24) Qian, L.; Winfree, E.; Bruck, J. Neural Network Computation with DNA Strand Displacement Cascades. *Nature* **2011**, *475* (7356), 368–372.

(25) Alon, U. *An Introduction to Systems Biology*; CRC Press, 2006.

(26) Watson, J.; Crick, F. Molecular Structure of Nucleic Acids. *Nature.* **1953**, *171* (4356), 737–738.

(27) Breslauer, K. J.; Frank, R.; Blocker, H.; Marky, L. A. Predicting DNA Duplex Stability from the Base Sequence. *Proc. Natl. Acad. Sci.* **1986**, *83* (11), 3746–3750.

(28) Borer, P. N.; Dengler, B.; Tinoco, I.; Uhlenbeck, O. C. Stability of Ribonucleic Acid Double-Stranded Helices. *J. Mol. Biol.* **1974**, *86* (4), 843–853.

(29) SantaLucia, J. A Unified View of Polymer, Dumbbell, and Oligonucleotide DNA Nearest-Neighbor Thermodynamics. *Proc. Natl. Acad. Sci. U. S. A.* **1998**, *95* (4), 1460–1465.

(30) Zadeh, J. N.; Steenberg, C. D.; Bois, J. S.; Wolfe, B. R.; Pierce, M. B.; Khan, A. R.; Dirks, R. M.; Pierce, N. A. NUPACK: Analysis and Design of Nucleic Acid Systems. *J. Comput. Chem.* **2011**, *32* (1), 170–173.

(31) Zuker, M. Mfold Web Server for Nucleic Acid Folding and Hybridization Prediction. *Nucleic Acids Res.* **2003**, *31* (13), 3406–3415.

(32) Seeman, N. C. Nucleic Acid Junctions and Lattices. *J. Theor. Biol.* **1982**, *99* (2), 237–247.

(33) Adleman, L. M. Molecular Computation of Solutions to Combinatorial Problems. *Science.* **1994**, *266* (5187), 1021–1024.

(34) Seelig, G.; Soloveichik, D.; Zhang, D. Y.; Winfree, E. Enzyme-Free Nucleic Acid Logic Circuits. *Science.* **2006**, *314* (5805), 1585–1588.

(35) Zhang, D. Y.; Seelig, G. Dynamic DNA Nanotechnology Using Strand-Displacement Reactions. *Nat. Chem.* **2011**, *3* (2), 103–113.

(36) Zhang, D. Y.; Winfree, E. Control of DNA Strand Displacement Kinetics Using Toehold Exchange. *J. Am. Chem. Soc.* **2009**, *131* (47), 17303–17314.

(37) Nagahara, S.; Matsuda, T. Hydrogel Formation via Hybridization of Oligonucleotides Derivatized in Water-Soluble Vinyl Polymers. *Polym. Gels Networks* **1996**, *4* (2), 111–127.

(38) Murakami, Y.; Maeda, M. DNA-Responsive Hydrogels That Can Shrink or Swell. *Biomacromolecules* **2005**, *6* (6), 2927–2929.

(39) Lin, D. C.; Yurke, B.; Langrana, N. A. Inducing Reversible Stiffness Changes in DNA-Crosslinked Gels. *J. Mater. Res.* **2005**, *20* (6), 1456–1464.

(40) Lin, D. C.; Yurke, B.; Langrana, N. A. Mechanical Properties of a Reversible, DNA-Crosslinked Polyacrylamide Hydrogel. *J. Biomech. Eng.* **2004**, *126* (1), 104–110.

(41) Legewie, S.; Dienst, D.; Wilde, A.; Herzel, H.; Axmann, I. M. Small RNAs Establish Delays and Temporal Thresholds in Gene Expression. *Biophys. J.* **2008**, *95* (7), 3232–3238.

(42) Zaslaver, A.; Mayo, A. E.; Rosenberg, R.; Bashkin, P.; Sberro, H.; Tsalyuk, M.; Surette, M. G.; Alon, U. Just-in-Time Transcription Program in Metabolic Pathways. *Nat. Genet.* **2004**, *36* (5), 486–491.

(43) Dirks, R. M.; Pierce, N. A. Triggered Amplification by Hybridization Chain Reaction. *Proc. Natl. Acad. Sci. USA* **2004**, *101* (43), 15275–15278.

(44) Yin, P.; Choi, H. M. T.; Calvert, C. R.; Pierce, N. A. Programming Biomolecular Self-Assembly Pathways. *Nature* **2008**, *451* (7176), 318–322.

(45) Zhang, D. Y.; Hariadi, R. F.; Choi, H. M. T.; Winfree, E. Integrating DNA Strand-Displacement Circuitry with DNA Tile Self-Assembly. *Nat. Commun.* **2013**, *4* (May), 1965.

(46) Fu, J.; Yang, Y. R.; Johnson-Buck, A.; Liu, M.; Liu, Y.; Walter, N. G.; Woodbury, N. W.; Yan, H. Multi-Enzyme Complexes on DNA Scaffolds Capable of Substrate Channelling with an Artificial Swinging Arm. *Nat. Nanotechnol.* **2014**, *9* (7), 531–536.

(47) Caldorera-Moore, M.; Peppas, N. A. Micro- and Nanotechnologies for Intelligent and Responsive Biomaterial-Based Medical Systems. *Adv. Drug Deliv. Rev.* **2009**, *61* (15), 1391–1401.

(48) Santini, J. T.; Richards, A. C.; Scheidt, R.; Cima, M. J.; Langer, R. Microchips as Controlled Drug-Delivery Devices. *Angew. Chemie - Int. Ed.* **2000**, *39* (14), 2396–2407.

(49) Staples, M.; Daniel, K.; Cima, M. J.; Langer, R. Application of Micro- and Nano-Electromechanical Devices to Drug Delivery. *Pharm. Res.* **2006**, *23* (5), 847–863.

(50) Kapsner, K.; Simmel, F. C. Partitioning Variability of a Compartmentalized in Vitro Transcriptional Thresholding Circuit. *ACS Synth. Biol.* **2015**, *4* (10), 1136–1143.

(51) Takahashi, K.; Yaegashi, S.; Kameda, A.; Hagiya, M. Chain Reaction Systems Based on Loop Dissociation of DNA. *DNA Comput.* **2006**, *3892*, 347–358.

(52) Zhang, C.; Yang, J.; Xu, J. Circular DNA Logic Gates with Strand Displacement. *Langmuir* **2010**, *26* (3), 1416–1419.

(53) Genot, A. J.; Bath, J.; Turberfield, A. J. Reversible Logic Circuits Made of DNA. *J. Am. Chem. Soc.* **2011**, *133* (50), 20080–20083.

(54) Zhang, D. Y.; Seelig, G. DNA-Based Fixed Gain Amplifiers and Linear Classifier Circuits. *DNA Comput. Mol. Program.* **2011**, *6518*, 176–186.

(55) Zhang, D. Y.; Turberfield, A. J.; Yurke, B.; Winfree, E. Engineering Entropy-Driven Reactions and Networks Catalyzed by DNA. *Science.* **2007**, *318* (5853), 1121–1126.

(56) Chen, X.; Briggs, N.; McLain, J. R.; Ellington, A. D. Stacking Nonenzymatic Circuits for High Signal Gain. *Proc. Natl. Acad. Sci. USA* **2013**, *110* (14), 5386–5391.

(57) Seelig, G.; Yurke, B.; Winfree, E. Catalyzed Relaxation of a Metastable DNA Fuel. *J. Am. Chem. Soc.* **2006**, *128* (37), 12211–12220.

(58) Srinivas, N. Programming Chemical Kinetics : Engineering Dynamic Reaction Networks with DNA Strand Displacement, California Institute of Technology, 2015.

(59) Soloveichik, D.; Seelig, G.; Winfree, E. DNA as a Universal Substrate for Chemical Kinetics. *Proc. Natl. Acad. Sci. USA* **2010**, *107* (12), 5393–5398.

(60) Chen, Y.-J.; Dalchau, N.; Srinivas, N.; Phillips, A.; Cardelli, L.; Soloveichik, D.; Seelig, G. Programmable Chemical Controllers Made from DNA. *Nat. Nanotechnol.* **2013**, *8* (10), 755–762.

(61) Srinivas, N.; Ouldridge, T. E.; Šulc, P.; Schaeffer, J. M.; Yurke, B.; Louis, A. A.; Doye, J. P. K.; Winfree, E. On the Biophysics and Kinetics of Toehold-Mediated DNA Strand Displacement. *Nucleic Acids Res.* **2013**, *41* (22), 10641–10658.

(62) Qian, L.; Winfree, E. Parallel and Scalable Computation and Spatial Dynamics with DNA-Based Chemical Reaction Networks on a Surface. *DNA Comput. Mol. Program.* **2014**, *8727* (68), 114–131.

(63) Wang, J. S.; Zhang, D. Y. Simulation-Guided DNA Probe Design for Consistently Ultraspecific Hybridization. *Nat. Chem.* **2015**, *7* (7), 545–553.

(64) Zhang, Z.; Chen, N.; Li, S.; Battig, M. R.; Wang, Y. Programmable Hydrogels for Controlled Cell Catch and Release Using Hybridized Aptamers and Complementary Sequences. *J. Am. Chem. Soc.* **2012**, *134* (38), 15716–15719.

(65) Gatto, B.; Palumbo, M.; Sissi, C. Nucleic Acid Aptamers Based on the G-Quadruplex Structure: Therapeutic and Diagnostic Potential. *Curr. Med. Chem.* **2009**, *16* (10), 1248–1265.

(66) Huizenga, D. E.; Szostak, J. W. A DNA Aptamer That Binds Adenosine and ATP. *Biochemistry* **1995**, *34* (2), 656–665.

(67) Yao, D.; Song, T.; Sun, X.; Xiao, S.; Huang, F.; Liang, H. Integrating DNA-Strand-Displacement Circuitry with Self-Assembly of Spherical Nucleic Acids. *J. Am. Chem. Soc.* **2015**, *137* (44), 14107–14113.

(68) Scalise, D.; Schulman, R. Designing Modular Reaction-Diffusion Programs for Complex Pattern Formation. *Technology* **2014**, *2* (1), 55–66.

(69) Puglisi, J. D.; Tinoco, I. Absorbance Melting Curves of RNA. *Methods Enzymol.* **1989**, *180*, 304–325.

(70) Gracias, D. H. Stimuli Responsive Self-Folding Using Thin Polymer Films. *Curr. Opin. Chem. Eng.* **2013**, *2* (1), 112–119.

(71) Liu, Y.; Boyles, J. K.; Genzer, J.; Dickey, M. D. Self-Folding of Polymer Sheets Using Local Light Absorption. *Soft Matter* **2012**, *8* (6), 1764–1769.

(72) Zarzar, L. D.; Aizenberg, J. Stimuli-Responsive Chemomechanical Actuation: A Hybrid Materials Approach. *Acc. Chem. Res.* **2014**, *47* (2), 530–539.

(73) Liedl, T.; Dietz, H.; Yurke, B.; Simmel, F. Controlled Trapping and Release of Quantum Dots in a DNA-Switchable Hydrogel. *Small* **2007**, *3* (10), 1688–1693.

(74) Hu, Y.; Kahn, J. S.; Guo, W.; Huang, F.; Fadeev, M.; Harries, D.; Willner, I. Reversible Modulation of DNA-Based Hydrogel Shapes by Internal Stress Interactions. *J. Am. Chem. Soc.* **2016**, *138* (49), 16112–16119.

(75) Kahn, J. S.; Hu, Y.; Willner, I. Stimuli-Responsive DNA-Based Hydrogels: From Basic Principles to Applications. *Acc. Chem. Res.* **2017**, *50* (4), 680–690.

(76) Yan, H.; Zhang, X.; Shen, Z.; Seeman, N. C. A Robust DNA Mechanical Device Controlled by Hybridization Topology. *Nature* **2002**, *415* (6867), 62–65.

(77) Shim, T. S.; Estephan, Z. G.; Qian, Z.; Prosser, J. H.; Lee, S. Y.; Chenoweth, D. M.; Lee, D.; Park, S.-J.; Crocker, J. C. Shape Changing Thin Films Powered by DNA Hybridization. *Nat. Nanotechnol.* **2017**, *12* (1), 41–47.

(78) Kim, Y.; Macfarlane, R. J.; Jones, M. R.; Mirkin, C. A. Transmutable Nanoparticles with Reconfigurable Surface Ligands. *Science.* **2016**, *351* (6273), 579–582.

(79) Zhang, Y.; Pal, S.; Srinivasan, B.; Vo, T.; Kumar, S.; Gang, O. Selective Transformations between Nanoparticle Superlattices via the Reprogramming of DNA-Mediated Interactions. *Nat. Mater.* **2015**, *14* (8), 840–847.

(80) Maye, M. M.; Kumara, M. T.; Nykypanchuk, D.; Sherman, W. B.; Gang, O. Switching Binary States of Nanoparticle Superlattices and Dimer Clusters by DNA Strands. *Nat. Nanotechnol.* **2010**, *5* (2), 116–120.

(81) Zhang, Y.; Zhao, Y. P. Applicability Range of Stoney's Formula and Modified Formulas for a Film/substrate Bilayer. *J. Appl. Phys.* **2006**, *99* (5), 53513.

(82) Venkataraman, S.; Dirks, R. M.; Rothemund, P. W. K.; Winfree, E.; Pierce, N. A. An Autonomous Polymerization Motor Powered by DNA Hybridization. *Nat. Nanotechnol.* **2007**, *2* (8), 490–494.

(83) Huang, F.; Zhou, X.; Yao, D.; Xiao, S.; Liang, H. DNA Polymer Brush Patterning through Photocontrollable Surface-Initiated DNA Hybridization Chain Reaction. *Small* **2015**, *11* (43), 5800–5806.

(84) Flory, P. J.; Rehner, J. J. Statistical Mechanics of Cross-Linked Polymer Networks I. Rubberlike Elasticity. *J. Chem. Phys.* **1943**, *11* (11), 512–520.

(85) Freund, L. B.; Floro, J. A.; Chason, E. Extensions of the Stoney Formula for Substrate Curvature to Configurations with Thin Substrates or Large Deformations. *Appl. Phys. Lett.* **1999**, *74* (14), 1987–1989.

(86) Zhou, W.; Huang, P. J.; Liu, J. Aptamer-Based Biosensors for Biomedical Diagnostics. *Analyst* **2014**, *139*, 2627–2640.

(87) Postma, S. G. J.; Vialshin, I. N.; Gerritsen, C. Y.; Bao, M.; Huck, W. T. S. Preprogramming Complex Hydrogel Responses Using Enzymatic Reaction Networks. *Angew. Chemie Int. Ed.* **2017**, *56* (7), 1794–1798.

(88) Ikeda, M.; Tanida, T.; Yoshii, T.; Kurotani, K.; Onogi, S.; Urayama, K.; Hamachi, I. Installing Logic-Gate Responses to a Variety of Biological Substances in Supramolecular Hydrogel-Enzyme Hybrids. *Nat. Chem.* **2014**, *6* (6), 511–518.

(89) Schulman, R.; Yurke, B.; Winfree, E. Robust Self-Replication of Combinatorial Information via Crystal Growth and Scission. *Proc. Natl. Acad. Sci.* **2012**, *109* (17), 6405–6410.

(90) Jamal, M.; Kadam, S. S.; Xiao, R.; Jivan, F.; Onn, T. M.; Fernandes, R.; Nguyen, T. D.; Gracias, D. H. Bio-Origami Hydrogel Scaffolds Composed of Photocrosslinked PEG Bilayers. *Adv. Healthc. Mater.* **2013**, *2* (8), 1142–1150.

(91) Linder, V.; Gates, B. D.; Ryan, D.; Parviz, B. A.; Whitesides, G. M. Water-Soluble Sacrificial Layers for Surface Micromachining. *Small* **2005**, *1* (7), 730–736.

(92) Kang, H.; Liu, H.; Zhang, X.; Yan, J.; Zhu, Z.; Peng, L.; Yang, H.; Kim, Y.; Tan, W. Photoresponsive DNA-Cross-Linked Hydrogels for Controllable Release and Cancer Therapy. *Langmuir* **2011**, *27* (1), 399–408.

(93) Hong, W.; Zhao, X.; Zhou, J.; Suo, Z. A Theory of Coupled Diffusion and Large Deformation in Polymeric Gels. *J. Mech. Phys. Solids* **2008**, *56* (5), 1779–1793.

(94) Chester, S. A.; Anand, L. A Coupled Theory of Fluid Permeation and Large Deformations for Elastomeric Materials. *J. Mech. Phys. Solids* **2010**, *58* (11), 1879–1906.

(95) Breger, J. C.; Yoon, C.; Xiao, R.; Kwag, H. R.; Wang, M. O.; Fisher, J. P.; Nguyen, T. D.; Gracias, D. H. Self-Folding Thermo-Magnetically Responsive Soft Microgrippers. *ACS Appl. Mater. Interfaces* **2015**, *7* (5), 3398–3405.

(96) Yoon, C.; Xiao, R.; Park, J.; Cha, J.; Nguyen, T. D.; Gracias, D. H. (SI) Functional Stimuli Responsive Hydrogel Devices by Self-Folding. *Smart Mater. Struct.* **2014**, *23* (9), 94008.

(97) Ogden, R. W. Large Deformation Isotropic Elasticity: On the Correlation of Theory and Experiment for Compressible Rubberlike Solids. *Proc. R. Soc. London A Math. Phys. Eng. Sci.* **1972**, *328* (1575), 567–583.

(98) Stoney, G. G. The Tension of Metallic Films Deposited by Electrolysis. *Proc. R. Soc. London A Math. Phys. Eng. Sci.* **1909**, *82* (553), 172–175.

(99) Shah, A. M.; Yu, M.; Nakamura, Z.; Ciciliano, J.; Ulman, M.; Kotz, K.; Stott, S. L.; Maheswaran, S.; Haber, D. A.; Toner, M. Biopolymer System for Cell Recovery from Microfluidic Cell Capture Devices. *Anal. Chem.* **2012**, *84* (8), 3682–3688.

(100) Wang, X.-Y.; Jin, Z.-H.; Gan, B.-W.; Lv, S.-W.; Xie, M.; Huang, W.-H. Engineering

Interconnected 3D Vascular Networks in Hydrogels Using Molded Sodium Alginate Lattice as the Sacrificial Template. *Lab Chip* **2014**, *14* (15), 2709–2716.
(101) Sung, J. H.; Yu, J.; Luo, D.; Shuler, M. L.; March, J. C. Microscale 3-D Hydrogel Scaffold for Biomimetic Gastrointestinal (GI) Tract Model. *Lab Chip* **2011**, *11* (3), 389–392.
(102) Harris, D. C. *Quantitative Chemical Analysis*, 8th ed.; W. H. Freeman and Company: New York, NY, 2010.
(103) Beyer, M. K.; Clausen-Schaumann, H. Mechanochemistry: The Mechanical Activation of Covalent Bonds. *Chem. Rev.* **2005**, *105* (8), 2921–2948.
(104) Li, J.; Nagamani, C.; Moore, J. S. Polymer Mechanochemistry: From Destructive to Productive. *Acc. Chem. Res.* **2015**, *48* (8), 2181–2190.
(105) Lee, C. K.; Beiermann, B. A.; Silberstein, M. N.; Wang, J.; Moore, S.; Sottos, N. R.; Braun, P. V. Exploiting Force Sensitive Spiropyrans as Molecular Level Probes. *Macromolecules* **2013**, *46*, 3746–3752.
(106) Wang, Q.; Gossweiler, G. R.; Craig, S. L.; Zhao, X. Mechanics of Mechanochemically Responsive Elastomers. *J. Mech. Phys. Solids* **2015**, *82*, 320–344.
(107) Silberstein, M. N.; Cremar, L. D.; Beiermann, B. A.; Kramer, S. B.; Martinez, T. J.; White, S. R.; Sottos, N. R. Modeling Mechanophore Activation within a Viscous Rubbery Network. *J. Mech. Phys. Solids* **2014**, *63*, 141–153.
(108) Fern, J.; Scalise, D.; Cangialosi, A.; Howie, D.; Potters, L.; Schulman, R. DNA Strand-Displacement Timer Circuits. *ACS Synth. Biol.* **2017**, *6* (2), 190–193.
(109) Rothemund, P. W. K. Folding DNA to Create Nanoscale Shapes and Patterns. *Nature* **2006**, *440* (7082), 297–302.
(110) Ke, Y.; Ong, L. L.; Shih, W. M.; Yin, P. Three-Dimensional Structures Self-Assembled from DNA Bricks. *Science.* **2012**, *338* (6111), 1177–1183.
(111) Cha, T.; Pan, J.; Chen, H.; Salgado, J.; Li, X.; Mao, C.; Choi, J. H. A Synthetic DNA Motor That Transports Nanoparticles along Carbon Nanotubes. *Nat. Nanotechnol.* **2013**, *9* (1), 39–43.
(112) Wickham, S. F. J.; Bath, J.; Katsuda, Y.; Endo, M.; Hidaka, K.; Sugiyama, H.; Turberfield, A. J. A DNA-Based Molecular Motor That Can Navigate a Network of Tracks. *Nat. Nanotechnol.* **2012**, *7* (3), 169–173.
(113) Bustamante, C.; Bryant, Z.; Smith, S. B. Ten Years of Tension: Single-Molecule DNA Mechanics. *Nature* **2003**, *421* (6921), 423–427.
(114) Wang, M. D.; Schnitzer, M. J.; Yin, H.; Landick, R.; Gelles, J.; Block, S. M. Force and Velocity Measures for Single Molecule of RNA Polymerase. *Science.* **1998**, *282* (5390), 902–907.
(115) Davenport, R. J.; Wuite, G. J. L.; Landick, R.; Bustamante, C. Single-Molecule Study of Transcriptional Pausing and Arrest by E . Coli RNA Polymerase. *Science.* **2000**, *287* (5462), 2497–2500.
(116) Wuite, G. J. L.; Smith, S. B.; Young, M.; Keller, D.; Bustamante, C. Single-Molecule Studies of the Effect of Template Tension on T7 DNA Polymerase Activity. *Nature* **2000**, *404* (6773), 103–106.
(117) Maier, B.; Bensimon, D.; Croquette, V. Replication by a Single DNA Polymerase of a Stretched Single-Stranded DNA. *Proc. Natl. Acad. Sci. USA* **2000**, *97* (22), 12002–12007.
(118) Mosayebi, M.; Louis, A. A.; Doye, J. P. K.; Ouldridge, T. E. Force-Induced Rupture of a DNA Duplex : From Fundamentals to Force Sensors. *ACS Nano* **2015**, *9* (12), 11993–12003.
(119) Wang, X.; Ha, T. Defining Single Molecular Forces Required to Activate Integrin and Notch Signaling. *Science.* **2013**, *340* (6135), 991–994.
(120) Zhang, Y.; Ge, C.; Zhu, C.; Salaita, K. DNA-Based Digital Tension Probes Reveal Integrin Forces during Early Cell Adhesion. *Nat. Commun.* **2014**, *5*, 5167.
(121) Arruda, E. M.; Boyce, M. C. A Three-Dimensional Constitutive Model for the Large Stretch Behavior of Rubber Elastic Materials. *J. Mech. Phys. Solids* **1993**, *41* (2), 389–412.
(122) Treloar, L. R. G. *The Physics of Rubber Elasticity*, 3rd ed.; Oxford University Press: USA, 1975.
(123) DeGennes, P.-G. Maximum Pull out Force on DNA Hybrids. *Biophysics (Oxf).* **2001**, *2147* (1), 1505–1508.
(124) Hatch, K.; Danilowicz, C.; Coljee, V.; Prentiss, M. Demonstration That the Shear Force Required to Separate Short Double-Stranded DNA Does Not Increase Significantly with Sequence Length for Sequences Longer than 25 Base Pairs. *Phys. Rev. E* **2008**, *78* (1), 11920.
(125) Woodside, M. T.; Behnke-Parks, W. M.; Larizadeh, K.; Travers, K.; Herschlag, D.; Block, S. M.

Nanomechanical Measurements of the Sequence-Dependent Folding Landscapes of Single Nucleic Acid Hairpins. *Proc. Natl. Acad. Sci. USA* **2006**, *103* (16), 6190–6195.

(126) Bloomfield, V. A.; Crothers, D. M.; Tinoco Jr., I. *Nucleic Acids: Structures, Properties, and Functions*; University Science Books: Sausalito, CA, 2000.

(127) Roberts, P.; Pilkington, G. A.; Wang, Y.; Frechette, J. A Multifunctional Force Microscope for Soft Matter with in Situ Imaging A Multifunctional Force Microscope for Soft Matter with in Situ Imaging. *Rev. Sci. Instrum.* **2018**, *89* (43902), 1–8.

(128) Menciassi, A. Swell Findings in Hydrogels. *N. Engl. J. Med.* **2018**, *378* (9), 864–865.

# CURRICULUM VITAE

Along with his four siblings, Angelo Cangialosi was born in New York City, NY on October 15, 1987 to parents Angelo and Alice Cangialosi. He spent his childhood in the Long Island suburb of Lake Ronkonkoma, NY and attended high school at Sachem North High. Angelo went on to receive his Bachelor of Science degree in Biochemistry from Boston College in May 2010. As an undergraduate, he spent roughly one year conducting organic chemistry research where he investigated enantioselective conjugate addition reactions. Next, Angelo worked in the Hydrogen & Fuel Cell Program at the U.S. Department of Energy for roughly 18 months where he helped prepare technical reports, create program briefings, and helped manage program funds. In August 2013 Angelo enrolled in the Ph.D. program in the Chemical & Biomolecular Engineering Department at Johns Hopkins University. While at Hopkins he worked with Prof. Rebecca Schulman to develop DNA programmable hydrogel devices and had the good fortune to learn from the bright minds of colleagues and faculty.